Strain engineering and epitaxial stabilization of halide perovskites

https://doi.org/10.1038/s41586-019-1868-x

Received: 12 April 2019

Accepted: 19 November 2019

Published online: 8 January 2020

Yimu Chen[1,8], Yusheng Lei[1,8], Yuheng Li[1], Yugang Yu[2], Jinze Cai[2], Ming-Hui Chiu[3], Rahul Rao[4], Yue Gu[2], Chunfeng Wang[1], Woojin Choi[5], Hongjie Hu[2], Chonghe Wang[1], Yang Li[1], Jiawei Song[2], Jingxin Zhang[2], Baiyan Qi[2], Muyang Lin[1], Zhuorui Zhang[1], Ahmad E. Islam[4], Benji Maruyama[4], Shadi Dayeh[1,2,5], Lain-Jong Li[3,6], Kesong Yang[1], Yu-Hwa Lo[2,5] & Sheng Xu[1,2,5,7]*

Strain engineering is a powerful tool with which to enhance semiconductor device performance[1,2]. Halide perovskites have shown great promise in device applications owing to their remarkable electronic and optoelectronic properties[3–5]. Although applying strain to halide perovskites has been frequently attempted, including using hydrostatic pressurization[6–8], electrostriction[9], annealing[10–12], van der Waals force[13], thermal expansion mismatch[14], and heat-induced substrate phase transition[15], the controllable and device-compatible strain engineering of halide perovskites by chemical epitaxy remains a challenge, owing to the absence of suitable lattice-mismatched epitaxial substrates. Here we report the strained epitaxial growth of halide perovskite single-crystal thin films on lattice-mismatched halide perovskite substrates. We investigated strain engineering of α-formamidinium lead iodide (α-$FAPbI_3$) using both experimental techniques and theoretical calculations. By tailoring the substrate composition—and therefore its lattice parameter—a compressive strain as high as 2.4 per cent is applied to the epitaxial α-$FAPbI_3$ thin film. We demonstrate that this strain effectively changes the crystal structure, reduces the bandgap and increases the hole mobility of α-$FAPbI_3$. Strained epitaxy is also shown to have a substantial stabilization effect on the α-$FAPbI_3$ phase owing to the synergistic effects of epitaxial stabilization and strain neutralization. As an example, strain engineering is applied to enhance the performance of an α-$FAPbI_3$-based photodetector.

α-$FAPbI_3$ is epitaxially grown on a series of mixed methylammonium lead chloride/bromide ($MAPbCl_xBr_{3-x}$) single crystalline substrates by the inverse temperature growth method[16]. The resulting $MAPbCl_xBr_{3-x}$ substrates, with different compositional ratios and thus lattice parameters, are grown by solutions with different Cl/Br precursor molar ratios (Supplementary Fig. 1)[17]. We note that the strain in the epilayer is determined not only by the lattice mismatch, but also by the relaxation mechanisms. Lattice distortion relaxes the strain, so the region near the heteroepitaxy interface has the highest strain, which gradually drops at regions distant from the interface. The total elastic strain energy increases as the film grows thicker, until it eventually crosses the threshold energy for structural defect generation, and dislocations will form to partially relieve the misfit[18]. A slow growth rate of the epilayer is chosen, as a higher rate will increase the defect concentration in the epilayer. The crystalline quality of the substrates is carefully optimized, as the defects in the substrates can propagate into the epilayer (Extended Data Fig. 1).

Heteroepitaxial growth leads to controllable film thickness, preferential growth sites and orientations, compatible fabrication protocols with existing infrastructures and scalable large-area device applications. Figure 1a shows optical images of a series of $MAPbCl_xBr_{3-x}$ substrates with a layer of epitaxial α-$FAPbI_3$ film on the top. The epilayer has a uniform thickness with a well defined film–substrate interface (Fig. 1b). The film topography can reveal the growth mechanism and sometimes the defects caused by strain relaxation. On the one hand, a sub-100 nm α-$FAPbI_3$ thin film shows a clear interface (Fig. 1b), and a well defined terrain morphology, with a step height close to the size of a α-$FAPbI_3$ unit cell, indicating layer-by-layer growth behaviour of the epitaxial α-$FAPbI_3$ (Extended Data Fig. 2a, b). A 10-μm film, on the other hand, shows non-conformal growth, indicating strain relaxation by dislocation formation (Extended Data Fig. 2c, d).

The crystallographic relationships between the $MAPbCl_xBr_{3-x}$ substrates and the epitaxial α-$FAPbI_3$ thin films are illustrated by high-resolution X-ray diffraction (XRD) (Fig. 1c). In their freestanding form, both α-$FAPbI_3$ and $MAPbCl_xBr_{3-x}$ have a cubic structure[19,20]. The lattice parameters of freestanding α-$FAPbI_3$ and $MAPbCl_xBr_{3-x}$ substrates (both with *Pm*3*m* space group) are calculated to be 6.35 Å (Supplementary Fig. 1) and 5.83–5.95 Å, respectively. The ratio x for each

[1]Department of Nanoengineering, University of California San Diego, La Jolla, CA, USA. [2]Materials Science and Engineering Program, University of California San Diego, La Jolla, CA, USA. [3]Physical Science and Engineering Division, King Abdullah University of Science and Technology, Thuwal, Saudi Arabia. [4]Materials and Manufacturing Directorate, Air Force Research Laboratory, Wright Patterson Air Force Base, Dayton, OH, USA. [5]Department of Electrical and Computer Engineering, University of California San Diego, La Jolla, CA, USA. [6]School of Materials Science and Engineering, University of New South Wales, Sydney, New South Wales, Australia. [7]Department of Bioengineering, University of California San Diego, La Jolla, CA, USA. [8]These authors contributed equally: Yimu Chen, Yusheng Lei. *e-mail: shengxu@ucsd.edu

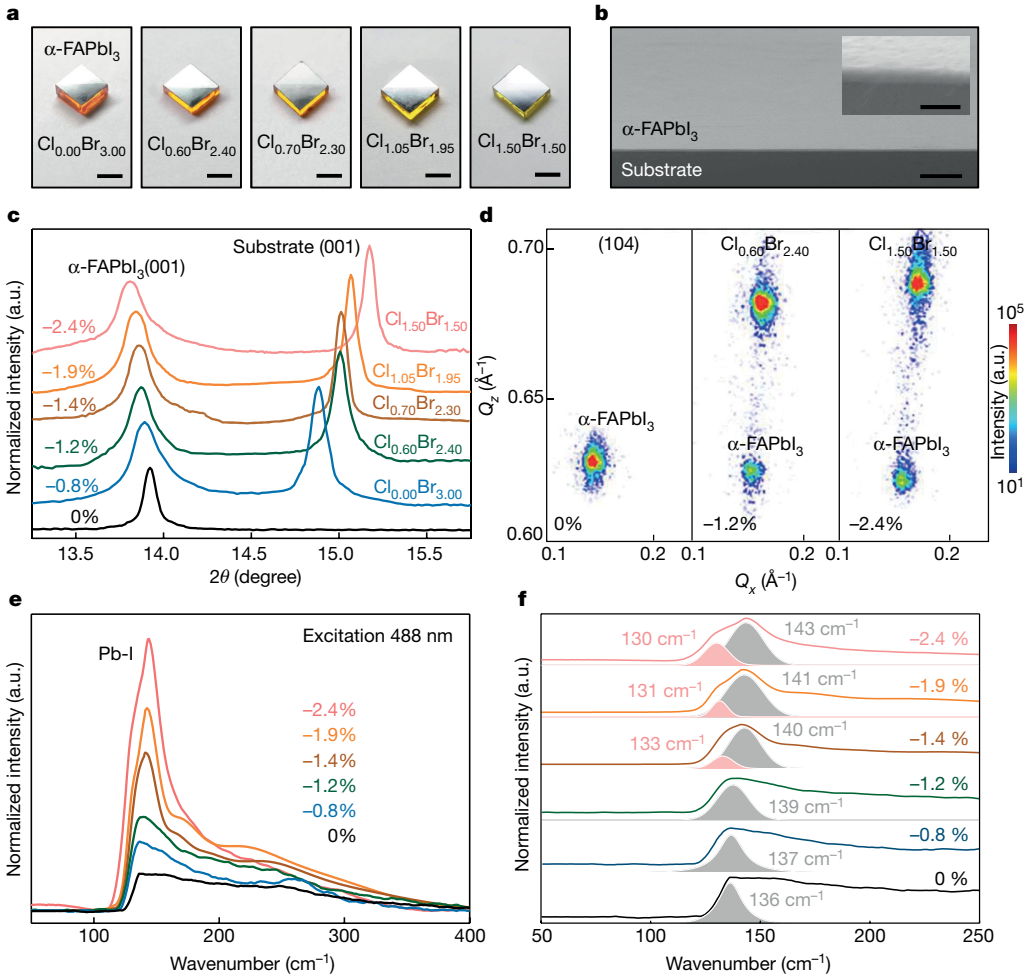

Fig. 1 | Epitaxial α-FAPbI$_3$ thin films and structural characterizations. **a**, Optical images of the as-grown epitaxial α-FAPbI$_3$ thin films. The high transparency of the substrates and the smooth surfaces of the thin films demonstrate their high quality. Scale bars, 4 mm. **b**, A cross-sectional scanning electron microscope (SEM) image of the epitaxial thin film with controlled uniform thickness. Scale bar, 2 μm. Inset, magnified SEM image of the heterostructure showing a well defined interface. Scale bar, 200 nm. **c**, High-resolution XRD $\omega-2\theta$ scan of the (001) peaks of the epitaxial samples on different substrates showing the increasing tetragonality with increasing lattice mismatch. **d**, Reciprocal space mapping with (104) asymmetric reflection of the α-FAPbI$_3$, for different lattice mismatches with the substrate. The results show a decrease in the in-plane lattice parameter as well as an increase in the out-of-plane lattice parameter with larger compressive strain. Q_x and Q_z are the in-plane and out-of-plane reciprocal space coordinates. **e**, Confocal Raman spectra of the epitaxial layer at different strains. We attribute the evolution of the shape and intensity of the peak with strain to the increase in lattice tetragonality under higher strain. We note that the broad peak at approximately 250 cm^{-1} is attributed to the Pb–O bond induced by laser oxidation. **f**, Fitting analysis of the Raman peaks. The peak at 136 cm^{-1} from the strain-free sample (black line) is attributed to the Pb–I bond. With increasing compressive strain, the peak gradually blueshifts as the bond becomes more rigid, and finally splits into a main peak that blueshifts (owing to in-plane bond contraction) and a shoulder peak that redshifts (owing to out-of-plane bond extension). (a.u., arbitrary units).

composition is then calculated to be 0–1.50, according to the Vegard's Law (Supplementary Table 1). As x increases, the MAPbCl$_x$Br$_{3-x}$ (001) peaks shift to a higher 2θ angle, indicating a decrease in the lattice parameters of the substrate and therefore an increase in the lattice mismatch (Fig. 1c and Supplementary Table 2). Meanwhile, the α-FAPbI$_3$ (001) peak shifts to a lower 2θ angle, indicating an increase in the out-of-plane lattice parameter as the in-plane compressive strain increases. When x exceeds 1.50, the strain energy dramatically increases, and the epitaxial growth becomes less thermodynamically favourable. α-FAPbI$_3$ then randomly crystallizes on the substrate (Supplementary Fig. 2). Peak broadening of the epitaxial α-FAPbI$_3$ is therefore induced by the epitaxial strain and the reduction in film thickness, instead of by the strain-induced dislocations or the strain relaxation (Supplementary Fig. 3). Figure 1d shows the reciprocal space mapping of strain-free and strained α-FAPbI$_3$ thin films with different lattice mismatch with the substrate. An increase of tetragonality of the lattice is evident as the compressive strain increases. The corresponding strain levels of the α-FAPbI$_3$ in those three cases are calculated to be 0%, −1.2% and −2.4%, respectively, on the basis of the lattice distortion (where the negative sign denotes compressive strain). The Poisson's ratio is determined to be around 0.3, which is consistent with the reported value[21].

We also studied the structure of α-FAPbI$_3$ at different strains (between 0% and −2.4%, on different substrates) by Raman spectroscopy (Fig. 1e). Control experiments exclude any Raman signals from the substrates (Supplementary Fig. 4). The peak at around 136 cm^{-1} in Fig. 1e, which originated from the stretching of the lead–iodine bond[22], increases in intensity and broadens in width as the strain increases. The cubic structure of the strain-free α-FAPbI$_3$ is less Raman-active, and the detectable signal is usually broad and weak. When in-plane compressive strain increases, the inorganic framework gradually gains tetragonality and produces a stronger Raman signal with a clearly distinguishable shape. Interestingly, at around −1.4% strain, the peak at 136 cm^{-1} starts to split into two: a main peak at about 140 cm^{-1} and a

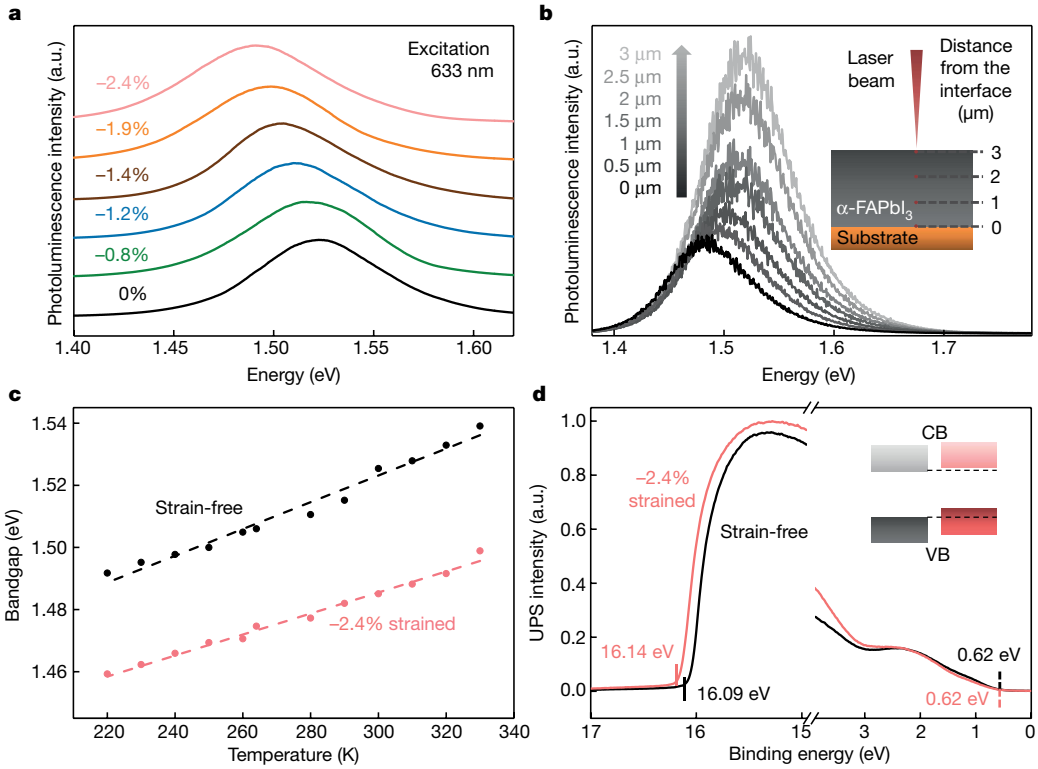

Fig. 2 | Optical properties. a, Photoluminescence spectra of α-$FAPbI_3$ at different strains. The redshift of the photoluminescence peak with increasing strain is due to bandgap reduction under compressive strain, consistent with the first-principles calculations. **b**, Focal-point-dependent confocal photoluminescence spectra of a 3-μm-thick film. When the focal point of the laser (indicated by the red point in the schematic; inset) moves towards the epitaxial interface, the photoluminescence emission peak shifts from about 1.523 eV to about 1.479 eV, owing to the large compressive strain close to the interface. **c**, Temperature-dependent photoluminescence spectra of a −2.4% strained and a strain-free sample. The bandgap of the strain-free sample shows a stronger temperature dependence than the strained sample, indicating that the substrate can reduce the lattice deformation that is caused by the temperature change. **d**, UPS spectra of a −2.4% strained and a strain-free sample. The Fermi level and the VBM of the samples can be extracted from the intersections of the curves with the horizontal axis, marked by the solid and dashed vertical lines, respectively. The results reveal that compressive strain increases the VBM more than it does the CBM, owing to the enhanced interaction of lead 6*s* and iodine 5*p* orbitals under the compressive strain. Inset, the schematic band diagram of the −2.4% strained and strain-free samples. CB, conduction band; VB, valence band.

shoulder at about 133 cm^{-1} (Fig. 1f). When the strain is further increased to −2.4%, these two peaks shift to 143 cm^{-1} and 130 cm^{-1}, respectively. We attribute the blueshift of the main peak to the compression of the in-plane lead–iodine bond, and the redshift of the shoulder peak to the stretching of the out-of-plane lead–iodine bond. This result is also supported by the simulated Raman spectra by first-principles calculations (Supplementary Fig. 4c, d). We also studied the Raman spectra of α-$FAPbI_3$ of various thicknesses on $MAPbCl_{1.50}Br_{1.50}$ (Supplementary Fig. 4f). The results are consistent: a strong, sharp peak is detected from a sub-100-nm film with −2.4% strain, and a weak, broad peak is detected from a film of around 2 μm, where the misfit strain is relaxed near the film surface.

Photoluminescence spectra (Fig. 2a) reveal changes in the bandgap of sub-100-nm epitaxial α-$FAPbI_3$ thin films under different strains (between 0% and −2.4%, on different substrates). The photoluminescence peak of α-$FAPbI_3$ gradually shifts from about 1.523 eV at 0% strain to about 1.488 eV at −2.4% strain, corresponding to a reduction of about 35 meV in the bandgap. We exclude the possible contributions to this photoluminescence redshift from thickness-dependent bandgap[23,24], reabsorption[25] or halide migration[26] (detailed discussions in the Supplementary Information). The bandgap change is consistent with the first-principles calculations and absorption measurements (Extended Data Fig. 3). The photoluminescence peak in Fig. 2a also broadens with increasing strain (Supplementary Fig. 5), which is not due to possible charge transfer between the epitaxial α-$FAPbI_3$ and the substrate (Supplementary Fig. 6). Temperature-dependent photoluminescence studies suggest that the emission peak broadening originates from the reduced crystalline quality and the enhanced carrier–phonon coupling under the strain (Extended Data Fig. 4).

Additionally, we studied confocal photoluminescence spectra at different locations in an α-$FAPbI_3$ film of around 3 μm on a substrate of $MAPbCl_{1.50}Br_{1.50}$ (Fig. 2b). The photoluminescence peak shifts from about 1.479 eV when the laser is focused at the interface where the local strain is high, to about 1.523 eV at 3 μm from the interface where the strain is relaxed. As a control, the photoluminescence redshift in a strain-free sample is less obvious (from about 1.516 eV to about 1.523 eV, Supplementary Fig. 7a), which is attributed to reabsorption[25]. In the strained sample, we exclude elastic relaxation although halide perovskites are much softer than conventional semiconductors[27]. Our finite element analysis simulation results show that the elastic relaxation for a 3-μm-thick α-$FAPbI_3$ thin film is negligible: only around 0.09% (Supplementary Fig. 8). Thickness-dependent in-plane XRD is used to study the critical thickness at which the strain will start to be plastically relaxed (Extended Data Fig. 5). The results show that the critical thickness is much less than the thickness we used in this study and, therefore, the relaxation can be attributed to plastic relaxation by the formation of dislocations. Photoluminescence measurements from samples of different thicknesses show a similar trend (Supplementary Fig. 9), indicating that the strain is relaxed by dislocations when the film grows thicker. Temperature-dependent photoluminescence studies indicate that the bandgap of α-$FAPbI_3$

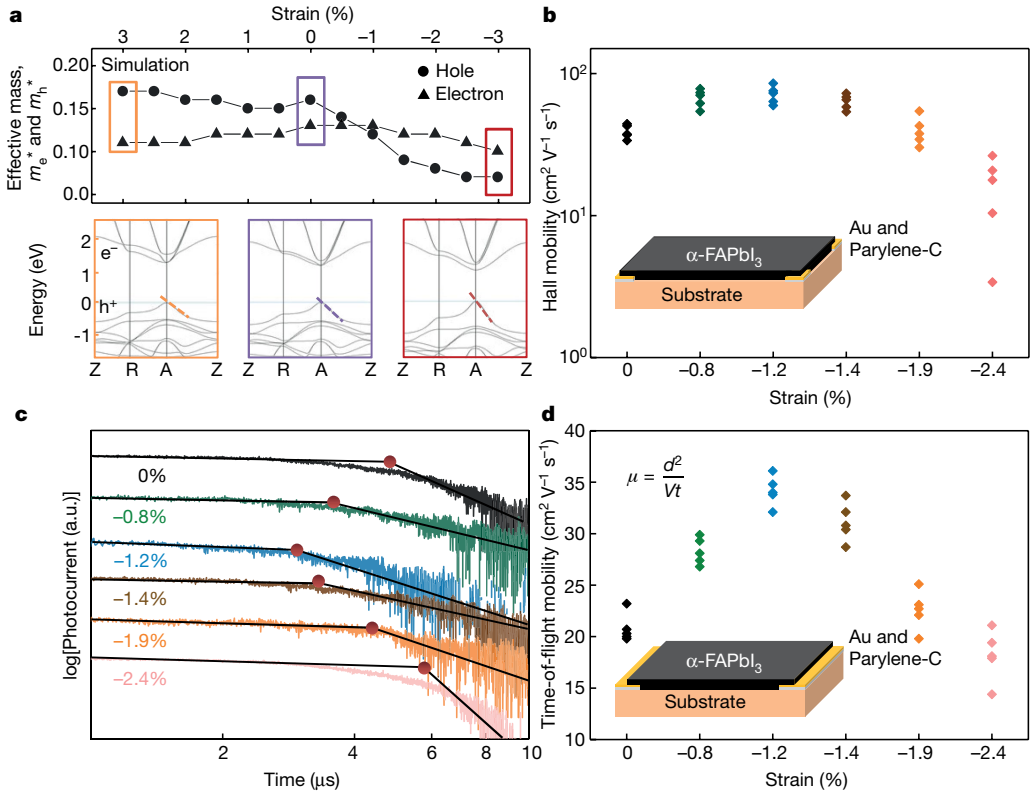

Fig. 3 | Electronic properties. a, Calculated effective masses of the carriers at different strains, and electronic bandstructures under three strain levels (3%, 0% and −3%). The electron effective mass (m_e^*) remains relatively stable with the change in strain, while the hole effective mass (m_h^*) decreases with increasing compressive strain. The dashed lines represent the dispersivity of the valence band; a less dispersive valence bandstructure indicates a smaller hole effective mass. The Z, R and A points are high-symmetry points in the first Brillouin zone of the tetragonal lattice. Bottom panels with coloured borders represent three typical examples with different strains. **b**, Hole mobilities by Hall effect measurements showing that α-$FAPbI_3$ with strain of −1.2% has the highest hole mobility. Coloured symbols correspond to the strain as in **c**. The decrease of the hole mobility with strain higher than −1.2% is attributed to the increase of dislocation density. Number of experiments, $n = 5$ for each strain. Inset, the structure of the measurement setup (gold, yellow; parylene-C, grey), not to scale. **c**, Transient photocurrent curves of the epitaxial α-$FAPbI_3$ under different strains. The transient photocurrent curves are plotted on a log–log scale. The carrier transit time—that is, the inflection point of the photocurrent curve—is marked by a solid red circle. The inflection point indicates the point at which the charge transport carriers switch from the majority to the minority carriers. Lines are guides to the eye. **d**, Plots of calculated carrier mobilities as a function of the strain magnitudes. The inset equation, $\mu = d^2/Vt$, transforms the carrier transit time to the carrier mobility, where μ is the calculated time-of-flight carrier mobility, d is the target region thickness, V is the applied voltage and t is the measured carrier transit time. Number of experiments, $n = 5$ for each strain. Inset, schematic measurement setup. Coloured symbols correspond to the strain as in **c**.

under both 0% and −2.4% strain shows a strong temperature dependence, owing to the soft nature of α-$FAPbI_3$ (Fig. 2c and Extended Data Fig. 4)[7]. The strained-sample bandgap is less temperature-dependent compared to that of the strain-free sample, because the smaller thermal expansion coefficient of the substrate compared to the epitaxial layer introduces a constraint[28] (detailed discussions in the Supplementary Information).

Ultraviolet photoelectron spectroscopy (UPS) reveals the bandstructure evolution of the α-$FAPbI_3$ under strain (see Fig. 2d for 0% and −2.4% strain and Extended Data Fig. 6 for other strains). All samples exhibit p-type behaviour (see Supplementary Information for more details). The Fermi level and the valence-band maximum (VBM) of the samples can be extracted from the UPS data. The results show that strain of −2.4% lifts the VBM upward by about 50 meV compared to the strain-free scenario. Considering the change in the bandgap (about 35 meV, Fig. 2a), the −2.4% strain pushes the conduction-band minimum (CBM) upward by about 15 meV compared to the strain-free scenario. The VBM mainly consists of lead 6*s* and iodine 5*p* orbitals, and the enhanced coupling between these orbitals under compressive strain pushes the VBM upward[29]. The CBM, which consists mostly of nonbonding localized states of Pb *p* orbitals, is less sensitive to the deformation of the PbI_6 octahedrons[7]. Therefore, the in-plane compressive strain increases the VBM more than it does the CBM.

The lattice deformation can alter the electronic bandstructure and therefore also the carrier dynamics. The effective mass of charge carriers can be assessed by the band curvature extracted from first-principles calculations[30]. Figure 3a shows the calculated results of the electron effective mass, m_e^*, and hole effective mass, m_h^* (the top panel) and three typical electronic bandstructures (the bottom panels) under different strains. On the one hand, the E–k dispersion of the conduction band remains relatively unaltered, and m_e^* shows only a slight variation under strain between 3% and −3%. On the other hand, compressive strain can modulate the E–k dispersion of the valence band and considerably reduce m_h^*.

To validate these calculations, Hall effect carrier mobilities of the α-$FAPbI_3$ thin films under strain of between 0% and −2.4% are measured (Fig. 3b). Finite element analysis simulation results show that potential carrier transfer from the substrate to the epitaxial layer is negligible, owing to an insulating layer (Parylene-C) and the energy barrier between the epitaxial layer and the substrate (Supplementary Fig. 10). All samples measured by the Hall effect show a p-type character, which is consistent with the UPS results. Of all strain levels tested, films under −1.2% strain on a $MAPbCl_{0.60}Br_{2.40}$ substrate have the highest hole mobility (Fig. 3b). Further increasing the strain results in a drastic drop in the hole mobility, because of the higher dislocation densities that arise at higher strain levels. We note that the devices for

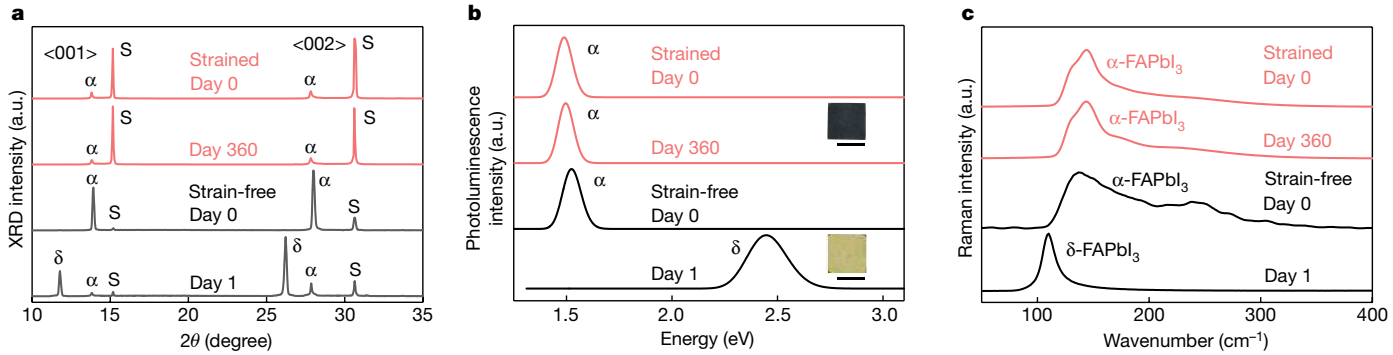

Fig. 4 | Epitaxial stabilization. a, Phase stability comparison of thin (sub-100 nm, −2.4% strained; pink) and thick (about 10 μm, strain-free; black) epitaxial α-$FAPbI_3$ on $MAPbCl_{1.50}Br_{1.50}$ substrates by XRD. α, α-$FAPbI_3$; δ, δ-$FAPbI_3$; S, substrate. The thin, strained sample shows better phase stability (red curves). For the thick, strain-free sample, the (001) peak for α-$FAPbI_3$ at 13.92° is the same as the strain-free sample in Supplementary Fig. 1a, which indicates that the top surface of the thick sample is fully relaxed (day 0, black curve). The X-ray can penetrate about 10–20 μm into the halide perovskites, which explains why the substrate peaks are more intense in the thin sample than in the thick sample. The thick, strain-free sample shows signs of a phase transition to δ-$FAPbI_3$ after 24 h (lower black curve). **b**, Phase stability study by photoluminescence spectroscopy. Re-measurement of the thin, strained sample after 360 d (lower pink curve) shows no obvious photoluminescence peak shift, but does show a slight decrease in peak intensity owing to its natural degradation into PbI_2 (ref. [16]). For the thick, strain-free sample, the photoluminescence spectrum shows an emission peak close to 1.52 eV, similar to that in the strain-free α-$FAPbI_3$ bulk crystal shown in Fig. 2a, indicating a full strain relaxation in the thick sample. Re-measurement after 24 h (lower black curve) shows that the thick film undergoes a transition from the α phase to the δ phase. Insets, optical images of the two samples, showing clear visual clues of the phase stability in the thin, strained sample (black α phase) and the phase transition in the thick, strain-free sample (yellow δ phase) after 24 h. Scale bars, 2 mm. **c**, Phase stability study by Raman spectroscopy. The Raman characteristics of the thin, strained sample show a peak at 143 cm^{-1} with no substantial difference after 360 d; the thick, strain-free sample (peak at 136 cm^{-1}) shows signs of a phase transformation to δ-$FAPbI_3$ after 24 h, as revealed by its signature peak at 108 cm^{-1}.

Hall effect measurements have an epitaxial-layer thickness larger than the critical thickness to ensure sufficient contact area between the halide perovskite and the bottom electrode. Therefore, a high strain level will induce a high concentration of dislocations that degrade the hole mobility.

To validate the Hall mobility, we carried out time-of-flight measurements. The transient photocurrents after single excitation are plotted logarithmically in Fig. 3c. The carrier transit time shows the smallest value of the film under −1.2% strain. The calculated carrier mobility is plotted as a function of the strain applied (Fig. 3d, see the Supplementary Information for calculation details), and shows a similar trend to that given by the Hall effect. We note that the absolute mobility values from the time-of-flight and Hall effect measurements differ, owing to experimental uncertainties in the type and quality of electronic contacts made during the fabrication processes[31]. The space-charge-limited-current method can quantify trap density[32]. Results show that a higher strain level leads to a higher trap density (Extended Data Fig. 7 and Supplementary Fig. 11), which explains the observed decrease in mobility under a higher strain magnitude. Capacitance–frequency (C–ω) spectroscopy is also used to cross-check the trap density (Supplementary Fig. 12), the results of which correspond well with those obtained by the space-charge-limited-current method.

It is widely accepted that α-$FAPbI_3$ crystals are metastable at room temperature and can quickly phase transform to photo-inactive δ-$FAPbI_3$ within approximately 24 h (ref. [16]), owing to its internal lattice strain and low entropy[19,33]. Existing strategies for α-$FAPbI_3$ stabilization, including alloying[26] and surface passivation[34], either widen the bandgap or raise the carrier transport barrier by introducing nonconductive ligands (detailed discussions in the Supplementary Information). However, the epitaxial α-$FAPbI_3$ thin film exhibits long-lasting phase stability at room temperature.

Figure 4a shows XRD results of a sub-100-nm epitaxial α-$FAPbI_3$ thin film that is stable for at least 360 d after growth (red curves in Fig. 4a). In the 10-μm epitaxial thick film (far beyond the threshold thickness at which the strain is fully relaxed), the stabilization effect disappears: after 24 h, XRD peaks from δ-$FAPbI_3$ can be detected (black curves in Fig. 4a). The phase stability of the strained α-$FAPbI_3$ is also verified by photoluminescence (Fig. 4b) and Raman spectroscopy (Fig. 4c). A possible stabilization effect from incorporating bromine or chlorine into the α-$FAPbI_3$ can be excluded, because those foreign ions would stabilize the α-phase regardless of the epilayer thickness. X-ray photoelectron spectroscopy (XPS) measurements showing the absence of bromine and chlorine provide additional evidence that this is not the origin of the stability (Extended Data Fig. 8).

The mechanism of the stable thin α-$FAPbI_3$ can be explained by two reasons. First, the interfacial energy of cubic α-$FAPbI_3$/cubic substrate is much lower than that of hexagonal δ-$FAPbI_3$/cubic substrate, which is the most critical factor for the stabilization effect (Supplementary Fig. 13, Supplementary Table 3, and see Supplementary Information for details). The epitaxial lattice is constrained to the substrate owing to the strong ionic bonds between them and, therefore, the lattice is restricted from the phase transition. Second, the driving force of the α-to-δ phase transition is believed to be the internal tensile strain in the α-$FAPbI_3$ unit cell, which can induce the formation of vacancies and subsequent phase transition[35]. In this study, the epitaxial film is under compressive strain, which neutralizes the effect of the internal tensile strain. Therefore, the synergistic effect of the low-energy coherent epitaxial interface and the neutralizing compressive strain are the key to α-$FAPbI_3$ stabilization. As a control, epitaxial α-$FAPbI_3$ thin film is removed from the substrate (Supplementary Fig. 14); the removed α-$FAPbI_3$ transforms to the δ phase within 24 h.

We demonstrate high-responsivity photodetectors as a use case of the strain engineered α-$FAPbI_3$ thin film. Figure 5a shows the current–voltage (I–V) characteristics of a strain-free device and a device under −1.2% strain. The dark current at −1 V in the strained device is around 15% higher than that in the strain-free one, indicating the higher defect density of the strained device. However, the photocurrent in the strained device increases by approximately 180% compared to the strain-free device. We attribute the photocurrent increase to higher carrier mobility and better alignment of VBM to the Fermi level of the gold electrode under compressive strain (Supplementary Fig. 15).

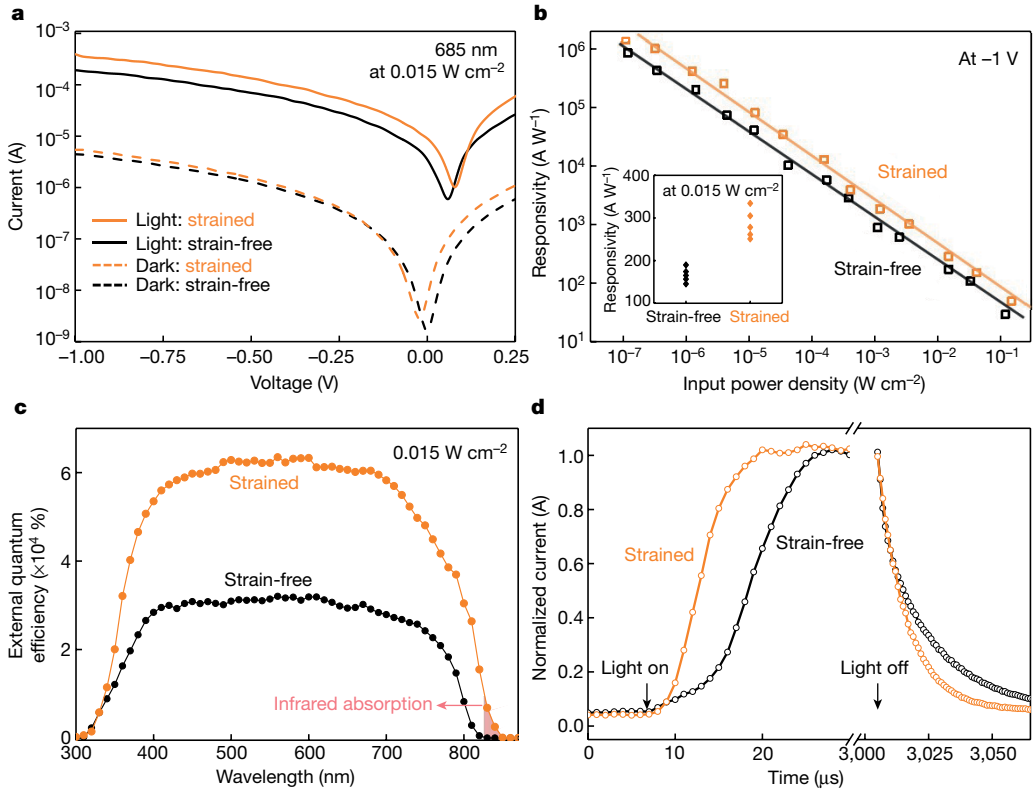

Fig. 5 | Photodetector characterizations of the α-FAPbI$_3$ thin films. **a**, *I*–*V* characteristics of Au/α-FAPbI$_3$/indium tin oxide photoconductor structured photodetectors. The dark current and photocurrent of the −1.2% strained detector are about 15% and 180% higher than those of its strain-free counterpart. Detectors are tested with a 685-nm laser under 0.015 W cm^{-2}. **b**, Comparison of responsivity of the −1.2% strained and strain-free photodetectors. The responsivity of both devices shows an increasing trend with decreasing incident power, as the chances of carrier recombination go down at low illumination intensities[36]. The strained device yields a higher responsivity owing to higher carrier mobility and better band alignment. Inset, the statistical average of the detector performance. Number of experiments, $n = 5$ for each strain value. **c**, External quantum efficiency spectra of the −1.2% strained and strain-free photodetectors showing that the strained photodetector yields a higher external quantum efficiency as well as a broader absorption spectrum (Extended Data Fig. 9d), owing to enhanced carrier mobility and bandgap reduction. **d**, Response times of the photodetectors, with faster rise and fall times for the −1.2% strained (9 μs and 34 μs) than the strain-free (14 μs and 50 μs) device due to the enhanced carrier mobility and transport.

Responsivity of the two photodetectors—defined as the change in photocurrent per unit of illumination intensity—is measured at various illumination intensities (Fig. 5b). The responsivity of the strained device, which reaches a maximum of 1.3×10^6 A W^{-1} at an incident power density of 1.1×10^{-7} W cm^{-2}, is almost twice of that of the strain-free device. This is again attributed to the enhanced carrier mobility and the better band alignment of the strained device. The responsivity of this strained device is, to our knowledge, the highest reported for a α-FAPbI$_3$ device under similar measurement conditions (for example, applied voltage and incident power (Supplementary Table 4)). Similar to the trend in Hall effect carrier mobility, the measured responsivity peaks at −1.2% strain (Extended Data Fig. 9a). Compressive strain also improves the detectivity and the gain of the photodetector (Extended Data Fig. 9b, c). Devices with a diode structure can reduce the dark current, but have a much lower responsivity: on average 500 times lower than that of the photoconductor-type device (Supplementary Fig. 16).

The strained device also shows an enhanced external quantum efficiency over the visible range (Fig. 5c), owing to the enhanced carrier mobility as well as more efficient carrier transport across the gold–perovskite interface. Additionally, after normalizing the spectra, a distinct response in the short-wave infrared region (>810 nm) can be identified for the strained device (Extended Data Fig. 9d), consistent with the photoluminescence measurements showing bandgap reduction under compressive strain. The rise and fall times of the strained device are around 30% shorter than those of the strain-free device, indicating a faster carrier dynamics (Fig. 5d).

Online content

Any methods, additional references, Nature Research reporting summaries, source data, extended data, supplementary information, acknowledgements, peer review information; details of author contributions and competing interests; and statements of data and code availability are available at https://doi.org/10.1038/s41586-019-1868-x.

1. Smith, C. S. Piezoresistance effect in germanium and silicon. *Phys. Rev.* **94**, 42–49 (1954).
2. Llordés, A. et al. Nanoscale strain-induced pair suppression as a vortex-pinning mechanism in high-temperature superconductors. *Nat. Mater.* **11**, 329–336 (2012).
3. Yang, W. S. et al. Iodide management in formamidinium-lead-halide-based perovskite layers for efficient solar cells. *Science* **356**, 1376–1379 (2017).
4. Lin, K. et al. Perovskite light-emitting diodes with external quantum efficiency exceeding 20 per cent. *Nature* **562**, 245–248 (2018).
5. Feng, J. et al. Single-crystalline layered metal-halide perovskite nanowires for ultrasensitive photodetectors. *Nat. Electron.* **1**, 404–410 (2018).
6. Lü, X. et al. Enhanced structural stability and photo responsiveness of $CH_3NH_3SnI_3$ perovskite via pressure-induced amorphization and recrystallization. *Adv. Mater.* **28**, 8663–8668 (2016).
7. Liu, G. et al. Pressure-induced bandgap optimization in lead-based perovskites with prolonged carrier lifetime and ambient retainability. *Adv. Funct. Mater.* **27**, 1604208 (2017).
8. Wang, Y. et al. Pressure-induced phase transformation, reversible amorphization, and anomalous visible light response in organolead bromide perovskite. *J. Am. Chem. Soc.* **137**, 11144–11149 (2015).
9. Chen, B. et al. Large electrostrictive response in lead halide perovskites. *Nat. Mater.* **17**, 1164 (2018).
10. Zhao, J. et al. Strained hybrid perovskite thin films and their impact on the intrinsic stability of perovskite solar cells. *Sci. Adv.* **3**, eaao5616 (2017).

11. Zhu, C. et al. Strain engineering in perovskite solar cells and its impacts on carrier dynamics. *Nat. Commun*. **10**, 815 (2019).
12. Steele, J. A. et al. Thermal unequilibrium of strained black $CsPbI_3$ thin films. *Science* **365**, 679–684 (2019).
13. Wang, Y. et al. Nontrivial strength of van der Waals epitaxial interaction in soft perovskites. *Phys. Rev. Mater*. **2**, 076002 (2018).
14. Li, X., et al. Residual nanoscale strain in cesium lead bromide perovskite reduces stability and shifts local luminescence. *Chem. Mater*. **31**, 2778–2785 (2019).
15. Wang, Y. et al. Defect-engineered epitaxial $VO_{2\pm\delta}$ in strain engineering of heterogeneous soft crystals. *Sci. Adv*. **4**, eaar3679 (2018).
16. Han, Q. et al. Single crystal formamidinium lead iodide ($FAPbI_3$): insight into the structural, optical, and electrical properties. *Adv. Mater*. **28**, 2253–2258 (2016).
17. Fang, Y., Dong, Q., Shao, Y., Yuan, Y. & Huang, J. Highly narrowband perovskite single-crystal photodetectors enabled by surface-charge recombination. *Nat. Photon*. **9**, 679–686 (2015).
18. Pohl, U. W. *Epitaxy of Semiconductors: Introduction to Physical Principles* (Springer, 2013).
19. Chen, T. et al. Entropy-driven structural transition and kinetic trapping in formamidinium lead iodide perovskite. *Sci. Adv*. **2**, e1601650 (2016).
20. Maculan, G. et al. $CH_3NH_3PbCl_3$ single crystals: inverse temperature crystallization and visible-blind UV-photodetector. *J. Phys. Chem. Lett*. **6**, 3781–3786 (2015).
21. Rakita, Y., Cohen, S. R., Kedem, N. K., Hodes, G. & Cahen, D. Mechanical properties of $APbX_3$ (A= Cs or CH_3NH_3; X= I or Br) perovskite single crystals. *MRS Commun*. **5**, 623–629 (2015).
22. Steele, J. A. et al. Direct laser writing of δ- to α-phase transformation in formamidinium lead iodide. *ACS Nano* **11**, 8072–8083 (2017).
23. Li, D. et al. Size-dependent phase transition in methylammonium lead iodide perovskite microplate crystals. *Nat. Commun*. **7**, 11330 (2016).
24. Sarmah, S. P. et al. Double charged surface layers in lead halide perovskite crystals. *Nano Lett*. **17**, 2021–2027 (2017).
25. Kanemitsu, Y. Luminescence spectroscopy of lead-halide perovskites: materials properties and application as photovoltaic devices. *J. Mater. Chem. C* **5**, 3427–3437 (2017).
26. Xie, L.-Q. et al. Understanding the cubic phase stabilization and crystallization kinetics in mixed cations and halides perovskite single crystals. *J. Am. Chem. Soc*. **139**, 3320–3323 (2017).
27. Katan, C., Mohite, A. D. & Even, J. Entropy in halide perovskites. *Nat. Mater*. **17**, 377–379 (2018).
28. Ge, C. et al. Ultralow thermal conductivity and ultrahigh thermal expansion of single-crystal organic–inorganic hybrid perovskite $CH_3NH_3PbX_3$ (X = Cl, Br, I). *J. Phys. Chem. C* **122**, 15973–15978 (2018).
29. Yin, W.-J., Yang, J.-H., Kang, J., Yan, Y. & Wei, S.-H. Halide perovskite materials for solar cells: a theoretical review. *J. Mater. Chem. A* **3**, 8926–8942 (2015).
30. Giorgi, G., Fujisawa, J.-I., Segawa, H. & Yamashita, K. Small photocarrier effective masses featuring ambipolar transport in methylammonium lead iodide perovskite: a density functional analysis. *J. Phys. Chem. Lett*. **4**, 4213–4216 (2013).
31. Herz, L. M. Charge-carrier mobilities in metal halide perovskites: fundamental mechanisms and limits. *ACS Energy Lett*. **2**, 1539–1548 (2017).
32. Dong, Q. et al. Electron-hole diffusion lengths > 175 μm in solution-grown $CH_3NH_3PbI_3$ single crystals. *Science* **347**, 967–970 (2015).
33. Zheng, X. et al. Improved phase stability of formamidinium lead triiodide perovskite by strain relaxation. *ACS Energy Lett*. **1**, 1014–1020 (2016).
34. Fu, Y. et al. Stabilization of the metastable lead iodide perovskite phase via surface functionalization. *Nano Lett*. **17**, 4405–4414 (2017).
35. Saidaminov, M. I. et al. Suppression of atomic vacancies via incorporation of isovalent small ions to increase the stability of halide perovskite solar cells in ambient air. *Nat. Energy* **3**, 648–654 (2018).
36. Liu, Y. et al. A 1300 mm_2 ultrahigh-performance digital imaging assembly using high-quality perovskite single crystals. *Adv. Mater*. **30**, 1707314 (2018).

Methods

Precursor synthesis

Methylammonium bromine (MABr) was synthesized as the precursor for the substrate growth. First, 20 ml methylamine (40% in methanol, Tokyo Chemical Industry) and 21.2 ml hydrobromic acid (48 wt% in water, Sigma Aldrich) were mixed in an ice bath and the temperature was maintained for the reaction to continue for 2 h. The mixture was heated to 80 °C to evaporate the solvent. The precipitate was dissolved in anhydrous ethanol (Sigma Aldrich) at 80 °C and cooled down for recrystallization. The crystals were then centrifuged with diethyl ether and dried at 80 °C overnight.

Crystal growth

Methylammonium lead chloride ($MAPbCl_3$) solution was prepared by mixing 0.6752 g of methylammonium chloride (MACl, 98%, Tokyo Chemical Industry) and 2.781 g lead chloride ($PbCl_2$, 99%, Alfa Aesar) in a mixed solution of 5 ml anhydrous dimethylformamide (99.8%, Aldrich) and 5 ml anhydrous dimethyl sulfoxide (DMSO, 99.8%, Aldrich). Methylammonium lead bromine ($MAPbBr_3$) solution was prepared by mixing 1.120 g MABr and 3.670 g lead bromine ($PbBr_2$, 98%, Acros) in 10 ml dimethylformamide. The $MAPbCl_3$ and $MAPbBr_3$ solutions were mixed with different ratios. The mixed solutions were kept at room temperature to slowly evaporate the solvent, and single crystals were collected to use as substrates. $FAPbI_3$ solutions were prepared by mixing formamidinium iodide (FAI, 99.9%, Greatcell Solar) and lead iodide (PbI_2, 99.99%, Tokyo Chemical Industry) at a molar ratio of 1:1 in anhydrous gamma-butyrolactone (Sigma Aldrich) with different concentrations. Strain-free α-$FAPbI_3$ single crystals were obtained by heating the $FAPbI_3$ solutions to 120 °C.

Epitaxial growth

The substrates were heated to different temperatures, and the preheated $FAPbI_3$ solutions (at 100 °C) were then deposited onto the substrates for epitaxial growth.

Structural and optical characterizations

SEM images were taken with a Zeiss Sigma 500 SEM operated at 3 kV. The $2\theta/\omega$ XRD patterns, the rocking curve (ω scan), and the asymmetrical reciprocal space mapping around the (104) reflection of the substrate were measured by a Rigaku Smartlab diffractometer equipped with a copper $K\alpha_1$ radiation source ($\lambda = 0.15406$ nm) and a germanium (220 × 2) monochromator. The unit cell parameters (a, c) for (104) reflection reciprocal space mapping were converted from (Q_x, Q_z) by $a = 1/Q_x$, $c = 4/Q_z$. Raman and photoluminescence spectra were measured by a Raman spectrometer (Renishaw inVia). Raman peak fitting was done by the Renishaw inVia software. Atomic force microscopy was carried out by a scanning probe microscope (Veeco) in a tapping mode. XPS and UPS were carried out by a Kratos AXIS Supra with an aluminium Kα anode source and a He I (21.22 eV) source, respectively. Measurements were operated under a chamber pressure of 10^{-8} torr. XPS data were calibrated with the $c1s$ peak (284.8 eV). If not otherwise specified, bulk α-$FAPbI_3$ single crystals were used as the strain-free samples for structural and optical characterizations.

Device fabrication

Devices with a vertical structure were fabricated based on a lithography-based method[37]. Parylene-C (50 nm) and gold (50 nm) were sequentially deposited on the substrates, followed by a photolithography process with photoresist AZ-1512. The pattern was composed of an array of 2-μm-diameter circles (exposed) with 1 μm interdistance (covered by photoresist). The gold was chemically etched with wet etchants and the Parylene-C was precisely etched by reactive ion etching. The etched substrates underwent secondary growth in their corresponding growth solutions so that the substrate surface reached the same height as the electrode. Epitaxial growth on the patterned substrate enabled the α-$FAPbI_3$ crystals to initiate from the exposed patterns and gradually merge into a thin film with a controllable thickness. We note that the $MAPbCl_xBr_{3-x}$ substrates were used for the strained devices (heteroepitaxy) and α-$FAPbI_3$ substrates were used for the strain-free devices (homoepitaxy). The top electrodes were then deposited by sputtering (for indium tin oxide, 200 nm). For vertical devices, the area of the top electrode was controlled to be $1 \times 1\ mm^2$ using a shadow mask. For planar devices, Parylene-C (50 nm) and the electrode (gold, 50 nm) were deposited using a shadow mask with designed electrode layouts.

Electrical characterizations

Space-charge-limited-current measurements were carried out by a source meter (Keithley 2400) and a customized probe station in a dark environment. Devices with an Au/Perovskite/Au structure were used. C–ω measurements were carried out by a parameter analyser (B1500, Agilent) in a dark environment. Devices with an Au/perovskite/indium tin oxide structure were used. The thickness of α-$FAPbI_3$ of all devices for space-charge-limited current and C–ω measurements was controlled to be 500 nm. Hall effect measurements were carried out with a Lake Shore Hall measurement system (HM 3000) using the van der Pauw method. We note that the Parylene-C layer prevented direct contact between the substrate and electrodes, eliminating possible carriers extracted from the substrate. The thickness of the α-$FAPbI_3$ for all devices for Hall effect measurement was controlled to be 500 nm. For the time-of-flight measurement, a 685-nm-pulse laser ($10\ mW\ cm^{-2}$) with $<10^{-10}$-s pulse width was used as the light source. Photoresponse was measured with an oscilloscope (MSO6104A Channel Mixed Signal, Agilent). An external bias of 1 V was applied to drive the carriers in the device while a 1-MΩ resistor was connected in series to simulate the open-circuit condition so that the carriers were effectively blocked in the devices[32]. The measurement was carried out in the dark while the bias and the laser power were kept constant. The experiment setup followed the reported time-of-flight measurement of halide perovskite single crystals[32,38–40]. The α-$FAPbI_3$ thickness of all devices for time-of-flight measurements was also controlled to be 500 nm.

Photodetector characterizations

Devices with the structure shown in Supplementary Figs. 15 and 16 were used. A 685-nm laser was used as the light source. The I–V characteristics were collected on a probe station with an Agilent B2912A source meter.

First-principles calculations

First-principles density functional theory calculations were performed using the Vienna ab initio Simulation Package (VASP)[41]. Electron–ion interactions were described using the Projector Augmented Wave pseudopotential[42]. The electron–electron exchange-correlation functional was treated using the Generalized Gradient Approximation parametrized by Perdew, Burke and Ernzerhof[43]. For bandgap calculations, spin–orbit coupling was incorporated owing to the heavy element Pb, and the hybrid functionals within Heyd–Scuseria–Ernzerhof formalism with 25% Hartree–Fock exchange were employed. A cutoff energy of 400 eV for the plane-wave basis set was used. All structures were fully optimized until all components of the residual forces were smaller than $0.01\ eV\ Å^{-1}$. The convergence threshold for self-consistent-field iteration was set at 10^{-5} eV. For optimization of the cubic lattice parameter, a Γ-centred 3 × 3 × 3 k-point mesh was used. A denser k-point mesh of 4 × 4 × 4 was used to obtain accurate energies and electronic structures for strained cells. For optimization and static calculations of the heterostructural models, Γ-centred 4 × 4 × 1 and 5 × 5 × 1 k-point meshes were used, respectively. Raman intensities were calculated by the CASTEP module in Materials Studios[44] with a 3 × 3 × 3 k-point mesh and a 400 eV cutoff energy.

Finite element analysis simulations

Simulation of the current density was done by the multiphysics analysis in COMSOL (version 5.4; www.comsol.com). Simulation of the elastic strain relaxation was done by the ABAQUS[45].

Data availability

The data that support the findings of this study are available from the corresponding authors on reasonable request.

37. Lei, Y. et al. Controlled homoepitaxial growth of hybrid perovskites. *Adv. Mater*. **30**, 1705992 (2018).
38. Shi, D. et al. Low trap-state density and long carrier diffusion in organolead trihalide perovskite single crystals. *Science* **347**, 519–522 (2015).
39. Pospisil, J. et al. Density of bulk trap states of hybrid lead halide perovskite single crystals: temperature modulated space-charge-limited-currents. *Sci. Rep*. **9**, 3332 (2019).
40. Saidaminov, M. I. et al. High-quality bulk hybrid perovskite single crystals within minutes by inverse temperature crystallization. *Nat. Commun*. **6**, 7586 (2015).
41. Kresse, G. & Furthmüller, J. Efficient iterative schemes for ab initio total-energy calculations using a plane-wave basis set. *Phys. Rev. B* **54**, 11169–11186 (1996).
42. Blöchl, P. E. Projector augmented-wave method. *Phys. Rev. B* **50**, 17953–17979 (1994).
43. Perdew, J. P., Burke, K. & Ernzerhof, M. Generalized gradient approximation made simple. *Phys. Rev. Lett*. **77**, 3865–3868 (1996).
44. Clark, S. et al. First principles methods using CASTEP. *Z. Kristallogr*. **220**, 567–570 (2005).
45. Smith, M. *ABAQUS/Standard User's Manual* Version 6.9 (Dassault Systèmes Simulia Corp, 2009).

Acknowledgements We thank T. N. Ng and Z. Wu for guidance on the transient photocurrent measurement; P. Liu and S. Yu for sharing the Rikagu Smartlab diffractometer; D. P. Fenning and X. Li for discussions; Q. Lin for guidance on the reciprocal space mapping measurements; S. Wang for analysis and discussions of the UPS; Y. Zeng for training on the Renishaw inVia Raman spectrometer; Y. Li, Y. Yin and M. Chen for guidance on the finite element analysis simulations; and S. Xiang for constructive feedback on manuscript preparation. This work was supported by the startup fund by the University of California San Diego. The microfabrication involved in this work was performed at the San Diego Nanotechnology Infrastructure (SDNI) of UCSD, a member of the National Nanotechnology Coordinated Infrastructure, which was supported by the the National Science Foundation (grant number ECCS-1542148). K.Y. acknowledges the National Science Foundation under award number ACI-1550404 and computational resources from Extreme Science and Engineering Discovery Environment (XSEDE), which is supported by National Science Foundation grant number ACI-1548562.

Author contributions S.X. and Y.C. conceived the idea. Y.C. and Y. Lei prepared the samples. Y.C. and Y. Lei took the optical and SEM images. Y.C., J.S. and M.-H.C. carried out the XRD, Raman and photoluminescence spectroscopy characterizations. R.R. and A.E.I. contributed to the temperature-dependent photoluminescence characterizations. Y. Li and J.S. carried out the density functional theory calculations. Y.C. and W.C. carried out the finite element analysis simulations. Y.C., Y. Lei, Y.G., C.W. and J.C. contributed to the device fabrication. Y.C., Y.Y. and W.C. carried out the mobility measurements. Y.C. carried out the trap density measurements. Y.C. and Y.Y. carried out the photodetectors characterizations. All authors contributed to analysing the data and commenting on the manuscript.

Competing interests The authors declare no competing interests.

Additional information
Supplementary information is available for this paper at https://doi.org/10.1038/s41586-019-1868-x.
Correspondence and requests for materials should be addressed to S.X.
Peer review information *Nature* thanks Jian Shi, Lijun Zhang and the other, anonymous, reviewer(s) for their contribution to the peer review of this work.
Reprints and permissions information is available at http://www.nature.com/reprints.

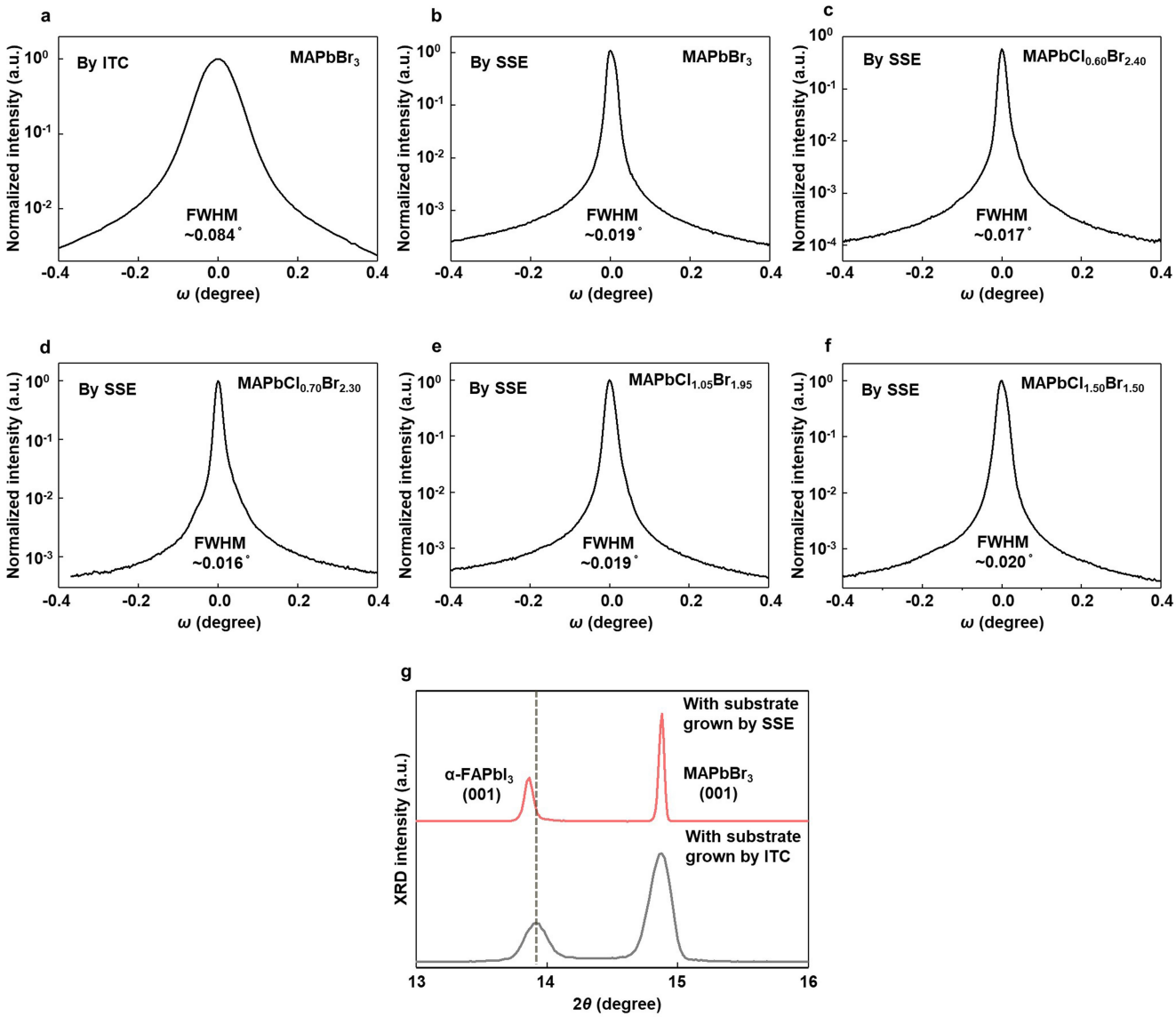

Extended Data Fig. 1 | Characterization of substrate quality with different growth methods and its impact on the epitaxial strain. a–**f**, Rocking curve measurements of substrates grown by the inverse temperature crystallization (ITC) and slow solvent evaporation (SSE) methods. Lower full-width at half-maximum (FWHM) values by the SSE indicate better crystal quality. **g**, XRD patterns of strained α-$FAPbI_3$ on a substrate with higher crystal quality (red curve) and relaxed α-$FAPbI_3$ on a substrate with lower crystal quality (grey curve). Dislocations in the substrates can propagate into and relax the strain in the epitaxial α-$FAPbI_3$. The vertical dash line labels the (001) peak position of strain-free α-$FAPbI_3$. The peak position from the strain-relaxed $FAPbI_3$ (grey curve) shifts back to that of strain-free α-$FAPbI_3$.

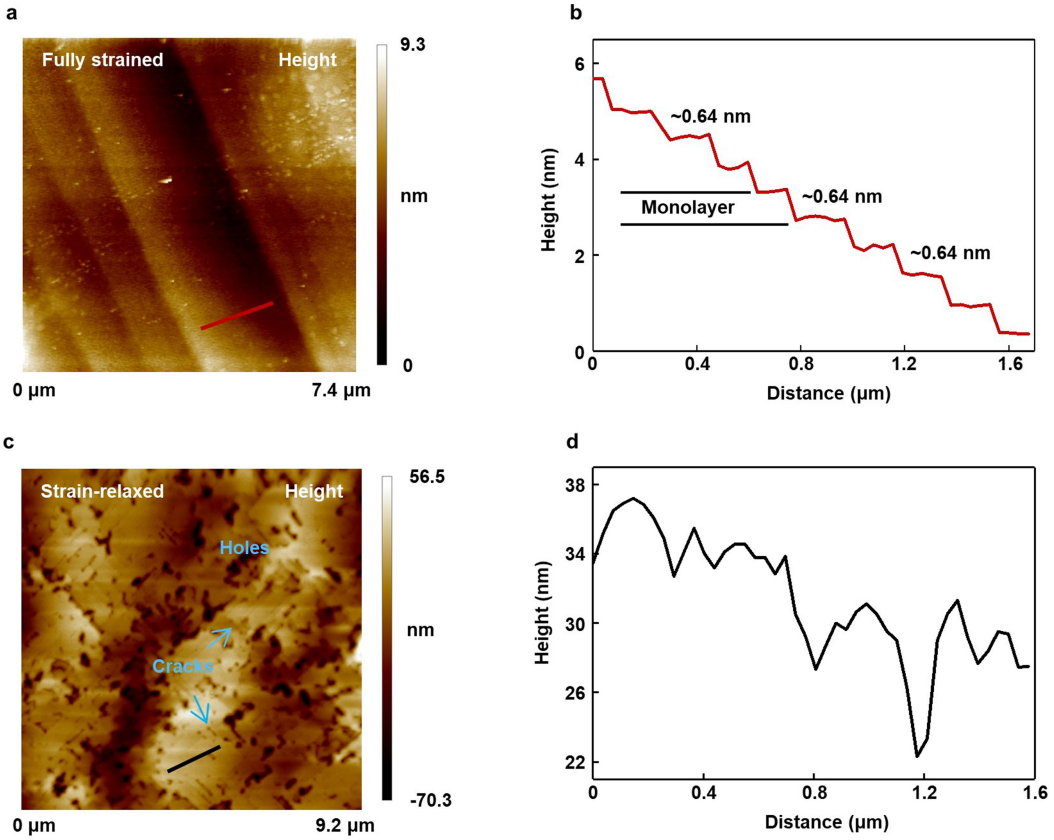

Extended Data Fig. 2 | Atomic force microscopy morphology characterization of strained and strain-relaxed epitaxial α-$FAPbI_3$ films. **a**, **b**, A topography image (**a**) and the corresponding height scanning curve (**b**) of the red line in **a** of a strained epitaxial α-$FAPbI_3$ thin film. **c**, **d**, A topography image (**c**) and the corresponding height scanning curve (**d**) of the black line in **c** of a strain-relaxed epitaxial α-$FAPbI_3$ thick film. Results show that the strained thin film adopts a layer-by-layer growth model. No cracks or holes can be detected. As the film thickness increases, the total strain energy builds up and generates dislocations that propagate throughout the film and relax the strain, leading to the formation of cracks and holes. These cracks and holes are typically regarded as a signature of strain relaxation.

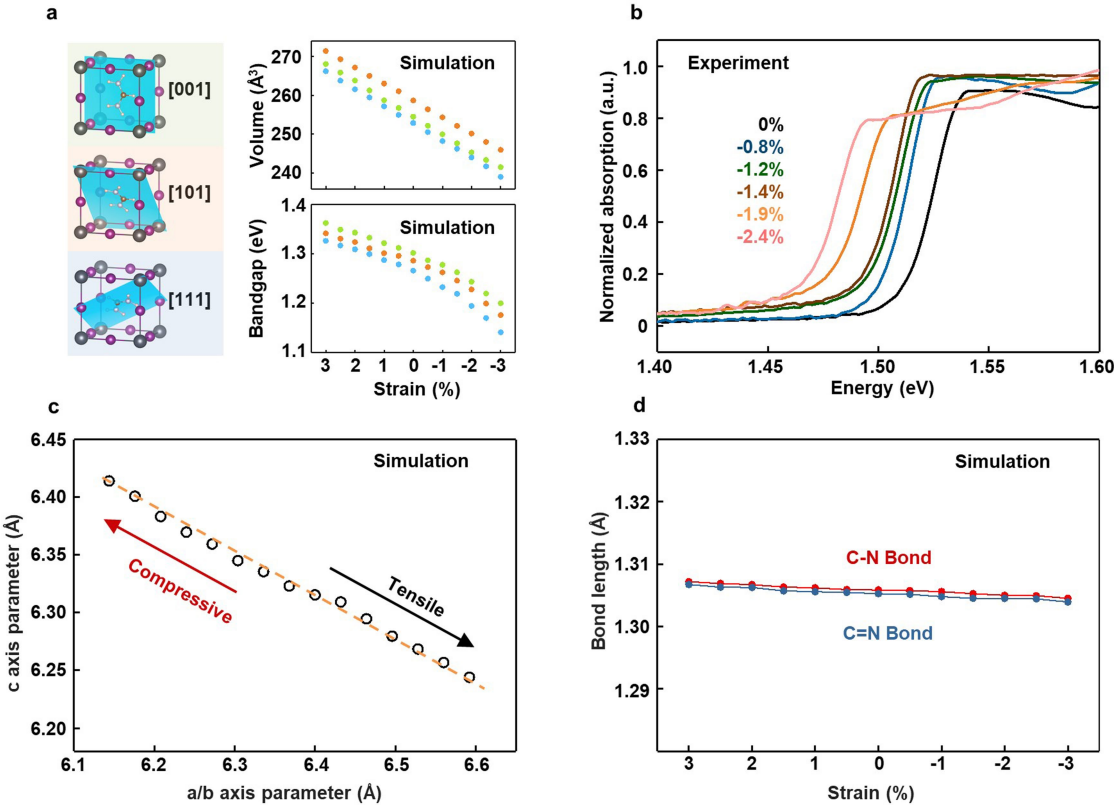

Extended Data Fig. 3 | First-principles calculations of the strained α-$FAPbI_3$ unit cell and experimental absorption spectra of the strained α-$FAPbI_3$ under different strains. a, Evolution of lattice volume and bandgap as a function of strain for three α-$FAPbI_3$ lattices with different FA^+ organic cation orientations. For the bandgap calculations, spin–orbit coupling is incorporated owing to the heavy element Pb, and the hybrid functionals within Heyd–Scuseria–Ernzerhof formalism with 25% Hartree–Fock exchange are employed. **b**, The absorption spectra of the strained α-$FAPbI_3$ thin films. The absorption onset redshifts will the increasing strain, which agrees with the photoluminescence spectra and prove that the strain can alter the bandgap of the α-$FAPbI_3$. **c**, The *c* axis length of the unit cell when biaxially straining the *a*/*b* axes. The slope of the fitted line shows a Poisson's ratio of about 0.3. **d**, C–N and C=N bond lengths at different strain levels. Simulation results show that the deformation of the FA^+ skeleton is very small under the applied biaxial strain.

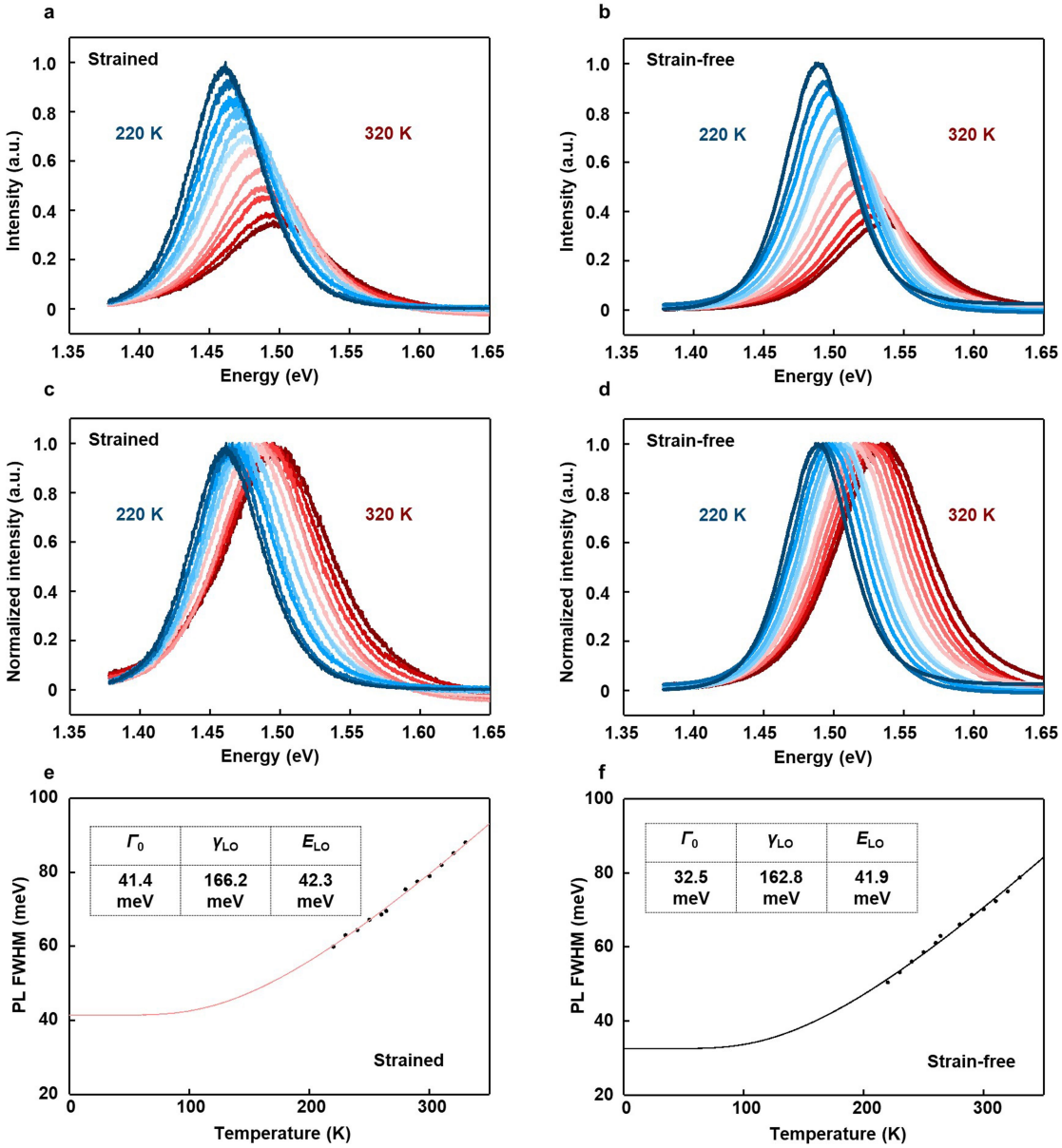

Extended Data Fig. 4 | Temperature-dependent photoluminescence measurement. a, **b**, Temperature-dependent photoluminescence of strained (**a**) and strain-free (**b**) α-$FAPbI_3$ before normalization. **c**, **d**, Temperature-dependent photoluminescence of strained (**c**) and strain-free (**d**) α-$FAPbI_3$ after normalization. Both samples exhibited uniform bandgap narrowing and FWHM narrowing with decreasing the temperature. **e**, **f**, Temperature-dependent photoluminescence (PL) FWHM of strained (**e**) α-$FAPbI_3$ and strain-free (**f**) α-$FAPbI_3$ with fitting. Results show that the strained α-$FAPbI_3$ has a higher Γ_0, γ_{LO} and E_{LO} than that of strain-free α-$FAPbI_3$ owing to the strain-induced crystalline quality reduction and the strain-enhanced carrier-phonon scattering. Γ_0, temperature-independent emission linewidth term associated with the structural disorder scattering. γ_{LO}, charged-carrier-optical-phonon coupling constant. E_{LO}, optical phonon energy.

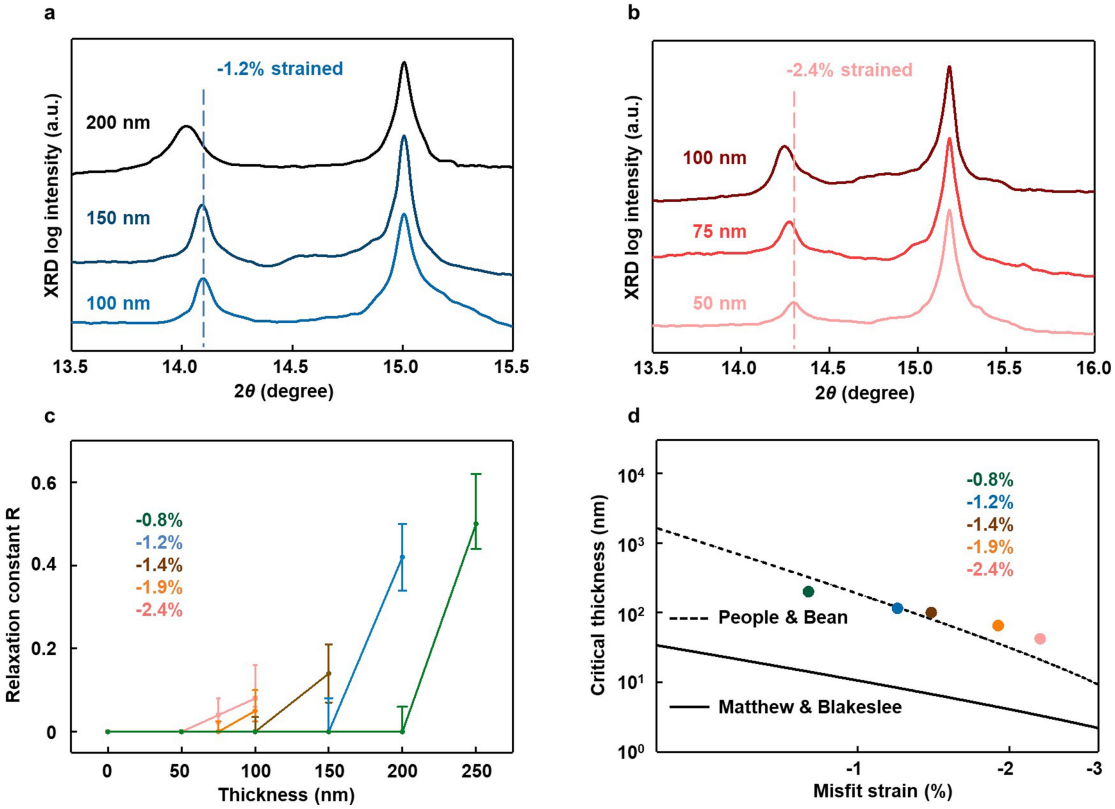

Extended Data Fig. 5 | Plastic strain relaxation study of the epitaxial α-FAPbI$_3$ thin films. a, **b**, Thickness-dependent in-plane XRD of −1.2% strained (**a**) and −2.4% strained (**b**) α-FAPbI$_3$ thin films. Vertical lines label the peak position of the fully strained films. Plastic strain relaxation at relatively high thickness can be evident by the peak shifting to lower angle and peak broadening. **c**, Thickness-dependent relaxation constant *R* of the epitaxial α-FAPbI$_3$ thin films with different strains. Results show that the critical thickness decreases with increasing strain. **d**, Fitting of the experimental critical thicknesses with the People and Bean and the Matthew and Blakeslee models (see Supplementary Information refs 69 and 70). Experimental results agree well with the People and Bean model, indicating that the plastic strain relaxation due to the dislocations generated during the epitaxial growth is the dominating relaxation mechanism.

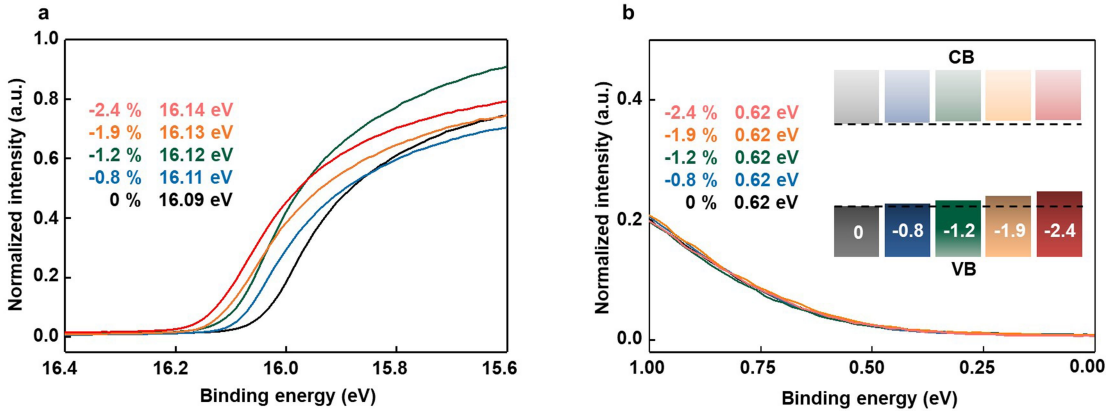

Extended Data Fig. 6 | UPS spectra of α-FAPbI$_3$ under different strains. a, The intersects of the curves with the baseline in the high-binding-energy region give the Fermi level position of corresponding strained α-FAPbI$_3$ films. There is a clear shift of the intersects to higher-binding-energy levels when the compressive strain becomes larger. **b**, The intersects of the curves with the baseline in the low-binding-energy region give the energy difference between the Fermi level and the VBM. All α-FAPbI$_3$ films have p-type character according to the calculated Fermi level position in the bandgap. Meanwhile, the VBM is pushed up more than the CBM with increasing strain. Inset, a schematic band diagram of the α-FAPbI$_3$ under different strains.

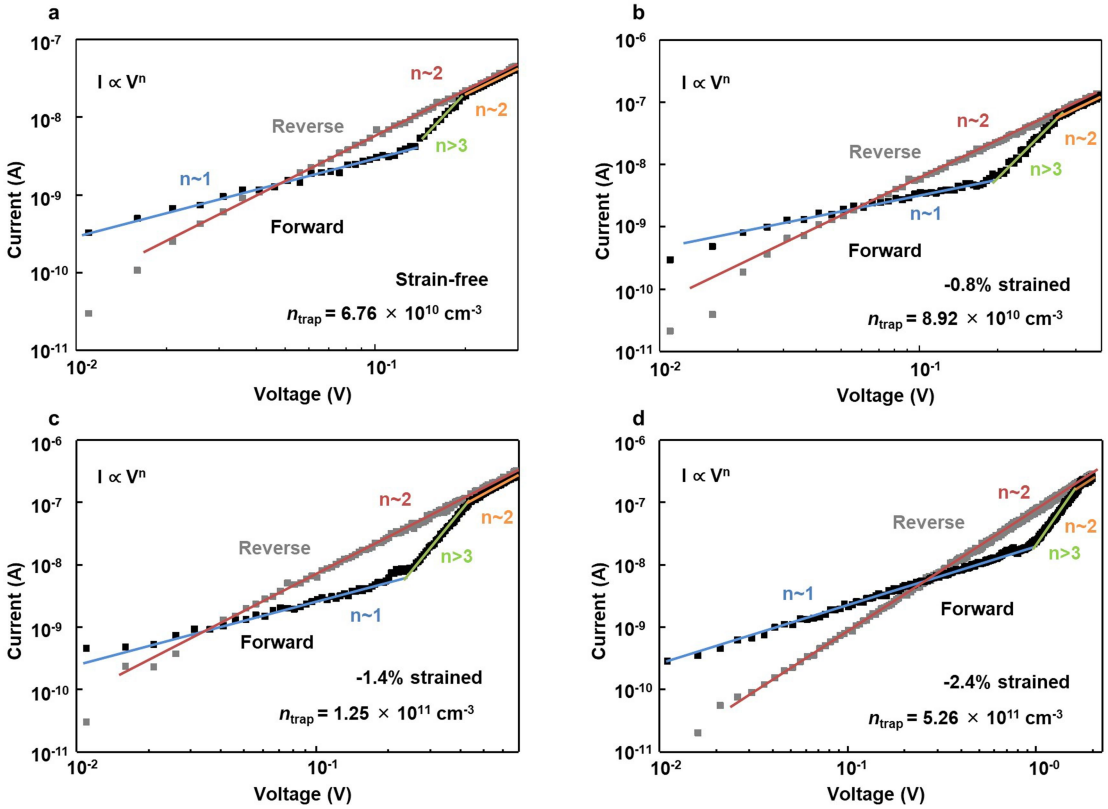

Extended Data Fig. 7 | Space-charge-limited-current measurement of the epitaxial α-FAPbI$_3$ with different strains. a–**d**, *I*–*V* characteristic curves for the space-charge-limited-current measurement of the epitaxial α-FAPbI$_3$ film with different strains. While the forward scans indicate a typical trap-filling process with increasing the applied voltage, the reverse scan doesn't show a detrapping process. Number of experiments, $n = 5$ for each strain value. n_{trap}, calculated trap density.

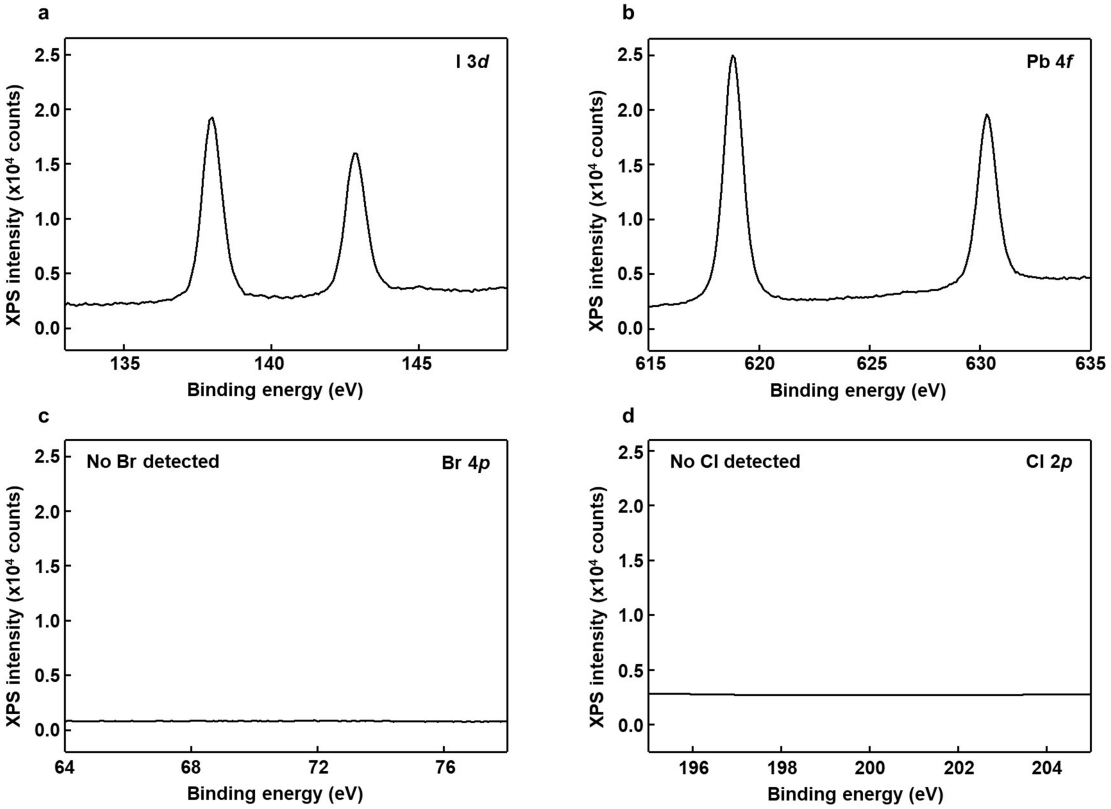

Extended Data Fig. 8 | XPS spectra of strained α-$FAPbI_3$. XPS spectra of: **a**, I 3*d*; **b**, Pb 4*f*; **c**, Br 4*p*; and **d**, Cl 2*p* photoelectrons from a strained α-$FAPbI_3$ film. Results show that Br and Cl are absent in the strained α-$FAPbI_3$.

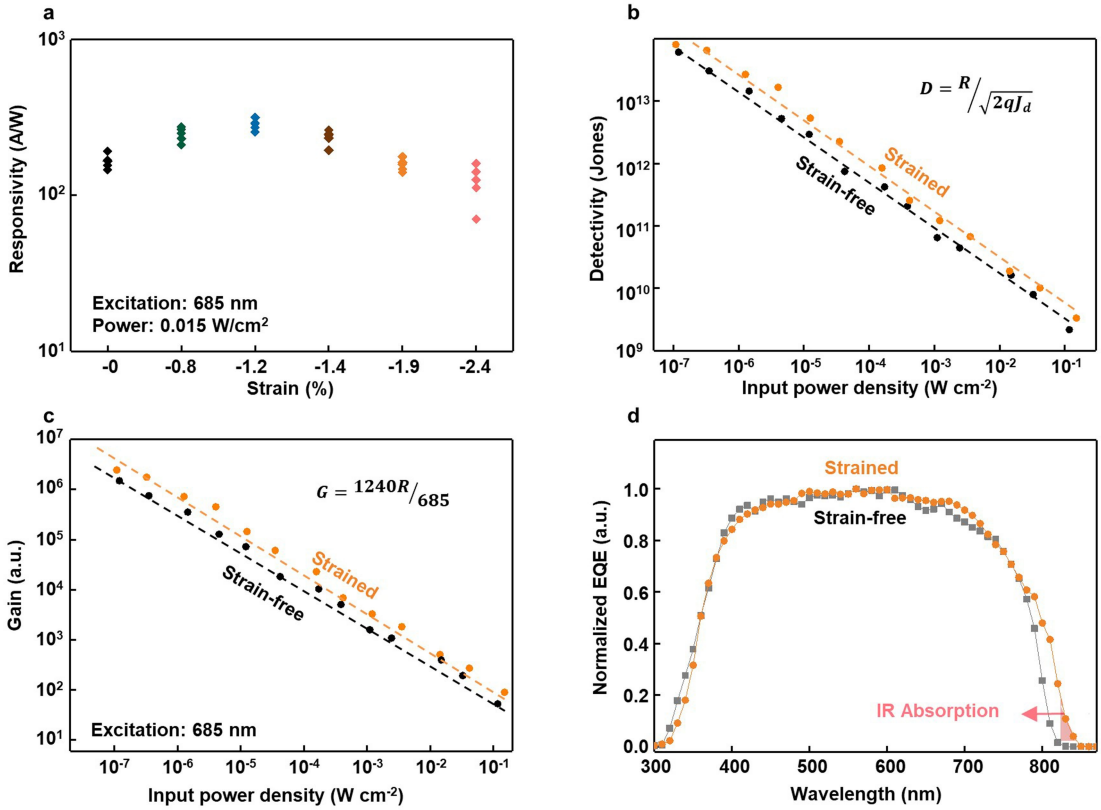

Extended Data Fig. 9 | Photoconductor-type photodetector characterizations with a 685-nm laser. a, Responsivity as a function of strain level in α-$FAPbI_3$. Devices under −0.8%, −1.2% and −1.4% compressive strain give better responsivity compared to the strain-free devices. Further increasing the compressive strain can lead to a higher density of dislocations, which reduces the responsivity. Number of experiments, $n = 5$ for each strain value. **b**, **c**, Detectivity (**b**) and gain G (**c**) of the photodetector based on α-$FAPbI_3$ under −1.2% strain, indicating enhanced performance. q, element charge. J_d, dark current density. **d**, Normalized external quantum efficiency (EQE) of the photodetector based on α-$FAPbI_3$ under −1.2% strain, showing an extended infrared absorption range.

nature

https://doi.org/10.1038/s41586-019-1868-x

Supplementary information

Strain engineering and epitaxial stabilization of halide perovskites

In the format provided by the authors and unedited

Yimu Chen, Yusheng Lei, Yuheng Li, Yugang Yu, Jinze Cai, Ming-Hui Chiu, Rahul Rao, Yue Gu, Chunfeng Wang, Woojin Choi, Hongjie Hu, Chonghe Wang, Yang Li, Jiawei Song, Jingxin Zhang, Baiyan Qi, Muyang Lin, Zhuorui Zhang, Ahmad E. Islam, Benji Maruyama, Shadi Dayeh, Lain-Jong Li, Kesong Yang, Yu-Hwa Lo & Sheng Xu

Supplementary Information for:

Strain engineering and epitaxial stabilization of halide perovskites

Yimu Chen[1,8], Yusheng Lei[1,8], Yuheng Li[1], Yugang Yu[2], Jinze Cai[2], Ming-Hui Chiu[3], Rahul Rao[4], Yue Gu[2], Chunfeng Wang[1], Woojin Choi[5], Hongjie Hu[2], Chonghe Wang[1], Yang Li[1], Jiawei Song[2], Jingxin Zhang[2], Baiyan Qi[2], Muyang Lin[1], Zhuorui Zhang[1], Ahmad E. Islam[4], Benji Maruyama[4], Shadi Dayeh[1,2,5], Lain-Jong Li[3,6], Kesong Yang[1], Yu-Hwa Lo[2,5], Sheng Xu[1,2,5,7*]

[1]Department of Nanoengineering, University of California San Diego, La Jolla, CA 92093, USA.

[2]Materials Science and Engineering Program, University of California San Diego, La Jolla, CA 92093, USA.

[3]Physical Science and Engineering Division, King Abdullah University of Science and Technology, Thuwal, 23955, Kingdom of Saudi Arabia.

[4]Materials and Manufacturing Directorate, Air Force Research Laboratory, Wright Patterson Air Force Base, Dayton, Ohio 45433, USA.

[5]Department of Electrical and Computer Engineering, University of California San Diego, La Jolla, CA 92093, USA.

[6]School of Materials Science and Engineering, University of New South Wales, Sydney 2052, Australia.

[7]Department of Bioengineering, University of California San Diego, La Jolla, CA 92093, USA.

[8]These authors contributed equally: Yimu Chen, Yusheng Lei.

*e-mail: shengxu@ucsd.edu

Supplementary Discussion 1: Current Methods to Strain Halide Perovskites

Strain engineering of halide perovskites is now receiving increasing attention in the field to improve the device performance by understanding device physics and improving materials quality. Different from the conventional semiconductors and perovskite oxides, the controllable strain engineering by heteroepitaxial growth of halide perovskites has not been achieved yet, to the authors' best knowledge, which is due to inappropriate growth methods and the absence of suitable lattice-mismatched substrates, therefore the lack of strong chemical bonds formed with the substrates.

Epitaxial growth of halide perovskites has been reported by many groups, but most of the works have been van der Waals epitaxy that is absent from strong interfacial chemical bonds[1-3]. Despite the weak nature of van der Waals bonds, nontrivial effects from van der Waals interaction to the epitaxial halide perovskites have been demonstrated due to the soft nature of halide perovskites[4]. Besides van der Waals epitaxy, chemical epitaxy by forming interfacial ionic bonds has also been reported[5,6]. However, due to the extremely high growth temperature (~500 °C), the interface was destroyed by the high diffusion rate of ions at such a high temperature and therefore, no interfacial strain could be detected. Other than epitaxial strain, thermally strained halide perovskites have also been studied. The thermal expansion coefficient difference between a patterned substrate and the halide perovskite was utilized to induce thermal strain to a perovskite microcrystal[7]. A thermally strained halide perovskite by introducing a phase transition of the substrate via increasing the temperature has also been demonstrated[8]. In this case, the thermal strain is highly dependent on the temperature and the magnitude of the strain cannot be well controlled.

Besides manipulating single crystalline halide perovskites, researchers are also creating strain in polycrystalline thin films by a variety of methods. One of the most popular methods is the ion substitution of a larger/smaller ion that can induce local tensile/compressive strain in the perovskite lattice[9,10]. Local compressive strain by small ion substitution was found to improve the stability of halide perovskites[10]. It was demonstrated that the local compressive strain by ion substitution could suppress the vacancy formation in halide perovskites[9]. Additionally, the crystalline quality of halide perovskites could be controlled by local strain via ion substitution[11]. Besides ion substitution, it was also reported the control of the local strain by light-induced lattice expansion[12]. The local strain was found to affect the optoelectronic properties of halide perovskites by creating defect distribution heterogeneity[13]. Recently, residual strain in polycrystalline halide perovskite films induced by the thermal annealing process has been reported. The residual strain in the polycrystalline methylammonium lead iodide film was found to have an impact on the perovskite stability[14]. Also, residual strain in the polycrystalline mixed halide perovskite film was reported to affect the carrier dynamics[15] and phase transition[16]. Hydrostatic pressurization was another commonly used method to apply strain to the halide perovskites. The crystal structure[17] and electronic band structure including bandgap[18] and carrier dynamics[19,20] were found to be highly subjective to the applied pressure. Metallic properties of halide perovskites were also reported under applied pressure[21].

While all of these efforts demonstrated interesting strain engineering of halide perovskites, a controllable and scalable method for strain engineering single crystal halide perovskites is still critically needed. The epitaxially strained halide perovskite demonstrated

in this study meets this need by realizing the precise control of the strain in terms of magnitude and uniformity. The chemical bonds formed at the interface, rather than the weak van der Waals interactions, not only provide strong epitaxial strain to effectively alter the material structure and properties but also endow stability against environmental fluctuations so that the strain can maintain under different temperatures and pressures, which are qualitatively different from the thermally strained and the pressurized perovskites. The magnitude of the strain can be precisely controlled by designing different lattice mismatch rather than the residual strain that shows uncertainty and uncontrollability. Enhanced optical and electrical properties have been shown in the strained halide perovskites. Therefore, this method represents a significant scientific advance compared with other reported studies to strain halide perovskites.

Supplementary Discussion 2: Characterizing $MAPbCl_xBr_{3-x}$ Substrates and Strain-free α-Formamidinium Lead Iodide (α-$FAPbI_3$)

Supplementary Fig. 1a shows the X-ray Diffraction (XRD) θ-2θ scan pattern of strain-free α-$FAPbI_3$ powder[22]. For the cubic crystal structure, the lattice parameter can be calculated by:

$$\lambda = 2d_{hkl}sin\theta$$

where λ is the incident beam wavelength, θ is the angle of incidence, and d_{hkl} is the lattice d-spacing. For strain-free α-$FAPbI_3$, the (001) peak position is at 13.92° and the corresponding lattice parameter is calculated to be 6.35 Å. All other peaks in the XRD pattern

are labeled and the corresponding lattice parameters can be calculated similarly.

Supplementary Fig. 1b shows a collection of the (001) peak locations from mixed methylammonium lead chloride/bromide ($MAPbCl_xBr_{3-x}$) single crystal substrates, which, regardless of the Cl/Br ratio, are reported to have a cubic structure[23]. The peak position shifts to a higher 2θ angle with increasing Cl ratio, indicating a decrease in the lattice parameter.

The $MAPbCl_xBr_{3-x}$ substrates are grown by solvent evaporation of different molar ratios of $MAPbCl_3$ and $MAPbBr_3$ solutions. With the lattice parameters derived from XRD measurements, the actual compositions of the substrates can be calculated by Vegard's Law[24]:

$$a_{MAPbCl_{1-x}Br_x} = (1-x)a_{MAPbCl_3} + xa_{MAPbBr_3}$$

where $a_{MAPbCl_{1-x}Br_x}$ is the lattice parameter of the mixed crystal, and a_{MAPbCl_3} and a_{MAPbBr_3} are the lattice parameters of $MAPbCl_{3.00}Br_{0.00}$ and $MAPbCl_{0.00}Br_{3.00}$ single crystals, respectively. The Cl/Br molar ratios of the precursors, the composition of the $MAPbCl_xBr_{3-x}$ crystal, and the calculated lattice parameters are summarized in Supplementary Table 1.

Supplementary Discussion 3: Strained Epitaxial Growth of α-$FAPbI_3$

Supplementary Table 2 summarizes the (001) XRD peak positions of the epitaxial α-$FAPbI_3$ on different substrates. All epitaxial samples have a shift of the (001) peak to a lower 2θ angle compared with the peak position of the strain-free crystal (13.92°), indicating an increase of the out-of-plane lattice parameter due to the in-plane compressive strain. The epitaxial α-$FAPbI_3$ on $MAPbCl_{0.00}Br_{3.00}$ substrate shows a minimum shift to 13.89°. When

more Cl is incorporated into the substrate, the lattice mismatch between α-$FAPbI_3$ and the substrate increases. The (001) XRD peak of the epitaxial α-$FAPbI_3$ will further shift to a lower 2θ angle, indicating a further increase of the out-of-plane lattice spacing and a stronger in-plane compressive strain. The strain values are calculated by comparing the in-plane lattice parameter of strain-free α-$FAPbI_3$ and epitaxial α-$FAPbI_3$, showing a tunable strain as high as -2.4%.

The epitaxial growth conditions are systematically studied (Supplementary Fig. 1c, d). $FAPbI_3$ solutions with different concentrations are deposited on the substrates at different temperatures for epitaxial growth. Since $FAPbI_3$ has an inverse solubility in the γ-Butyrolactone (GBL) solvent, high concentration and high temperature will accelerate the crystallization of α-$FAPbI_3$. In Supplementary Fig. 1c, the (001) peak position of the epitaxial α-$FAPbI_3$ is studied as a function of the growth temperature. The vertical orange line labels the peak position (13.92˚) of the strain-free α-$FAPbI_3$. The results show that growth temperatures below 180℃ always generate diffraction peaks larger than 13.92˚, while growth temperatures above 180℃ can generate peaks smaller than 13.92˚. The diffraction peak position reveals the out-of-plane lattice parameter of the epitaxial thin film. When the growth temperature is too high, crystallization of α-$FAPbI_3$ is fast and many defects are incorporated, which would relax the strain in the α-$FAPbI_3$. When the growth temperature is too low, the crystallization is too slow and Cl^-/Br^- ions may dissolve from the substrate and re-crystallize into the epitaxial α-$FAPbI_3$, forming mixed alloys at the interface, although $MAPbCl_xBr_{3-x}$ has an extremely low solubility in GBL. Diffraction peaks larger than 13.92˚ provide evidence for uniform lattice contraction caused by the incorporation of smaller Br^-

and Cl^- ions.

The epitaxial growths with different $FAPbI_3$ precursor concentrations are also investigated (Supplementary Fig. 1d). Similar to the effect of temperature, $FAPbI_3$ precursor concentrations that are too high will result in fast crystallization and a high defect concentration. Precursor concentrations that are too low will lead to slow α-$FAPbI_3$ crystallization, and thus the incorporation of Cl^-/Br^- ions that form alloys at the interface.

Supplementary Discussion 4: Quality of the Epitaxial Films

The crystalline quality of the substrate is found to have a significant impact on the quality of the epitaxial thin film since defects in the substrates will propagate through the epitaxial layer and relax the strain. The substrate crystal quality prepared using the Inverse Temperature Crystallization (ITC)[25] (Extended Data Fig. 1a) and the Slow Solvent Evaporation (SSE) methods (Extended Data Fig. 1b to 1f) are systematically characterized. The Full Width at Hall Maximum (FWHM) value in rocking curve measurements characterizes crystal mosaicity. Substrates grown by the SSE method show a much smaller FWHM value (~0.020°) compared with those by the ITC method (~0.084°) due to the extremely slow crystallization speed of SSE, indicating a higher crystal quality of substrates prepared by the SSE than those by the ITC.

Extended Data Fig. 1g shows (001) XRD patterns of epitaxial α-$FAPbI_3$ grown on substrates with high quality (red curve) and low quality (black curve). For α-$FAPbI_3$ grown on the high-quality substrate, the FWHM of the XRD peak is also smaller than α-$FAPbI_3$

150 grown on the low-quality substrate. Additionally, the epitaxial α-$FAPbI_3$ grown on the
151 high-quality substrate maintains the strained status with a shifted diffraction peak while the
152 epitaxial α-$FAPbI_3$ grown on the low-quality substrate has a (001) peak close to that of the
153 strain-free sample at 13.92˚(position of the dashed line).

154 Evidence for the strain relaxation and the growth model can also be found by studying
155 the surface topography of the epitaxial crystal. Atomic force microscopy is used to
156 characterize topographic features of a fully strained film and a fully relaxed film under the
157 tapping mode. The topography of the fully strained film (Extended Data Fig. 2a) shows a
158 smooth surface with small terrains. The stepwise height profile (Extended Data Fig. 2b)
159 corresponds to the red line in Extended Data Fig. 2a. Each step has a height of ~0.64 nm, the
160 same as the height of a strained α-$FAPbI_3$ unit cell. This reveals that the epitaxial growth of
161 α-$FAPbI_3$ follows a layer-by-layer model[26]. Besides, no obvious cracks or pits can be
162 observed, indicating a coherent growth of the epitaxial layer on the mismatched substrate.

163 The areal elastic strain energy will increase with the epitaxial layer thickness, which
164 leads to the formation of defects (e.g., dislocations) that relax the strain energy. Also, the
165 dislocations will glide and propagate to form cracks and pits at the surface of the epitaxial
166 layer. The rough surface of the fully relaxed film shows the existence of such dislocations
167 (Extended Data Fig. 2c). The corresponding height profile shows a very rough surface
168 morphology, which indicates strain relaxation (Extended Data Fig. 2d).

169 α-$FAPbI_3$ fails to epitaxially grow on substrates with a Cl ratio higher than 50% (i.e.,
170 higher Cl content than that in $MAPbCl_{1.50}Br_{1.50}$), because higher levels of lattice mismatch
171 will dramatically increase the strain energy and make the epitaxial growth less

thermodynamically favorable. Supplementary Fig. 2b shows the optical image of growth results on a $MAPbCl_{2.00}Br_{1.00}$ substrate prepared using the same method as the other substrates. In this case, the α-$FAPbI_3$ randomly crystallizes on the substrate, without forming a uniform epilayer; most of the black α-$FAPbI_3$ crystals undergo a phase transition to yellow δ-$FAPbI_3$ due to the phase instability of α-$FAPbI_3$ at room temperature.

Supplementary Discussion 5: Mechanisms of XRD Diffraction Peak Broadening

For XRD diffraction peak broadening, common reasons include[27]: 1) lattice strain, 2) crystalline dimension, 3) misorientation induced by defects, 4) thermal movement of the atoms around the equilibrium states, and 5) instrumental effects like focusing imperfection. The fourth and fifth reasons are irrelevant to this study.

We attribute the main contributions of the diffraction peak broadening in Fig. 1c to the increased lattice strain and the reduced crystalline dimension rather than the misorientation. Based on the Williamson-Hall equation[28], the diffraction peak FWHM is linearly related to the lattice strain and reversely related to the crystalline dimension[27]. In fact, such diffraction peak broadening is commonly reported in thin film heteroepitaxial growth where the thin epitaxial films usually exhibit broader diffraction peaks due to the lattice strain and low thickness[29].

In general, dislocation-induced lattice distortion and misorientation can also lead to broadening of the XRD diffraction peaks. For the strain relaxation of the epitaxial film, however, the diffraction peak broadening due to the dislocations usually leads to a huge

broadening that is several times broader than that of the free-standing materials and the fully-strained materials[30]. We investigate the FWHM of the diffraction peaks in the epitaxial α-$FAPbI_3$ thin film under different strains. Results show that the diffraction peak FWHM of the free-standing single crystals is ~0.05° while the diffraction peak FWHM of the epitaxial α-$FAPbI_3$ thin film is ~0.07°, suggesting a small broadening rather than the large broadening by the strain relaxation (Supplementary Fig. 3a).

We study the diffraction peak FWHM of the strained and the strain-relaxed α-$FAPbI_3$ thin films in Extended Data Fig. 1g. Note that in this case, we exclude the influence of the thickness-induce diffraction broadening by using films with the same thickness. Strain is relaxed by adopting a substrate with a high density of dislocations for the epitaxial growth. The XRD diffraction patterns shown in Extended Data Fig. 1g indicates that the strained epitaxial α-$FAPbI_3$ thin film shows a shift to the lower diffraction angle due to the in-plane compressive strain compared with that of the strain-relaxed epitaxial α-$FAPbI_3$ thin film. A broadening effect due to the high dislocation density of the strain-relaxed epitaxial α-$FAPbI_3$ thin film is also shown. Statistical study of the diffraction peak FWHM (Supplementary Fig. 3b) shows that the diffraction peak of the strain-relaxed α-$FAPbI_3$ is much broader (FWHM~0.25°) than that of the strained α-$FAPbI_3$ (FWHM~0.07°). Therefore, we can conclude that the broadening in the XRD diffraction peak in Fig. 1c is not due to strain relaxation.

Supplementary Discussion 6: Raman Spectroscopy and Simulation

1. Discussion of the Raman spectroscopy measurement

Full Raman spectra of the strain-free (Supplementary Fig. 4a) and the -2.4% strained (Supplementary Fig. 4b) α-$FAPbI_3$ show that there is only one peak in the region between 0 cm^{-1} and 1200 cm^{-1}, which can be attributed to the vibration of Pb-I bonds[22,31]. Note that the broad shoulder peak at ~250 cm^{-1} in the strain-free sample is attributed to the Pb-O bond from the oxidation of Pb-I bond induced by the incident laser[31]. During the fitting process, the spectra were fitted with both Pb-I and Pb-O peaks, while only the Pb-I peaks were shown in Fig. 1f.

Raman spectroscopy is also used to study the substrates (Supplementary Fig. 4e) using a 488-nm laser as the excitation source. No Raman signals can be detected from these substrates in the wavenumber range of interest. Therefore, all Raman signals in this study are originated from the epitaxial thin film.

Thickness-dependent Raman study is based on epitaxial α-$FAPbI_3$ thin films on substrates with the same composition. The results show that increasing the epitaxial thin film thickness will cause strain relaxation (Supplementary Fig. 4f). The trend is similar to the strain-dependent Raman spectra in Fig. 1e.

2. Raman spectra simulation and peak broadening

The peaks are fitted, and the peak broadening can be attributed to the emergence of a shoulder peak due to the strain-induced out-of-plane bond elongation. This phenomenon is also reported in other strain-dependent Raman studies[32-34].

To further confirm that the peak broadening in the Raman spectra originates from the strain-induced lattice deformation, we simulate the Raman spectra with first-principles calculations by the CASTEP in Materials Studios. The Raman spectra are simulated from 100 cm^{-1} to 400 cm^{-1} to compare with the experimental data.

Supplementary Fig. 4c shows the comparison between the experimental and simulated Raman spectra of the strain-free α-$FAPbI_3$ lattice. Simulated results show a Raman peak at 124 cm^{-1}, which can be assigned to the stretching of the Pb-I bond. This is correlated with the Raman peak at ~136 cm^{-1} in the experimental result. Underestimations of the simulated Raman peak wavenumbers are commonly reported[35-37]. Possible explanations may be that the anharmonicity of the bonds and the van der Waals interactions (between the inorganic cages and organic cations) can affect the simulated results[36]. Besides, the assignment of the Pb-I stretching peak also agrees with the reported studies[38,39]. Meanwhile, we also identify a weak peak at 377 cm^{-1} from the simulated Raman spectrum, which can be assigned to the bending of the FA^+ cation. However, this peak vanishes in the experimental spectrum, probably because the organic cations in halide perovskites are highly dynamic in the inorganic framework[40-42]. The reorientation of the cation will lead to the weakening of the peak under room temperature[43]. This is also the reason why low-temperature Raman, which can freeze the orientation of the organic cation, can resolve the signal from the organic cations in halide perovskites[36,43]. Note that the weak Raman band at ~250 cm^{-1} from the experimental Raman spectrum is assigned to the Pb-O bond induced by the laser oxidation[38].

We then apply -2.4% strain to the α-$FAPbI_3$ lattice and comparison between the experimental and simulated Raman spectra of the strained α-$FAPbI_3$ lattice is shown in

Supplementary Fig. 4d. An obvious peak splitting due to the in-plane Pb-I bond compression and the out-of-plane Pb-I bond stretching can be observed from the simulated Raman spectrum. This agrees with the experimental Raman peak, which shows obvious broadening due to the peak splitting. In fact, the strain-induced Raman peak splitting is also reported in other materials[32-34]. We also notice the increase of the peak intensity, which is due to the breakage of the Raman-inactive cubic symmetry[44].

Therefore, we demonstrate that the Raman peak broadening originates from the strain-induced peak splitting. Strain leads to the in-plane compression and out-of-plane stretching of the Pb-I bonds in the α-$FAPbI_3$ lattice, splitting the Pb-I stretching peak, and broadening the peak FWHM.

Supplementary Discussion 7: First-Principles Calculations of the Strained α-$FAPbI_3$

First-principles calculations allow a better understanding of the structural deformation and prediction of any emerging new properties. Cubic α-$FAPbI_3$ unit cells are calculated with the N-N axis of the FA^+ cation along (001), (101), and (111), respectively (left panel of Extended Data Fig. 3a). These three low Miller index directions represent FA's typical orientations, and their calculated total energies could reveal potential orientation preferences. As the first step, we optimized the cubic lattice parameter *a* for each orientation to obtain the lowest total energy. Our calculations show a = 6.35 Å for the FA along (001), a = 6.40 Å for the FA along (101), and a = 6.37 Å for the FA along (111). The optimized structure with the FA along (101) has the lowest total energy of -52.73 eV, and the optimized structure with the

FA along (001) shows the highest total energy of -52.68 eV. The total energy difference between these two structures is within 50 meV, and thus the structural model with FA along (101) direction was used in our calculations.

Then we applied bi-axial strains in the *ab*-plane of the optimized structure for each orientation. The range is from 3% tensile strain to -3% compressive strain. The strained cells keep their original FA orientation after optimization along the z-direction. For bandgap calculations, spin-orbit coupling (SOC) was incorporated due to the heavy element Pb, and hybrid functionals within Heyd–Scuseria–Ernzerhof (HSE) formalism with 25% Hartree–Fock (HF) exchange were employed. The calculated bandgap energy (lower right of Extended Data Fig. 3a) and cell volume (upper right of Extended Data Fig. 3a) are displayed as a function of the bi-axial strain. The cell volume decreases as the strain changes from tensile to compressive for each FA orientation. This is a result of the decreased *a* and *b* and slightly increased *c*. The bandgap decreases as well when the strain changes from tensile to compressive for each FA orientation.

Extended Data Fig. 3c shows the out-of-plane lattice deformation with different in-plane strain levels. A Poisson's ratio of around 0.3 can be calculated, consistent with the experimental value by reciprocal space mapping. Meanwhile, C-N and C=N bond lengths in FA^+ cation with different strain levels (Extended Data Fig. 3d) show no obvious changes with the strain, indicating a weak interaction between the FA^+ cation and the inorganic Pb-I framework.

Supplementary Discussion 8: Bandgap Reduction of the Strained α-$FAPbI_3$

Fig. 2a shows photoluminescence (PL) spectra of the epitaxial α-$FAPbI_3$ thin films at different strain levels. With increasing the in-plane compressive strain, a clear redshift can be seen from ~1.523 eV to ~1.488 eV. To confirm whether the redshift of PL peaks is caused by the in-plane compressive strain, several possible mechanisms are discussed.

It has been reported that as the perovskite thickness decreases, surface charges will induce depletion micro-electric field near the perovskite surface and increase the bandgap, which causes the PL to blueshift[45,46], opposite to this case here. Thus, this surface field effect can be ruled out. We also rule out the possibility of reabsorption of short-wavelength photons by the material itself, which may cause PL redshift. This effect is only observed in bulk crystals and thick films (>1 μm in thickness) and can be neglected for <100 nm films in Fig. 2a[47]. Additionally, the possible incorporation of Br or Cl element is excluded since those foreign atoms will lead to PL blueshift[48]. Hence, we can conclude that the PL redshift is due to the compressive strain generated by the lattice mismatch.

The absorption spectrum is also studied to validate the bandgap measured by PL. Note that improper measurement methods can lead to inaccurate results in both absorption and PL. For example, the absorption spectrum of thick materials obtained by the transmission mode cannot distinguish the light being absorbed or being scattered due to the large thickness of the sample[49]. Meanwhile, PL emission peaks show dependence on the illumination intensity[50] as well as material dimensions[45]. Therefore, absorption and PL measurements can be used to validate each other.

Due to the large thickness (1 to 2 mm) and the high absorption coefficients (~10^5 cm^{-1}) of the substrates, light transmittance cannot be detected[51]. Therefore, we adopt the reflection mode of UV-VIS to detect the absorption onset of the samples. The collected absorption results (Extended Data Fig. 3b) also demonstrate a red-shift when the strain goes up, which is consistent with the PL measurements.

Meanwhile, we notice that there is a quantitative discrepancy between the calculated bandgap reduction (~120 meV) and the experimental bandgap reduction (~35 meV) under -2.4% compressive strain. Note that the first-principle calculations of the strain-dependent bandgap serve as a general prediction. The main purpose is to predict the trend of the change instead of showing quantitative agreement with experimental results. Due to the approximation in the exchange-correlation functionals, deviation in the order of 10^2 meV in calculated bandgap energy from experiments is within a reasonable and tolerable range. Additionally, the geometry approximation of the strained lattice model doesn't reveal the actual deformation of the strained lattice. For example, the lattice parameters *a* and *b* are set to be different values to mimic different in-plane biaxial strain levels in the simulation, which changes the bond length between atoms. In real lattice deformation, however, the bond angle will also change to accommodate the in-plane biaxial strain (e.g., by octahedral rotation). Therefore, the calculated values can be different from the experimental values.

Supplementary Discussion 9: Emission Peaks Broadening of the Strained α-$FAPbI_3$

PL FWHM of the epitaxially strained α-$FAPbI_3$ thin film is shown to increase with the

346 strain (Supplementary Fig. 5). There are multiple possibilities origins of the PL broadening.
347 We can first rule out the influence of the domain size because the sample is a single domain
348 thin film[52]. For semiconductors, emission linewidth broadening is governed by charged
349 carrier-phonon coupling, including crystalline quality, acoustic phonon scattering, optical
350 phonon scattering, and impurity[53]. In semiconductors with heterojunctions, charged carrier
351 transfer can also take place with specific band structure at the interfaces. Such charged carrier
352 transfer usually leads to carrier quenching without direct recombination[54-56], and emission
353 peak shifting due to the energy change[57], while very few reported PL broadening due to the
354 carrier relaxation[58]. Here, we discuss the possible emission peak broadening mechanism in
355 the epitaxially strained α-$FAPbI_3$ thin films.
356
357 **1. Charge transfer**
358 The α-$FAPbI_3$ grown on $MAPbBr_3$ is analyzed as an example. α-$FAPbI_3$ has a very
359 different band structure compared with $MAPbBr_3$ in terms of bandgap, valance band
360 maximum (VBM), and conduction band minimum (CBM) as shown in Supplementary Fig. 6.
361 The heterojunction shows a straddling band alignment where the charged carrier transfer is
362 only allowed from the larger bandgap side to the smaller bandgap side when the larger
363 bandgap side is excited. During the PL measurement in this study, a 633-nm laser
364 (corresponding to 1.95 eV) was used for exciting the epitaxial layer (bandgap 1.50 eV)
365 without exciting the substrates (bandgap 2.30 eV). Upon absorption, electrons in the
366 α-$FAPbI_3$ will be excited to the conduction band while the $MAPbBr_3$ remains unexcited.

Here, the large barrier between α-$FAPbI_3$ and $MAPbBr_3$ blocks the carrier transfer from the α-$FAPbI_3$ to the $MAPbBr_3$ across the interface (Supplementary Fig. 6).

This analysis also applies to other substrates $MAPbCl_xBr_{3-x}$ in this study with different compositions from $MAPbBr_3$. When incorporating more Cl into the $MAPbBr_3$ substrate, the bandgap will further increase by lifting up the CBM and pushing down the VBM, and the energy barrier between the α-$FAPbI_3$ and the substrates will be even larger[59]. Thus, interfacial charge transport will be even less favorable.

Additionally, we also consider the carrier transfer from the $MAPbBr_3$ to the α-$FAPbI_3$. Since the $MAPbBr_3$ remains unexcited due to the large bandgap, the intrinsic electrons are extremely minor compared with the excited carrier in α-$FAPbI_3$. Therefore, we exclude the possibility of carrier transfer from the $MAPbBr_3$ to the α-$FAPbI_3$.

Considering that the laser for the PL measurement doesn't excite the carriers in the substrate, as well as the large energy barrier that blocks the interfacial carrier transfer between the epitaxial layer and the substrate, we draw the conclusion that the charged carrier transfer between the epitaxial layer and the substrates will not take place in the PL measurements and, therefore, will not contribute to the PL broadening.

2. Emission broadening by charged carrier-phonon coupling

For inorganic semiconductors, emission linewidth is associated with different mechanisms of scattering between charged carriers and phonons or impurities, which can be expressed as[60]:

$$\Gamma(T) = \Gamma_{\mathrm{imp}} + \Gamma_{\mathrm{ac}} + \Gamma_{\mathrm{LO}} + \Gamma_0$$

where $\Gamma(T)$ is the temperature-dependent emission linewidth, Γ_{imp} is the broadening terms of scattering with impurities, Γ_{ac} and Γ_{LO} are the broadening terms of the scattering from the acoustic phonons and the optical phonons, and Γ_0 is a temperature-independent broadening term associating with the scattering due to the structural disorder, respectively.

2.1 Impurity

Experimentally speaking, as mentioned above, impurity during epitaxial growth can be controlled by adopting the same growth solutions and epitaxial growth protocol. Therefore, the impurity in the epitaxial films will have a similar concentration. The influence on the PL FWHM from impurity variation will be very minimal.

Additionally, theoretical studies have identified that impurity scattering should be an inhomogeneous broadening term for PL FWHM in halide perovskites[53,61] and other semiconductors[62], which should show a weak temperature dependence. This is because impurities can lead to local electric field heterogeneity, and the existence and scattering of impurities are independent on the temperature. The PL FWHM will not change much with the temperature. However, experiments have shown a homogeneous broadening behavior of the PL FWHM of halide perovskites, with a strong temperature dependency[53,61]. Therefore, the contribution of impurity-induced emission broadening of the PL FWHM is considered to be minor in halide perovskites.

2.2 Acoustic phonon scattering

As we mentioned above, the temperature-dependent PL FWHM of halide perovskites shows a homogeneous behavior, which can be attributed to optical phonon and acoustic phonon scattering[53,61]. This is due to the fact that acoustic and optical phonons are strongly temperature-dependent. However, the contribution of the acoustic scattering Γ_{ac} in the emission broadening is also demonstrated to be minor in halide perovskites[61]. According to the expression equation of the acoustic scattering, Γ_{ac} is linearly proportional to the temperature[61]. However, the experimental temperature-dependent PL FWHM of halide perovskites, especially $FAPbI_3$, behave nonlinearly with temperature[61]. This is due to the fact that the polar Pb-I bond mainly generates optical phonons. Therefore, the contribution of the acoustic phonon scattering to the emission linewidth broadening is considered to be minor, and the optical phonon scattering is the dominating factor.

2.3 Temperature-dependent PL FWHM study

As demonstrated by extensive prior works[53,61,63,64], the above equation can be expressed in the following form, with the consideration that the acoustic phonon scattering and the impurity scattering contribute little to the emission linewidth in halide perovskites:

$$\Gamma(T) = \Gamma_{LO} + \Gamma_0 = \frac{\gamma_{LO}}{e^{(\frac{E_{LO}}{k_b T})} - 1} + \Gamma_0$$

where γ_{LO} is the charged carrier-optical phonon coupling constant, E_{LO} is the energy of the optical phonon, and k_b is the Boltzmann constant. Based on this equation, we studied the relationship between PL FWHM and the temperature for the strained and the strain-free α-$FAPbI_3$ (Extended Data Fig. 4a, b). A clear redshift can be observed while the intensity of

the emission peak increases with reducing the temperature due to the reduced scattering between the phonon and carriers at low temperatures. To better reveal the change in bandgap and FWHM as a function of the temperature, we normalize each of the PL peak intensity (Extended Data Fig. 4c, d). With decreasing the temperature, both strained and strain-free α-$FAPbI_3$ showed a bandgap narrowing, which is attributed to the contraction of the lattice. Meanwhile, the PL FWHM exhibits a uniform narrowing with decreasing the temperature. Extended Data Fig. 4e, f show the PL FWHM as a function of the temperature for a -2.4% strained and a strain-free sample, respectively.

Data were fitted with the equation introduced above. Fitted results indicate the main increment of Γ_0 in the strained sample can be attributed to the increased scattering by the crystalline quality reduction. Meanwhile, the increment of both γ_{LO} and E_{LO} suggests an enhanced charged carrier-optical phonon coupling and higher phonon energy in the strained lattice, which can be attributed to the strain-induced lattice deformation[65]. Therefore, we can conclude that the PL FWHM difference of the strained and the strain-free sample mainly comes from the increased scattering by the strain-induced crystalline quality reduction.

To sum up, we discussed several possible mechanisms that might have led to the PL peak broadening and focused on the crystalline quality and charged carrier-optical phonon coupling. By analyzing the temperature-dependent PL FWHM of both strained and strain-free α-$FAPbI_3$, the calculation results demonstrate that the PL broadening with strain is caused by the strain-induced crystalline quality reduction (major) and enhanced optical phonon scattering (minor).

Supplementary Discussion 10: Strain Relaxation of the Epitaxial α-$FAPbI_3$

Confocal PL spectroscopy is used to study the PL emission with different focal points inside a 3 μm thick -2.4% strained epitaxial α-$FAPbI_3$ (Fig. 2b). Results show a PL redshift from ~1.523 eV to ~1.479 eV with the focal point moving from the film surface to the film/substrate interface. The large discrepancy indicates the strain is relaxed in the thick α-$FAPbI_3$ film. Here, we study the possible elastic strain relaxation due to the soft nature of halide perovskite and the plastic strain relaxation from the strain-induced dislocation.

1. Elastic strain relaxation

We study the elastic relaxation of the epitaxial α-$FAPbI_3$ thin film using finite element analysis (FEA) simulations. The simulation results are shown in Supplementary Fig. 8 where an α-$FAPbI_3$ thin film with a 30 μm × 30 μm × 3 μm dimension in $l \times w \times t$. Elastic constants C_{11}, C_{12}, and C_{44} of α-$FAPbI_3$ come from the reported literature[66]. Different biaxial compressive strains (-1.2% and -2.4%) are applied at the bottom of the α-$FAPbI_3$ to simulate the interfacial strain. Plastic relaxation from the dislocations is ignored in the simulation to focus on the influence of the elastic relaxation only. Supplementary Fig. 8a, b show the planar stress distribution from the bottom view of the -1.2% and -2.4% strained α-$FAPbI_3$, respectively. Supplementary Fig. 8c, d show the vertical stress distribution from the cross-sectional view of the -1.2% and -2.4% strained α-$FAPbI_3$, respectively.

Simulated results indicate a uniform strain distribution throughout the entire epitaxial α-$FAPbI_3$ thin film. We further study the thickness-dependent stress distribution along the

vertical direction (Supplementary Fig. 8e, f), as labeled by the blue line and the red line in the Supplementary Fig. 8c, d, respectively. From the results, the strain maintains almost the same along with the thickness. For a sample thickness of 3 μm, the elastic relaxation is calculated to be 0.096% and 0.093% for -1.2% and -2.4% strained α-$FAPbI_3$, respectively. The small discrepancy between the elastic relaxation under the two strain magnitudes is due to the numerical dispersive error because the FEA simulation uses a dispersive model for approximation[67]. Therefore, the elastic relaxation in the epitaxially strained α-$FAPbI_3$ is not as prominent as we expected, due to the small thickness (in the range of hundreds of nanometers to a few micrometers) used in this study. Halide perovskites are in fact still brittle solids even though they are softer in nature than other conventional semiconductors[68].

2. Plastic strain relaxation

In heteroepitaxial growth, strain usually relaxes plastically rather than elastically. The calculations of the critical thickness where the dislocations form and relax the strain have been determined theoretically and experimentally. There are two models that have been widely used for the critical thickness calculations: the Matthews and Blakeslee (MB) model[69] and the People and Bean (PB) model[70].

The MB model is a mechanical equilibrium model that stems from the force balance of dislocations. In this model, the critical thickness is defined as the thickness when the strain force is equal to the dislocation tension force and can be expressed as:

$$h_c = \frac{b(1 - v\cos^2\alpha)}{8\pi f(1+v)\cos\lambda}\left[1 + ln(\frac{h_c}{b})\right]$$

where h_c is the critical thickness, b is the length of the Burger's vector, v is the Poisson's

ratio, α is the angle between the Burger's vector and the line vector for the dislocation, f is the misfit strain, and λ is the angle between the Burger's vector and the line in the interface plane that is perpendicular to the intersection of the glide plane with the interface.

The PB model is an alternative prediction method based on the energy equilibrium that is widely studied and experimentally proved. In this model, the critical thickness is defined as the thickness where the strain energy is equal to the dislocation formation energy and can be expressed as:

$$h_c = \frac{(1-v)b^2}{(1+v)\left(16\sqrt{2}\pi a f^2\right)} ln(\frac{h_c}{b})$$

where a is the lattice constant of the material.

Many studies show large discrepancy with the MB model. Even the epilayer is thicker than the MB limit, the dislocations are still absent[71]. Therefore, the MB model underestimates the critical thickness. The MB model may not give a quantitatively matched result. Besides, α and λ in PB need to be determined for different dislocations. However, the PB model gives a closer estimation of the critical thickness[71], and will therefore be used in this study.

We first study the thickness-dependent strain relaxation of the epitaxial α-$FAPbI_3$ thin films with different strains by in-plane XRD. In-plane XRD measures the in-plane lattice constant of the crystalline materials, which can be directly used to calculate the strain and contains information about the plastic strain relaxation in heteroepitaxy. Extended Data Fig. 5a, b show the thickness-dependent in-plane XRD patterns of two representative epitaxially strained α-$FAPbI_3$ thin films with -1.2% and -2.4% strain, respectively. The -1.2% strained epitaxial α-$FAPbI_3$ thin film with a thickness of 200 nm shows obvious plastic strain relaxation (Extended Data Fig. 5a), as evidenced by the peak shifting (to a lower angle, the

515 vertical line labels the fully strained peak position) and broadening. For the -2.4% strained
516 epitaxial α-$FAPbI_3$ thin films, plastic relaxation can be measured in films above 50 nm with
517 obvious peak shifting and broadening (Extended Data Fig. 5b). The vertical line labels the
518 fully strained peak position. Besides, we can also obtain the thickness-dependent in-plane
519 lattice constants, based on which we can calculate the in-plane strain by comparing with the
520 in-plane lattice constant. The degree of plastic strain relaxation can be quantified by
521 comparing the local in-plane strain with the highest measured in-plane strain.

522 Quantification of the degree of plastic strain relaxation is done by calculating the
523 relaxation constant R:

$$R = \frac{a_{measured} - a_{strained}}{a_{\alpha-FAPbI_3} - a_{strained}}$$

524 where $a_{measured}$ is the measured in-plane lattice constant at different thicknesses, $a_{strained}$
525 is the in-plane lattice constant with maximum strain, and $a_{\alpha-FAPbI_3}$ is the lattice constant of
526 the strain-free α-$FAPbI_3$. For the epitaxial film with the same substrate but different
527 thicknesses, R $(0 \leq R \leq 1)$ reveals the relationship between the film thickness and the
528 degree of plastic strain relaxation. For R equals to one, the epitaxial film is considered as
529 fully-relaxed. Otherwise, the film is considered as partially-relaxed. At relatively low
530 thickness, R remains at zero without any relaxation. With increasing thickness, R will
531 gradually increase due to the formation of dislocations, which plastically relax their
532 surrounding strain.

533 The thickness-dependent relaxation constants of each epitaxial α-$FAPbI_3$ with different
534 substrates (i.e., different strains) are calculated and shown in Extended Data Fig. 5c. The
535 error bars label the range of calculated R of the films with the same substrate and thickness.

Results show that the film with a -2.4% strain quickly relaxes at the thickness of ~50 nm while the film with -0.8% start to relax at ~200 nm. Note that the thinnest film we can obtain is ~50 nm and we assume that the thin layer α-$FAPbI_3$ will be fully strained without relaxation. Critical thicknesses are extracted from Extended Data Fig. 5c where R is larger than 0 and fitted with both the MB and PB models (Extended Data Fig. 5d). Results show that the critical thickness decreases with increasing the strain. Our experimental results agree more with the predicted PB model, indicating that the plastic strain relaxation due to the dislocations generated during the epitaxial growth is the dominating relaxation mechanism.

Confocal PL spectroscopy is used to study the PL emission with different focal points inside a 3 μm thick -2.4% strained epitaxial α-$FAPbI_3$ (Fig. 2b). Results show a PL redshift from ~1.523 eV to ~1.479 eV with the focal point moving from the film surface to the film/substrate interface. Besides, we also measured a strain-free bulk α-$FAPbI_3$ crystal sample and a 3 μm thick mixed sample (Supplementary Fig. 7). Note that the mixed sample came from the mixed epitaxial growth with low temperature and low concentration in Supplementary Fig. 1. By using a low growth temperature and low concentration solution, the crystallization speed of the epitaxial film will be significantly retarded. The long-time contact of the substrate and solution will lead to a slow ion exchange between them and, therefore, form an epitaxial film containing mixed Cl and Br. In the case of Fig. 2a, we adopt an optimal growth condition with high temperature (180 °C) and high concentration (1.2 mol L^{-1}) to achieve a fast crystallization speed, so that the α-$FAPbI_3$ crystals will nucleate on the substrate, even before the Cl and Br ions dissolve and get mixed in the solution. The obtained interface will be clear and the epitaxial α-$FAPbI_3$ sample will be highly strained. The

strain-free sample shows a much less obvious PL peak redshift from ~1.523 eV to ~1.516 eV (Supplementary Fig. 7a), which can be attributed to reabsorption as discussed above. For the mixed sample grown under low temperature and low concentration (Supplementary Fig. 7b), the PL peak at the sample surface is at ~1.542 eV, indicating incorporation of Cl and Br elements from the substrate. With increasing focal depth to the film/substrate interface, the PL peak blueshifts to below 1.550 eV, which indicates a higher degree of mixing.

Film thickness-dependent PL measurements are based on samples at -2.4% strain with different epitaxial film thicknesses (Supplementary Fig. 9). A 633-nm laser with the standard mode is used as the excitation source to study the overall emission behavior of the film at all depths. The PL peak position shows a strong film thickness dependency. When the α-$FAPbI_3$ film thickness increases, the PL emission peak shifted from ~1.479 eV back to 1.523 eV, the same as that of the strain-free α-$FAPbI_3$, which indicates the strain has been fully relaxed.

Supplementary Discussion 11: Temperature-Dependent Bandgap of the Strained α-$FAPbI_3$

Due to the soft nature, external stimuli (i.e., temperature, pressure) can effectively alter the lattice structure of halide perovskites, and, therefore, change the electronic band structures[18,20,72]. Under such considerations, temperature-dependent PL was studied on both epitaxial α-$FAPbI_3$ and free-standing α-$FAPbI_3$. Epitaxially grown thin films are subjected to the lattice deformation of the substrates due to the strong chemical bonds at the interface and the much bulkier size of the substrate. In this case, the epitaxial film will adopt a similar

thermal expansion coefficient α_t to that of the substrate[73]. A reported study has shown that the α_t of halide perovskites are subjected to the molecular radius of halides. Therefore, the I-based perovskite epitaxial layer will have a larger α_t due to the large radius of I^- than the Br^- and Cl^- based halide perovskite substrate[74]. The epitaxial α-$FAPbI_3$ on a Br^- and Cl^- based substrate exhibited a reduced temperature dependency compared with the freestanding α-$FAPbI_3$. Additionally, if the substrate has a larger α_t than that of the strained layer, we should expect to see the strained sample has a stronger temperature dependence than that of the free-standing sample.

Supplementary Discussion 12: Band Structure of the Strained α-$FAPbI_3$

UPS measurements are carried out on epitaxial α-$FAPbI_3$ films with different strain levels. Extended Data Fig. 6a shows the cutoff energy region and Extended Data Fig. 6b shows the valence band region of the α-$FAPbI_3$. Take the UPS spectrum of the strain-free α-$FAPbI_3$ as an example, the position of the electron affinity (Fermi level) *versus* vacuum is the difference between the high binding energy cutoff and the radiation energy of He I (21.22 eV):

$$16.09\ \text{eV} - 21.22\ \text{eV} = -5.13\ \text{eV}$$

The low binding energy cutoff (0.62 eV) determines the position of Valence Band Maximum (VBM). Therefore, the position of the VBM relative to the vacuum level is:

$$-5.13\ \text{eV} - 0.62\ \text{eV} = -5.75\ \text{eV}$$

Considering the measured optical bandgap of ~1.51 eV (Fig. 2a), the Conduction Band

602 Minimum (CBM) is determined to be -4.24 eV. This also suggests that the Fermi level is
603 closer to the VBM than to the CBM, and therefore the strain-free α-$FAPbI_3$ is p-type.
604 Similarly, all other strained epitaxial thin films show a p-type character.

605 Additionally, the results show that the valence band is pushed up by 50 meV while the
606 CBM is only pushed up by 15 meV when strain increases from 0% to -2.4%. The reason why
607 VBM is pushed up more than the CBM by the biaxial in-plane compressive strain is because
608 the compressed PbI_6 octahedron contributes more to the VBM than the CBM. The VBM is
609 composed of the coupled Pb 6*s* and I 5*p* orbitals that form the PbI_6 octahedral, while the
610 CBM is mostly nonbonding localized states of Pb *p* orbitals[75].

611

612

613 **Supplementary Discussion 13: Effective Mass Calculations and Carrier Mobility**
614 **Characterizations of the Strained α-$FAPbI_3$**

615 **1. Effective mass calculations**

616 To investigate the effect of strain on carrier dynamics in α-$FAPbI_3$, we analyzed the
617 variation of charged carrier mobility via predicting effective masses of charged carriers from
618 first-principles calculations. In the calculations, the mean free time of carriers was assumed to
619 be a constant, and the reversely proportional relationship between the effective mass and
620 charged carrier mobility was used. Carrier effective masses are determined by the curvature
621 of the highest energy at the VBM for holes and lowest energy at the CBM for electrons in the
622 *k* space. Figure 3a shows the calculated electron and hole effective masses of α-$FAPbI_3$ under
623 different strain levels. Electronic band structures of α-$FAPbI_3$ under 3%, 0%, and -3% are

also shown in the lower panels of Fig. 3a. Results indicate that the hole effective mass m_h^* decreases when strain goes from tensile to compressive, while the electron effective mass m_e^* barely changes with the strain. The trend of m_h^* can be revealed from the curvature of the highest energy point of the VBM, which gets less dispersive with increasing compressive strain. This is due to the fact that the VBM that determines m_h^* mainly consists of Pb 6*s* and I 5*p* orbitals. Under tensile strain, the distance between Pb and I atoms increase and therefore the Pb-I bond interaction is weakened, thus leading to the increase of effective mass. In contrast, the hole mobility will increase under compressive strain due to the enhanced Pb-I bond interaction and the decreased effective mass. However, the CBM that determines the electron effective mass mainly consist of Pb *p* orbitals is less sensitive to the deformation of Pb-I bonds, which is why m_e^* barely changes with applied strain[15].

2. Interfacial carrier transfer and Hall effect measurements

Hall effect is used to measure the strain-dependent carrier mobility of the epitaxial α-$FAPbI_3$ thin films. Before the measurement, we study the possible carrier collection from the substrates since the substrates are halide perovskites with high carrier mobility as well. We first analyze the device structure with the FEA simulation. The schematic device structure is shown in Supplementary Fig. 10a where four Au electrodes are deposited with a layer of Parylene-C beneath. The Parylene-C serves as the insulating layer to prevent the carrier collection from the substrate to the electrodes. To better understand the carrier transfer between the epitaxial layer and the substrate, we also study the band alignment between them (Supplementary Fig. 10b). Herein, α-$FAPbI_3$ and $MAPbBr_3$ are analyzed as an example.

646 α-$FAPbI_3$ has a very different band structure compared with $MAPbBr_3$ in terms of bandgap,
647 valance band maximum (VBM) as well as conduction band minimum (CBM). For α-$FAPbI_3$,
648 VBM and CBM are determined to be -5.75 eV and -4.25 eV by the ultraviolet photoelectron
649 spectroscopy, respectively. For $MAPbBr_3$, VBM and CBM are determined to be -6.20 eV and
650 -3.90 eV from the literature[76]. For the Hall measurement, the injected carriers are subject to
651 the Lorentz force applied by the vertical magnetic field and are accumulated at the diagonal
652 electrodes to build up the Hall voltage. However, the large energy barrier at the
653 heterojunction interface blocks the carrier injection from the α-$FAPbI_3$ to the $MAPbBr_3$.
654 Therefore, there is a very low concentration of free carriers in the substrate that can hardly
655 generate a significant Hall voltage during the measurement. This analysis also applies to
656 other substrates $MAPbCl_xBr_{3-x}$ in this study with different compositions from $MAPbBr_3$.
657 When incorporating more Cl into the $MAPbBr_3$ substrate, the bandgap will further increase
658 by lifting up the CBM and pushing down the VBM, and the energy barrier between the
659 α-$FAPbI_3$ and the substrates will be even larger[59]. Thus, interfacial charge transport will be
660 even less favorable. Additionally, we also exclude the free carrier transfer from the $MAPbBr_3$
661 to the α-$FAPbI_3$.

662 We then simulate the current distribution within the device by FEA. We also intend to
663 quantify the current density in both the epitaxial layer and the substrate to study the
664 contribution of the substrate to the Hall measurement. With the combined energy diagram
665 and the electric field distribution, we simulate the current distribution in the device
666 (Supplementary Fig. 10c upper panel). The simulation results show that the current
667 distribution is completely different from the electric field distribution. Current density in the

668 epitaxial layer (9.8 A m^{-2}) is much higher than that of the substrate (0.4 A m^{-2}), which means
669 that the large energy barrier between the epitaxial layer and the substrate, as well as the
670 minimal vertical electric field distribution and the insulation of the Parylene-C, minimizes the
671 carrier injection to the substrate. A closer look at the area that is close to the electrode
672 suggests that the carrier injection to the substrate is indeed prohibited (Supplementary Fig.
673 10c lower panel, red arrows indicate the direction of the current flow). To quantify the ratio
674 of the current in the substrate to that in the epitaxial layer, we study the current density along
675 the vertical orange line where the current flows horizontally (at a steady state).
676 Supplementary Fig. 10d shows the vertical current density distribution along the vertical
677 orange line where the heterostructural interface locates at 500 nm from the bottom (0 nm).
678 The ratio of current density across the interface is shown to ~ 24.5:1 where the epitaxial layer
679 is 9.8 A m^{-2} and the substrate is 0.4 A m^{-2}. By integrating the area below the current
680 distribution curve, we obtain the ratio of the current density in the substrate to the total
681 current density along the vertical line to be 0.8%. Therefore, we conclude that the carrier in
682 the substrate is negligible compared with that in the epitaxial layer, and we attribute this
683 result to the large energy barrier between the epitaxial layer and the substrate, as well as the
684 minimal vertical electrical field distribution and the insulation of the Parylene-C layer.
685 Without the concern of possible carrier collection from the substrates, we perform Hall
686 effect measurement to the epitaxial α-$FAPbI_3$ thin films under different strains. Measurement
687 results also show p-type character, which is consistent with the UPS results. The hole
688 mobility as a function of strain is plotted in Fig. 3b, which doesn't show a linear tendency
689 with increasing strain. Devices with -0.8%, -1.2%, and -1.4% strain show enhanced hole

mobility compared with that of the strain-free α-$FAPbI_3$ bulk crystal. A -1.2% strained device gives the highest mobility of ~72 $cm^2 V^{-1} s^{-1}$. Further increasing the strain results in a drastic drop in the hole mobility, because higher strain levels will relax at a lower thickness and induce high concentrations of dislocations that deteriorate the device performance.

3. Time-of-flight (ToF) measurements

To validate the results from the Hall effect measurement, we study the carrier mobility of the epitaxial α-$FAPbI_3$ thin films under different strains by ToF measurements. The schematic device structure is shown in the inset of Fig. 3d. A layer of Parylene-C was deposited between the Au electrode and the substrate to block the carrier extracted from the substrate as demonstrated above. Besides, we adopted a 685-nm laser as the excitation source so that the photon can only be absorbed by the epitaxial layer rather than the substrate that has a larger bandgap than the excitation laser energy. In this case, we guaranteed the measured photovoltages coming from the epitaxial layer absorption were the same. Similarly, the excited electrons that occupy the CBM of the α-$FAPbI_3$ are less likely to be extracted to the CBM of the substrate due to the large energy barrier, as shown in Supplementary Fig. 10.

ToF measurements were carried out with the designed structure where the distance between the two electrodes is controlled to be 100 μm in lateral directions. Meanwhile, the thickness of the epitaxial layer is controlled to be the same and all the devices are biased with 1 V. The measured transient photocurrents are shown in Fig. 3c where the carrier transit time can be extracted as the inflection point of the photocurrent curve. The carrier mobility can be calculated by:

$$\mu = \frac{d^2}{Vt}$$

where μ is the calculated carrier mobility, d is the thickness of the target region, V is the applied voltage, and t is the measured carrier transit time. The measured carrier mobilities are plotted in Fig. 3d. Our measured ToF mobility of the epitaxial α-$FAPbI_3$ with different strains showed a similar trend compared with the measured Hall mobility. -1.2% strained α-$FAPbI_3$ exhibits the highest carrier mobility while further increasing the strain can lead to faster relaxation, and the accumulation of dislocations will reduce the carrier mobility.

Besides, bias and laser power dependence of the ToF measurement are also discussed. ToF mobility is calculated by $\mu = \frac{d^2}{Vt}$. The applied bias will only change the carrier transient time rather than the carrier mobility. This is because the carrier mobility is an intrinsic property of the semiconductor materials and is independent of the magnitude of the applied bias. This rule has been demonstrated by many ToF measurements of halide perovskites, in which the carrier mobility is independent of the applied bias but the measured carrier transient time is inversely proportional to the applied bias[77,78]. In the measurements, as described in the manuscript, all experiments are tested under 1 V DC bias with other experimental parameters well-controlled. Therefore, the transient photocurrents of the epitaxial films under different strain magnitudes appropriately reveal the carrier mobility of the epitaxial thin films. For the ToF measurement, it has been reported that the photogenerated carrier density shows laser power dependency and a high carrier density can generate the space charge effect which affects carrier extraction[79,80]. However, the space charge effect will be significant only in systems where the ratio between the electron mobility and the hole mobility excesses two orders of magnitude[81]. According to the reported carrier

mobility of halide perovskites, the electron and hole mobilities are usually on the same order of magnitude when they are from the same literature[82]. Therefore, the space charge effect can be safely ignored and the laser power dependence of ToF measurements is less significant in this study. In the measurements, the laser intensity is kept at constant (10 mW cm^{-2}) throughout the entire measurement so that the only variation is the strain magnitude of the epitaxial thin film.

The possible influence of the current–voltage (*I–V)* hysteresis on the ToF measurement is also discussed here. During the ToF measurement, the devices are biased under a constant voltage, e.g., 1 V, to collect photogenerated carriers in the epitaxial thin films. In this case, the baseline current due to ion migration and mobile electron and hole carriers under a fixed electric field is considered to be in a steady state. Adding on top of the baseline current, a pulsed laser is used as the excitation source to generate carriers in the epitaxial thin film. The corresponding photocurrent-time characteristics are recorded by an oscilloscope. The timescale of the excited transient current, i.e., ToF, is measured to be ~10^{-6} s (as seen in Fig. 3 in the main text). *I–V* hysteresis is reported to originate from ion migration, device capacitive charging, and perovskite ferroelectric polarization[83,84]. For the ion migration, the timescale is reported to be in the range of seconds to minutes in halide perovskites[85], which is much longer than that of the ToF. For the device capacitive charging, whose timescale is reported to be in the range of milliseconds to seconds[83], which is also much longer than that of the ToF. Also, the timescale of ferroelectric dipole switching is reported to be faster than 10^{-8} s [86], which is much shorter than that of the ToF. Besides, since the devices are biased under 1 V DC voltage during the measurement, the capacitive charge and the ferroelectric

755 dipoles are almost kept constant in the devices. Therefore, it is safe to exclude the possible
756 influence of the *I–V* hysteresis on the ToF measurement.
757
758 **4. Analysis of the influence of ion migrations to the carrier mobility measurements**
759 Ion migrations of halide perovskites have been studied in the literature and are believed
760 to be the origin of the reported current-voltage hysteresis in halide perovskites. Reported
761 studies showed that the mobility of the vacancies and the ions in polycrystalline perovskites
762 were determined to be ~1.6×10^{-6} cm^2 V^{-1} s^{-1} and ~5×10^{-8} cm^2 V^{-1} s^{-1}, respectively[87,88].
763 However, these values are much smaller than that of the measured hole mobilities (~50 cm^2
764 V^{-1} s^{-1}) in this study. Additionally, the carrier transit time in the ToF measurement of this
765 study was in the range of μs, which was too short for the ions to move a substantial distance.
766 Therefore, it is safe to exclude the contribution of ions and structural vacancies from the
767 measured hole mobility in this study.
768 Besides, grain boundaries of the polycrystalline halide perovskites were reported to be a
769 major pathway for ion migrations[89-91]. In this study, the epitaxial growth of single-crystalline
770 perovskites minimizes the formation of grain boundaries and, therefore, minimizes the
771 influence of the ion migrations. In a reported study, the ion migration mobility in both
772 polycrystalline and single crystalline methylammonium lead iodide ($MAPbI_3$) were
773 measured[92]. Compared with the ion migration in polycrystalline $MAPbI_3$ whose ion migration
774 mobility was ~1×10^{-9} cm^2 V^{-1} s^{-1}, the ion migration in single crystalline $MAPbI_3$ can hardly be
775 detected[92]. Therefore, we can conclude that the influence of ionic movements in the halide
776 perovskites can be excluded from this study.

5. Crystalline quality characterization

The space-charge limit current (SCLC) method is used to quantitatively evaluate the crystalline quality of the epitaxial thin film (Extended Data Fig. 7 and Supplementary Fig. 11). Devices adopt the same structure as the one used in ToF measurement. Devices with different strain levels (strain-free, -0.8%, -1.4%, and -2.4%) are fabricated and tested. Note that bulk α-$FAPbI_3$ single crystals were used as the substrates to fabricate strain-free devices.

We first study the *I–V* characteristic curves of the devices with forward and reverse scans from 0.01 V to 2 V (Extended Data Fig. 7a to 7d). Note that the devices adopt a planar structure to correlate with the devices used in the Hall effect measurements. A layer of Parylene-C (50 nm) and a layer of Au (50 nm) are sequentially deposited on the substrates while the lateral distance between two Parylene-C/Au electrodes is 100 μm. Epitaxially strained α-$FAPbI_3$ thin films are then grown from the gaps between the electrodes and cover part of the electrodes for electrical contact.

In the forward scan, the log-log *I–V* characteristic curves show different regions of behavior. At low voltages, the *I–V* curves exhibit a typical ohmic conduction behavior, where the current is linearly related to the applied voltage (n~1, blue line). In this region, the quantity of the thermally generated free carriers exceeds that of the externally injected carriers[93]. With increasing the applied voltage, the externally injected carriers gradually increase and start to fill the traps. Therefore, a trap-filling process is identified by the end of the linear ohmic region (n>3, green). By further increasing the voltage, traps in the bandgap are completely filled by the externally injected carriers and the carriers move freely[94]. In this

799 region, the current is squarely related to the applied voltage (n~2, orange). V_{TFL} is extracted
800 by finding the voltage where the ohmic region ends. The extracted V_{TFL} in samples with
801 different strains is used to evaluate the trap density, which agrees with the results in the
802 manuscript.

803 The forward scan is followed by a reverse scan where the *I–V* characteristic curves of
804 the reverse scan show only a linear region. By fitting the *I–V* curves of the reverse scan, we
805 find out that the current is squarely related to the applied voltage (n~2, red). During the
806 reverse scan, the filled traps will not undergo a de-trapping process because of the existence
807 of the applied electric field as well as the continuously injected carriers. Therefore, the
808 reverse scan cannot be used to study the trap-filling process, and the evaluation of the V_{TFL}
809 can only be studied with the forward scan. Trap density of the epitaxial film n_t can be
810 calculated by:

$$V_{TFL} = {en_t d^2}\Big/{2\varepsilon\varepsilon_0}$$

811 where d is the layer thickness, ε (=47) is the relative dielectric constant of α-$FAPbI_3$, and
812 ε_0 is the vacuum permittivity.

813 We also statistically study the trap density in the epitaxial α-$FAPbI_3$ film with different
814 strain magnitudes to evaluate the robustness of the measured trap density values. Here, five
815 different devices of each strain value are tested. The trap density of the epitaxial α-$FAPbI_3$
816 film from different samples are calculated and displayed in Supplementary Fig. 11a. The
817 average trap densities and the standard deviation are shown in Supplementary Fig. 11b. With
818 increasing the strain, the average trap densities show an increasing trend, indicating that a
819 higher strain level induces a higher defect density in the epitaxial α-$FAPbI_3$ film. This trend

820 correlates well with the data we showed in the manuscript. Meanwhile, the standard deviation
821 of the trap density also increases with the strain, which reveals an increased disorder in the
822 epitaxial α-$FAPbI_3$ film at higher strain values.

823 Besides, we also investigate *I–V* characteristic curves from the same device under
824 different measurement conditions, e.g., different scan rates and scan directions. *I–V* curves of
825 the halide perovskites are reported to be scan rate-dependent due to the fact that the scan rate
826 can alter the charged carrier collection efficiency of the devices, which results in artificial *I–V*
827 curves[84,85,95]. However, this discrepancy can be effectively minimized by adopting a
828 relatively slow scan rate[83] since a fast scan rate has been reported to go beyond the response
829 speed of free carriers to the electric field[96]. To prove that the 50 mV s^{-1} scan rate we use in
830 this work does not produce artificial *I–V* curves, we study *I–V* curves under four representative
831 scan rates (Supplementary Fig. 11c). *I–V* curves with 10 mV s^{-1}, 50 mV s^{-1}, and 200 mV s^{-1}
832 scan rates show distinct trap filling behavior as we discussed above. The V_{TFL} extracted from
833 the *I–V* curves with 10 mV s^{-1} and 50 mV s^{-1} scan rates are similar, indicating that 10 mV s^{-1}
834 and 50 mV s^{-1} are sufficiently slow to avoid artificial *I–V* curves and V_{TFL} values. Meanwhile,
835 increasing the scan rate to 200 mV s^{-1} leads to a smaller V_{TFL} because of the limited response
836 of free carriers to the rapid electric field change. No trap filling process can even be measured
837 when further increasing the scan rate to 1000 mV s^{-1}, showing that the *I–V* curve under a very
838 fast scan rate can skew the results. Therefore, we can conclude that the 50 mV s^{-1} scan rate
839 we use in the SCLC measurements helps produce reliable *I–V* curves and V_{TFL}. Besides, we
840 study how the scan direction may possibly affect the SCLC measurement. Supplementary Fig.
841 11d shows *I–V* curves of the same device with different scan directions. The *I–V* curves from

positive and negative scan directions, with ~10 min in between the scans, are similar to each other, which is because the device adopts a symmetric Au/perovskite/Au structure. The initial direction of the forward scan along either direction should give the same result. Therefore, we can conclude that the SCLC measurements under different scan conditions, with a slow scan rate (50 mV s^{-1}), and a symmetric device structure can produce reliable results.

In this study, the goal is not to distinguish the origins or the densities of various traps but is to study the trap density increment in the epitaxial α-$FAPbI_3$ thin films when the strain magnitude is increased. For lattice-mismatched heteroepitaxial growth, the density of misfit dislocations will be increased with increasing the interfacial misfit magnitude and the epitaxial layer thickness, to partially release the strain[97]. These misfit dislocations tend to degrade the properties of the epitaxial layers and, therefore, the performance of the devices by introducing below-gap trap states. For the impurity, the growth precursor was controlled to be the same, which will keep a similar impurity source for all α-$FAPbI_3$ films in this study. Without additional impurity source being introduced during epitaxial growth, the epitaxial film with different strain levels should share a similar impurity density. Therefore, we exclude the contribution of impurities to the measured trap density increment. For the other crystallographic defects (e.g., vacancies, interstitials, antisites, etc.), their contributions to the trap density increment are considered to be minor, because it is a convention that the generation of dislocations is the main reason for strain relaxation in heteroepitaxy[97,98]. For the interfacial defects formed at the perovskite/electrode interface, all devices fabrication adopted the same protocol. Therefore, the interfacial traps caused by the interfacial defects are similar for different strain values and can be excluded from the possible reason for the trap density

increment in the epitaxial samples. In this case, the impurities and the interfacial defects will not lead to the significant trap density increment, up to ~1000% as observed in the studies with increasing the strain magnitude from 0% to -2.4%.

Based on the above discussions, we demonstrate that the trap density increments with increasing the interfacial misfit magnitude and film thickness can be attributed to the strain-induced dislocations. Even though there is currently a lack of an experimental characterization technique that would allow accurately quantifying the separate contribution of each defect due to the complexity of these defects[99], contributions from all other types of traps are minor and can be safely excluded in this study by adopting the unique variable principle throughout the experiment. Actually, the unique variable principal is commonly used to exclude irrelevant factors in trap density measurements, as evidenced by many examples in the literature. Vapor deposition of relatively thick perovskite film is reported to show reduced trap density due to the reduced crystallographic defects. The trap density increment in the relatively thinner sample excludes the contribution of impurities and the interfacial defects because they are considered to be similar to those of the thicker sample and will not lead to trap density reduction[100]. Also, it is recently reported that the addition of CuBr into inorganic perovskite will reduce the trap density. The influence of the interfacial defects and the impurities are considered of minor influence to the trap density reduction in the control sample due to the same fabrication protocol[101]. Similarly, the addition of Eu^{3+}-Eu^{2+} ionic pair can reduce the crystallographic defects generated by the Pb^0 and I^0. The trap density increment in the control sample rules out the contribution of interfacial defects and impurities because the samples share similar fabrication processes[102]. Additionally,

perovskite seeding growth is reported to improve the crystallinity and reduce the trap density. The interfacial defects and the impurities in the control sample are considered to be similar in the seeded grown sample and control sample[103]. What's more, modifying the interface between the perovskite and the electron transporting layer is shown to reduce interfacial defects and trap density. The influence of the impurities and crystallographic defects can be excluded because they are considered to be similar in different devices[104]. Finally, incorporating bilateral alkylamine additives is shown to reduce interfacial defects and trap density in the perovskite film. Contributions from impurities and crystallographic defects are ruled out due to the fact these two factors are similar in different devices[105].

We also investigate the literature to study the minimum trap density difference that can be measured by the SCLC method. Researchers demonstrated the reduced trap density by 15% due to the incorporation of Cl in the perovskite film[100]. In two-dimensional perovskite nanowires with different layer numbers, a one-fold increment of trap density was also reported[106]. Meanwhile, researchers demonstrated the decrease of trap density by ~20% with a modified tin doped indium oxide (ITO) surface[107]. Similarly, a decrease of trap density by ~50% with a modified interface was also reported[108]. Compared with the reported works, the results in this study demonstrate a difference from ~30% to up to ~1000%, which is sufficiently large to conclude that a higher strain can induce more defects.

Characterizing the trap density in halide perovskite thin films has been widely studied. Quantitative characterization of the trap density in halide perovskites are mostly done by the SCLC method (the dark *I–V* characteristic curve). It is believed to be the most facile, accurate, and direct technique for trap density characterization and has been extensively used[77,78,109].

908 Besides the SCLC method, tuning the excitation density of input photons in the transient
909 photocurrent measurement is also reported to roughly estimate the trap density by generating
910 different densities of free carriers and monitoring the decay rate[110,111]. The measurement
911 accuracy is relatively low. Additionally, capacitance-frequency (*C*-ω) spectroscopy has been
912 reported to study the trap density in organic materials[112,113] and halide perovskites[114-117]. The
913 low-frequency capacitance originates from the carrier trapping/detrapping of electronic traps
914 while the high-frequency capacitance is attributed to the geometrical capacitance and the
915 depletion capacitance[114,116].

916 In this study, we use the *C*-ω spectroscopy as an alternative probe for trap density of
917 epitaxial α-$FAPbI_3$ thin films with different strain magnitudes. Devices for *C*-ω
918 measurements have a lateral configuration with a 3 mm width. Au and ITO are used as the
919 two electrodes with a 2×2 mm^2 area. During the measurement, a 0.5 V AC voltage is applied.
920 The resulting electric field is 1.67×10^{-4} V μm^{-1}, which is insufficient for generating ion
921 migration[117]. In this case, we exclude the contribution of charged ions to the measured
922 capacitance. The capacitance of α-$FAPbI_3$ thin films with different strain magnitudes are
923 measured in the frequency range of 1~10^5 Hz in dark. To eliminate the influence of the
924 parasitic capacitance from the substrate and air, we first measure the *C*-ω spectra of the bare
925 substrate without the epitaxial layer. After measuring the *C*-ω spectra of the devices with the
926 epitaxial layer, we subtract the spectra of the substrates from that of the devices to obtain the
927 *C*-ω spectra of the epitaxial layer, which therefore exclude the capacitance contributions from
928 the substrates and air. The results after subtraction are shown in Supplementary Fig. 12a. The
929 measured capacitance gradually increases with increasing the strain magnitudes, indicating

the accumulation of electronic traps. We then calculate the trap density with the *C-ω* measurement results. The trap density can be calculated by

$$N_t(E_\omega) = -\frac{V_b}{qkAtT}\frac{d\,C(\omega)}{d\ln(\omega)}$$

where N_t is the trap density at a certain trap energy E_ω, V_b is the build-in potential and is estimated to be ~0.5 V from the work function difference between Au and ITO, q is the element charge, k is the Boltzmann constant, A is the device area, t is the thickness, and T is the temperature. Trap energy E_ω is calculated by

$$E_\omega = kT\ln(\frac{\omega_0}{\omega})$$

where ω_0 is the attempt-to-escape frequency, which is reported to be ~2×10^{11} s^{-1} for halide perovskites[118]. The calculated trap density of the epitaxial α-$FAPbI_3$ thin films with different strain magnitudes are shown in Supplementary Fig. 12b and an obvious trap density increment can be seen with increasing strain magnitudes.

To quantitatively evaluate the trap density in the epitaxial thin films, we fit the calculated trap density distribution with the following Gaussian distribution equation:

$$N_t(E_\omega) = \frac{n_t}{\sigma\sqrt{2\pi}}exp\left[-\frac{(E_0 - E_\omega)^2}{2\sigma^2}\right]$$

where n_t is the trap density, σ is the disorder parameter, and E_0 is the mean energy of the traps. The fitted trap density (n_t) for 0%, -0.8%, -1.4%, and -2.4% strained epitaxial thin films are 2.6×10^{11} cm^{-3}, 3.2×10^{11} cm^{-3}, 7.2×10^{11} cm^{-3}, and 2.4×10^{12} cm^{-3}, respectively. The trap density increment with increasing the strain magnitude indicates an accumulation of dislocations under a higher strain magnitude[97]. The trend also agrees with that measured by the SCLC method (Extended Data Fig. 7 and Supplementary Fig. 11). Note that the *C-ω* method measures the sum of electron and hole traps[112] while the SCLC methods can

distinguish electron and hole traps with selected electrodes[78]. In the SCLC measurements, we adopt an Au/perovskite/Au structure that only reveals the hole traps due to the energy alignment of the Au electrode for hole injection[78]. This may be the main reason that leads to the small discrepancy in the results measured by the *C-ω* and the SCLC methods.

Supplementary Discussion 14: Different Methods for Stabilizing α-$FAPbI_3$

1. Current methods

The high-temperature α-$FAPbI_3$ phase suffers from a spontaneous and quick phase transition to the low-temperature, photoinactive δ-$FAPbI_3$ phase at room temperature. The most popular stabilization method for α-$FAPbI_3$ is accomplished by mixing/doping small ions[119-121]. Several reported works discussed the possible stabilization mechanisms behind. Researchers explained the stabilization effect of mixing small ions by studying the entropy where the formation energy of the mixed δ phase was too large for the phase transition to take place[119]. Meanwhile, the internal strain of α-$FAPbI_3$ lattice was reported as the driving force of the phase transition and compensation of the strain by incorporating small ions could prevent the phase transition[10]. Despite the success and reliability of this method, it should be pointed out that the incorporation of the small ions usually leads to an enlarged bandgap[119]. As a result, light absorption at the long-wavelength region will be inhibited and the short-circuit current of the fabricated solar cells will decrease[122]. Recently, researchers reported several mixing strategies that stabilized the phase without the bandgap increment[122,123]. However, such incorporation showed short-term stability of no more than

several weeks. Meanwhile, the incorporation of external ions that were not well-miscible with the α-$FAPbI_3$ matrix would eventually lead to disorders and heterogeneity in the lattice, and these heterogeneities would serve as non-radiative recombination centers that deteriorated the device performance[51].

Other stabilization methods of α-$FAPbI_3$ were also reported. Surface functionalization and dimension reduction are popular due to the recent emergence of low-dimensional halide perovskites. The reduction of surface energy was accomplished by large-sized/nonconductive organic molecules[124]. However, such functionalization with organic molecules would prohibit the transport of charged carriers and, therefore, led to relatively low performance. Recently, a new confinement strategy of α-$FAPbI_3$ stabilization was reported. α-$FAPbI_3$ was found to obtain phase stability within patterned nanochannels[125]. Long-term stability was achieved by limiting the expansion of α-$FAPbI_3$ during phase transition to δ-$FAPbI_3$ with the confinement of the surrounding nanochannels. However, this method lacked compatibility with conventional fabrication protocols and could hardly be applied to device integration. Additionally, encapsulating the α-$FAPbI_3$ with mesoporous TiO_2 scaffolds was found to enhance the phase stability of α-$FAPbI_3$[126]. However, the stability didn't last long.

2. Differences between the epitaxial stabilization and the current methods.

Besides the conventional stabilization by forming mixed perovskite alloys, the dimensional reduction, as well as the encapsulation effects, are also reported[124,125,127,128]. Herein, we discuss the differences between these methods with the epitaxial stabilization in

this study and demonstrate that the epitaxial stabilization is from neither the dimensional reduction nor the encapsulation effect.

The dimensional reduction of the α-$FAPbI_3$ is usually accomplished by forming two-dimensional α-$FAPbI_3$ with several atomic layers or zero-dimensional quantum dot with a limited number of lattices[124]. This low-dimensional α-$FAPbI_3$ is usually capped with surfactants/capping agents to reduce the surface energy so that the metastable α phase can be stabilized. In the case of the epitaxially stabilized α-$FAPbI_3$, however, the thin film is far beyond several atomic layers and, therefore, will not be considered as the effect of the dimensional reduction.

The encapsulation effect is also reported to stabilize the α-$FAPbI_3$. Embedding the α-$FAPbI_3$ into the mesoporous TiO_2 scaffolds was reported to retard the phase transition due to the partial encapsulation by the mesoporous TiO_2 [126]. Meanwhile, the stabilization of α-$FAPbI_3$ within nanochannel was also reported[125,128]. The encapsulation of the α-$FAPbI_3$ with the nanochannels prohibits the phase transition by constraining the volume expansion of α-$FAPbI_3$ to δ-$FAPbI_3$ in the nanochannels. However, in both cases, an epitaxial relationship between the mesoporous TiO_2/nanochannel and the constrained α-$FAPbI_3$ is not necessary. In the case of the epitaxial stabilization, the α-$FAPbI_3$ is grown on the substrate with only the bottom surface chemically bonded to the substrate. The α-$FAPbI_3$ lattice is constrained to the substrate, which is the essential difference from the encapsulation method.

By comparing these two methods with the epitaxial growth, we can conclude that both the dimensional reduction and the encapsulation effect require the entire capping/encapsulation of the α-$FAPbI_3$ by either the capping agents or space-confinement

1014 objects. In the epitaxial stabilization, the epitaxial α-$FAPbI_3$ grows on the substrate and
1015 leaves the top surface and the side surfaces uncapped. The stabilization effect comes from the
1016 coherent growth of the α-$FAPbI_3$ with the substrates. During nucleation, the crystalized
1017 $FAPbI_3$ will adopt the most conformal atom sequence to accommodate the existing substrate
1018 crystal structure. Once crystallized, the formed epitaxial lattice will be constrained to the
1019 substrate due to the strong chemical bonds between them. Therefore, the epitaxial growth is
1020 also used to stabilize the polymorphs that are unstable under ambient condition[129-131]. The
1021 origin of the epitaxial stabilization actually comes from the coherent interface rather than the
1022 reduced dimension or the encapsulation effect. The epitaxial α-$FAPbI_3$ thin film strongly
1023 bonds to the substrate, leaving other surfaces uncapped. Not to mention the passivation effect
1024 of the surfactant. Therefore, we can exclude the possibility of dimensional reduction and
1025 encapsulation effects regarding the phase stabilization of α-$FAPbI_3$.

1026 Besides, a recent study shows that the residual strain produced from the thermal
1027 expansion coefficients difference during the thermal annealing can be used to temporarily
1028 stabilize the polycrystalline α-$CsPbI_3$ film[16]. However, the mechanism is different from the
1029 internal lattice strain neutralization. The isotropic (to the randomly orientated polycrystalline
1030 perovskite lattices) residual strain originates from the thermal expansion coefficients
1031 difference between the glass slide and the polycrystalline perovskites. During cooling down,
1032 the constraint from the glass will prevent the phase transition of the α-$CsPbI_3$ film. The weak
1033 constraint by van der Waals contact between the glass slides and the perovskite will be
1034 unstable against the environmental fluctuations and can gradually lose the stabilization effect.
1035 In the case of chemically epitaxially strained α-$FAPbI_3$, we suggest that strong constraint

from the ionic bond at the epitaxial interface restrict the phase transition, and neutralization of the lattice internal tensile strain can also be an important reason for stabilization. The strain we applied by epitaxial growth is an anisotropic lattice strain (to the aligned single crystal lattices), which is different from the isotropic residual strain from the reported work[16].

Supplementary Discussion 15: Composition of the Strained α-$FAPbI_3$

To study the composition of the stabilized epitaxial α-$FAPbI_3$ thin film, X-ray photoelectron spectroscopy (XPS) is used to examine the targeted key elements (I, Pb, Br, and Cl), as shown in Extended Data Fig. 8a to 8d. The results indicate a pristine surface of the epitaxy α-$FAPbI_3$ thin film without any contamination from the Br and Cl elements, which excludes the possibility of any stabilization effects by Br and Cl incorporation[48].

Supplementary Discussion 16: First-Principles Calculations of Epitaxial Stabilization

First-principles calculations were performed to investigate epitaxial stabilization of α-$FAPbI_3$ with respect to δ-$FAPbI_3$ on $MAPbBr_3$ substrates. A typical model of epitaxial stabilization calculations compares the total energy changes of nucleating the two phases on the substrate[132]. Equation (1) shows an expression of this model for this specific system:

$$\Delta E^{\alpha-\delta} = \left(\Delta E_f^{\alpha} - \Delta E_f^{\delta}\right)d + \left(\Delta E_s^{\alpha} - \Delta E_s^{\delta}\right)d + \left(\sigma^{\alpha||S} - \sigma^{\delta||S}\right) \quad (1)$$

where the terms on the right-hand side for phase i (i = α, δ) are bulk formation energy (ΔE_f^i), strain energy (ΔE_s^i), and interfacial energy ($\sigma^{i||S}$, S means substrate) terms. Here, we use

area-specific bulk energy terms (ΔE_f^i and ΔE_s^i) by setting the film thickness to d = 1 nm. The sum of the three energy-difference terms is the total energy difference between strained α-$FAPbI_3$ and δ-$FAPbI_3$ ($\Delta E^{\alpha-\delta}$). A negative $\Delta E^{\alpha-\delta}$ indicates that growth of α-$FAPbI_3$ is energetically more favorable than δ-$FAPbI_3$ on the $MAPbBr_3$ substrate, and thus the metastable α-$FAPbI_3$ is epitaxially stabilized. Calculation details and results for each energy term are discussed below.

The bulk formation energy (ΔE_f^i) is the energy difference between bulk *i*-$FAPbI_3$ and its elemental components, as shown in Equation (2):

$$\Delta E_f^i = E_i - E_{FA} - E_{Pb} - 3E_I \qquad (2)$$

Because we are dealing with polymorphs with the same composition, the elemental components for both α and δ phases are the same. The total energy of the FA^+ cation is calculated based on an isolated molecule. Total energies of Pb and I are calculated using their most stable crystal structures, with a space group of *Fm*3*m* and *Cmce*, respectively. By setting the film thickness to 1 nm, we get area-specific bulk formation energies $\Delta E_f^\alpha = -2.279\times10^{-1}\,\frac{eV}{Å^2}$ and $\Delta E_f^\delta = -2.31\times10^{-1}\,\frac{eV}{Å^2}$. The results indicate that δ-$FAPbI_3$ is more stable, which agrees with the experimental findings that δ-$FAPbI_3$ is more stable than α-$FAPbI_3$ at room temperature[40].

The strain energy of *i*-$FAPbI_3$ (ΔE_s^i) is induced by constraints from the substrate due to epitaxial nucleation and lattice mismatch. It equals to the energy difference between the films with and without the strain (Equation (3)).

$$\Delta E_s^i = E_i^{strained} - E_i \qquad (3)$$

In the case of α-$FAPbI_3$, we have confirmed in the experiments that both $MAPbBr_3$ substrate

and α-$FAPbI_3$ film are (001) oriented. Our calculations also show that lattice constants of α-$FAPbI_3$ and $MAPbBr_3$ have a relatively large mismatch of 6%. Therefore, we can explicitly obtain $E_\alpha^{strained}$ in Equation (3) by calculating α-$FAPbI_3$ with 6% bi-axial compressive strain along *ab*-axes. The area-specific ΔE_s^α is calculated to be $1.2\times10^{-2}\,\frac{eV}{Å^2}$.

In the case of δ-$FAPbI_3$, the possible growth model is not straightforward. Therefore, we perform a search for the lattice plane of minimal lattice mismatch with $MAPbBr_3$ (001). The hexagonal (001) close-packed plane of δ-$FAPbI_3$ has dimensions of $a = b = 8.62$ Å and $\gamma = 120^\circ$. Based on this plane, the termination we found that is most compatible with $MAPbBr_3$ (001) substrate has a large vector strain of 13.2% and 3.43°, and an area strain of 18.3%. This obviously exceeds the strain threshold for a coherent interface, which is usually below 10% [132]. We thus consider δ-$FAPbI_3$ forms incoherent interface with $MAPbBr_3$ (001). A film with the incoherent interface is not constrained by the substrate and the strain energy ΔE_s^δ is therefore 0.

To calculate the interfacial energy for α-$FAPbI_3$ (001)/$MAPbBr_3$ (001) ($\sigma^{\alpha||S}$), we build heterostructural models consisting of *m* layers of substrate and *n* layers of film. The two heterostructural models are shown in Supplementary Fig. 13a. They represent two different terminations, namely FAI/$PbBr_2$ (m = 5, n = 9) and PbI_2/MABr (m = 5, n = 11). Note that only nine layers of film material are shown in each structure for clarity.

The other two possible terminations for the α-$FAPbI_3$ (001)/$MAPbBr_3$ (001) interfaces are FAI/MABr and PbI_2/$PbBr_2$ (not shown here). Through initial analysis of bonding characteristics, we find that these terminations cannot form ionic bonds between the film and the substrate like the Pb-I or Pb-Br bonds in FAI/MABr (PbI_2/$PbBr_2$). 'Physical contacts' like

FAI/MABr and PbI_2/$PbBr_2$ [133] at the interface are less stable than 'chemical contacts' like FAI/$PbBr_2$ and PbI_2/MABr. Therefore, we only focus on FAI/$PbBr_2$ and PbI_2/MABr in this investigation.

After the heterostructural models are confirmed, the interfacial energy can be calculated by subtracting the bulk energy of all components in the heterostructural model. Specifically, interfacial energy equations for these two heterostructural models are shown as Equations (4) and (5).

$$\sigma_{TERM1}^{\alpha||S} = \frac{1}{2A}(E_{HS1} - 2\times E_{MAPbBr_3} - 4\times E_{FAPbI_3}^{strain} - \mu_{Pb}^{MAPbBr_3} - 2\times\mu_{Br}^{MAPbBr_3} - \mu_{FA}^{FAPbI_3} - \mu_{I}^{FAPbI_3}) \quad (4)$$

$$\sigma_{TERM2}^{\alpha||S} = \frac{1}{2A}(E_{HS2} - 2\times E_{MAPbBr_3} - 5\times E_{FAPbI_3}^{strain} - \mu_{MA}^{MAPbBr_3} - \mu_{Br}^{MAPbBr_3} - \mu_{Pb}^{FAPbI_3} - 2\times\mu_{I}^{FAPbI_3}) \quad (5)$$

where E_{HS} is the total energy of the heterostructural model, E_{MAPbBr_3} is the total energy of the strain-free $MAPbBr_3$ lattice, $E_{FAPbI_3}^{strain}$ is the total energy of the strained α-$FAPbI_3$ lattice, and μ represents the chemical potentials of the corresponding atoms/molecules. Each of the heterostructural models contains two identical interfaces, and A is the interfacial area.

On the right-hand side, the trailing terms represent the bulk energy of each component in the heterostructure. For example, there are nine layers of α-$FAPbI_3$ in FAI/$PbBr_2$, which equals to four intact α-$FAPbI_3$ unit cells (each has two layers) plus one extra layer of FAI. The extra or un-stoichiometric components require the determination of their chemical potentials in the corresponding film or substrate material. Here we show in detail how we obtained chemical potentials of un-stoichiometric α-$FAPbI_3$ components.

$$\Delta\mu_{FA} + \Delta\mu_{Pb} + 3\Delta\mu_{I} = \Delta H(FAPbI_3) = -5.78\ eV \quad (6)$$

$$\Delta\mu_{Pb} + 2\Delta\mu_I < \Delta H(PbI_2) = -2.02\ eV \quad (7)$$

$$\Delta\mu_{FA} + \Delta\mu_I < \Delta H(FAI) = -3.74\ eV \quad (8)$$

According to thermodynamic stability limits expressed in Equations (6) - (8), we plot the phase diagram for α-$FAPbI_3$ against the chemical potential change $\Delta\mu_I$ and $\Delta\mu_{Pb}$. Supplementary Fig. 13b shows the phase diagram, and the long, narrow green region indicates the thermodynamic stability region for the synthesis of α-$FAPbI_3$. We select three representative points throughout the whole region for the following calculations: A ($\Delta\mu_I = -1.02\ eV$, $\Delta\mu_{Pb} = 0\ eV$), B ($\Delta\mu_I = -0.50\ eV$, $\Delta\mu_{Pb} = -1.03\ eV$), and C ($\Delta\mu_I = 0\ eV$, $\Delta\mu_{Pb} = -2.04\ eV$).

Similarly, we obtain the phase diagram for $MAPbBr_3$ substrate (not shown) and select one representative point P ($\Delta\mu_{Br} = -0.70\ eV$, $\Delta\mu_{Pb} = -1.47\ eV$) in the middle of the thermodynamically stable range. The values of point P are used as constants in Equations (4) and (5) for the un-stoichiometric $MAPbBr_3$ components.

We also added the stability limit for FAI/MABr and PbI_2/$PbBr_2$ in the phase diagram (Supplementary Fig. 13b). As the red dashed line shows, FAI/MABr is more stable in the region below this limit, and it covers the whole stability range of α-$FAPbI_3$. Therefore, we only need to calculate the interfacial energy for FAI/MABr, and the results are 2.86×10^{-4} eV Å^{-2}, 4.29×10^{-4} eV Å^{-2}, and 2.86×10^{-4} eV Å^{-2} at A, B, and C points, respectively. Interestingly, the composition of interfacial terminations and their preferred chemical potential conditions agree with each other. For the δ-$FAPbI_3$/$MAPbBr_3$ (001) interface, the interfacial energy $\sigma^{\delta||S}$ is given as 6.242×10^{-2} eV Å^{-2} (i.e., 1 J m^{-2}), a typical value for incoherent interfaces[132].

Results for all energy terms in Equation (1) are summarized in Supplementary Table 3.

The calculated total energy change of nucleating α-$FAPbI_3$ is around -2.155×10^{-1} eV $Å^{-2}$ (regardless of chemical potential conditions), while the value for δ-$FAPbI_3$ is -1.6858×10^{-1} eV $Å^{-2}$. Apparently, $\Delta E^{\alpha-\delta}$ has a negative value of around -4.7×10^{-2} eV $Å^{-2}$ (i.e., -0.75 J m^{-2}), which indicates epitaxial stabilization of α-$FAPbI_3$ with respect to δ-$FAPbI_3$ on $MAPbBr_3$ substrates. This result is comparable to prior successful prediction of epitaxial stabilization.

From Supplementary Table 3, we can see that the bulk formation energy is the largest term but yields a small difference (3.1×10^{-3} eV $Å^{-2}$) between α-$FAPbI_3$ and δ-$FAPbI_3$. The strain energy term is in favor of δ-$FAPbI_3$ by a large value of 1.2×10^{-2} eV $Å^{-2}$. The main contribution to $\Delta E^{\alpha-\delta}$ is from interfacial energy, which is above 6×10^{-2} eV $Å^{-2}$ and decides the overall energy preference. Notably, to accurately determine energetics using DFT calculations, we apply a large interfacial mismatch (strain = -6%) to calculate the strain energy term for α-$FAPbI_3$. However, the calculations represent an upper imit of strain's influence and guarantee a negative $\Delta E^{\alpha-\delta}$ in lower-strain circumstances. Strains below 6% would definitely yield a ΔE_s^{α} less than 1.2×10^{-2} eV $Å^{-2}$ and a more negative $\Delta E^{\alpha-\delta}$, which better ensures epitaxial stabilization of α-$FAPbI_3$. Another experimental variable is the substrate composition. We use $MAPbBr_3$ as the substrate in the heterostructural model to calculate the interfacial energies, but in experiments we also use mixed-halide substrates with Cl composition up to $MAPbCl_{1.50}Br_{1.50}$. This will not change the conclusion of the discussions here because the substrate energy is excluded in the calculation of the interfacial energy, as shown in Equations (4) and (5).

Besides, the consideration of the stabilization mechanism is based on the system with

both the α-$FAPbI_3$ and substrate lattices rather than just focusing on the α-$FAPbI_3$ lattice alone. Two different heterostructures (i.e., the α-$FAPbI_3$/substrate and the δ-$FAPbI_3$/substrate) are used to study the interfacial energy of nucleus crystallization during the epitaxial growth. The structure with lower interfacial energy will be more favorable during nucleus crystallization and, thus, more favorable to form. Calculation results show that the interfacial energy of the α-$FAPbI_3$/substrate (0.0286×10^{-2} eV $Å^{-2}$) is much lower than that of the δ-$FAPbI_3$/substrate (6.242×10^{-2} eV $Å^{-2}$). Therefore, the total energy of the α-$FAPbI_3$/substrate system is much smaller than that of the δ-$FAPbI_3$/substrate system because of the interfacial energy benefit, which stabilizes the epitaxial α-$FAPbI_3$ on the substrate. Additionally, the phase transition depends on not only the energy landscapes of both phases (phases before/after phase transition), but also the energy barrier between the two phases. This is where the epitaxial constraint from the substrate comes into play. In order to make the phase transition to happen, the α-$FAPbI_3$ need to break the ionic bonds with the substrate, which represents a very high energy barrier. Therefore, due to the synergistic effects of strain and epitaxial constraint, the α-$FAPbI_3$ is stable for long term as observed in this study. In summary, our calculations show reliable and robust validation of the epitaxial stabilization of α-$FAPbI_3$.

Supplementary Discussion 17: Stability Investigation of the α-$FAPbI_3$ Removed from the Substrate

Due to the constraint of the substrate lattice, the epitaxial α-$FAPbI_3$ thin film shows long-term stability without phase transition. To experimentally demonstrate the phase stability originates from the substrate lattice constriction, we partially remove the epitaxial α-$FAPbI_3$ thin film from the substrate and investigate the phase stability of the removed α-$FAPbI_3$. Due to the limited thickness of the epitaxial α-$FAPbI_3$ thin film, it is difficult to remove the epitaxial thin film by a sharp razor blade or needle. Therefore, we remove the epitaxial α-$FAPbI_3$ by polishing a substrate covered with the epitaxial α-$FAPbI_3$ thin film with a sandpaper. As shown in Supplementary Fig. 14a, removed α-$FAPbI_3$ attached to the upper half of the sandpaper while the removed substrate ($MAPbBr_3$ in this case) attached to the lower half of the sandpaper due to over-polishing. Meanwhile, the right half of the substrate, which remains unpolished, is covered with epitaxial α-$FAPbI_3$ while the left half exposes the substrate due to the removal of epitaxial α-$FAPbI_3$. The removed α-$FAPbI_3$, which attaches to the sandpaper, remains in black α phase right after removal. After 24 hours, the removed α-$FAPbI_3$ changes to yellow δ phase while the epitaxial α-$FAPbI_3$ on the right half of the substrate remains black and stable (Supplementary Fig. 14b). This experiment shows that the epitaxial stabilization of the α-$FAPbI_3$ thin film originates from the constraint by the substrate lattice and relies on the existence of the substrate. The $MAPbCl_xBr_{3-x}$ substrates are highly stable and therefore the epitaxial α-$FAPbI_3$ is expected to be highly stable as well.

Supplementary Discussion 18: Photodetectors Based on the Strained α-$FAPbI_3$

Based on the device structure and working principles, the halide perovskites photodetectors are divided into two main categories: the photodiode-type and the photoconductor-type. Here, we fabricate photodetectors with both structures and discuss them below.

1. Photodetector with a photoconductor structure

Photodetectors with a vertical photoconductor structure based on the strained α-$FAPbI_3$ thin films are fabricated with a structure shown in Supplementary Fig. 15. Compared with the photodiode-type one, the photoconductor-type photodetectors will have a much higher responsivity and the EQE will be larger than 100% due to the injected carriers[134-136]. All devices we tested have a thickness of around 1 μm. A transparent ITO electrode is deposited as the top electrode with an area of 1×1 mm^2. *I–V* characteristics are measured under -1 V bias with a 685-nm laser as the excitation source. The responsivity of the photodetectors is calculated by:

$$R = (J_{light} - J_{dark})/P,$$

where J_{light} and J_{dark} are the current densities under illumination and dark conditions, respectively, and P is the input light power density. Extended Data Fig. 9a shows the responsivity of photodetectors at different strain levels under 0.015 W cm^{-2} illumination. Compared with the strain-free device, devices at -0.8%, -1.2%, and -1.4% strain levels show enhanced responsivity. Further increasing the compressive strain level will lead to a deterioration of the responsivity due to the accumulation of defects. Supplementary Table 4 summarizes the highest responsivity measured on α-$FAPbI_3$ in the literature. The

responsivity of the device is comparable with the highest responsivity of a strain-free system with a similar device structure but at a much weaker illumination and higher bias voltage.

Besides, the detectivity, which characterizes how weak light can be detected, and the gain, which describes the number of charges flowing through an external circuit per incident photon, are calculated by:

$$D = {R}/{\sqrt{2qJ_d}} \text{ and } G = {1240R}/{685}$$

where D is the detectivity, R is the responsivity, q is element charge, J_d is the dark current density, and G is the gain. They are also plotted as a function of illumination power level for both -1.2% strained and strain-free devices (Extended Data Fig. 9b, c). Results demonstrate that the strained device has better performance than the strain-free device.

Normalized external quantum efficiency (EQE) spectra are shown in Extended Data Fig. 9d to highlight the extended absorption range of the strained device compared with the strain-free device.

2. Photodetectors with a photodiode structure

With electrons/holes blocking layers, the photodiode-type photodetectors exhibit a minimized dark current by blocking the external current injection. In this study, we aim at fabricating a detector with high responsivity. Therefore, we fabricate and test the photodetector with the photodiode structure for comparison. We fabricated a photodiode-type photodetector by inserting poly(3,4-ethylenedioxythiophene) polystyrene sulfonate (PEDOT:PSS) as the hole transporting layer and tin oxide (SnO_2) as the electron transporting layer. The structure of the photodiode type photodetector is

Au/PEDOT:PSS/$FAPbI_3$/SnO_2/ITO, which is shown in Supplementary Fig. 16a. From the band diagram, the carrier injection under reverse bias is blocked due to the large energy barrier. The characterization of the photodetector was carried out with a 685-nm red laser, which is selected based on the highest EQE wavelength, under different input power levels. Supplementary Fig. 16b shows the *I–V* curves of the photodetector under the dark condition as well as under 1 μW illumination. The *I–V* curves show a typical diode-like behavior while the dark current under -0.5 V is measured to be ~$2x10^{-8}$ A. This value is more than two orders of magnitude lower than that of the photoconductor type detector. However, under the same illumination power level, the photocurrent is much smaller than that of the photoconductor type detector (~600 times lower at a 10^{-6} W incident power), and therefore, leads to a lower responsivity (~500 times lower at a 10^{-6} W incident power). The responsivity and the photocurrent under different illumination power levels are also shown in Supplementary Fig. 16c. Under different illumination power levels, the responsivity of the photodetector is always lower than 1 A W^{-1} (in comparison with the responsivity of 200 A W^{-1} of the photoconductor type detector), indicating the block of external current injection with the presence of the different transporting layers.

Supplementary Discussion 19: Broader Impact of the Epitaxial System

The technique we developed enables the controllable strain engineering of halide perovskites with epitaxial growth, which has a fundamental difference from the previous works. The free-standing α-$FAPbI_3$ suffers from severe phase transition under room

temperature while the epitaxial strain can stabilize the α-$FAPbI_3$ without changing the perovskite composition. The pure phase α-$FAPbI_3$ with long-term stability is a property that is absent in the free-standing α-$FAPbI_3$.

Secondly, the epitaxial system we developed is a generalized approach that can presumably be applied to the entire halide perovskites family. We have already demonstrated the growth of epitaxial α-$FAPbI_3$ on various substrates, which means that we can grow various epitaxial halide perovskites on one or multiple halide perovskite substrates.

Additionally, the epitaxial strain can be applied to stabilize polymorphs of metastable perovskites. Perovskites with new compositions are recently predicted through computational designs[137]. However, those predicted new perovskites with novel optical and electronic properties may have unstable crystal structures under room temperature or normal working conditions. In this case, epitaxial stabilization can potentially be applied to stabilize these unstable or metastable perovskites on suitable substrates. The reported approach can be generalized to other halide perovskites with different compositions and structures.

Supplementary Table 1. Summary of the substrate growth precursor ratios, the resulting substrate compositional Br ratios, and lattice parameters.

Cl/Br Solution Ratio	Compositional Br Ratio (%)	Formula	Lattice Parameter (Å)
Cl Only	0	$MAPbCl_{3.00}Br_{0.00}$	5.70
1/2	50.0	$MAPbCl_{1.50}Br_{1.50}$	5.83
1/2.5	58.0	$MAPbCl_{1.25}Br_{1.75}$	5.86
1/3	62.1	$MAPbCl_{1.15}Br_{1.85}$	5.87
1/4	64.3	$MAPbCl_{1.05}Br_{1.95}$	5.88
1/6	76.8	$MAPbCl_{0.70}Br_{2.30}$	5.89
1/8	80.6	$MAPbCl_{0.60}Br_{2.40}$	5.90
1/19	85.2	$MAPbCl_{0.45}Br_{2.55}$	5.92
Br Only	100	$MAPbCl_{0.00}Br_{3.00}$	5.95

Supplementary Table 2. Summary of epitaxial growth substrates and the corresponding strain measured in α-$FAPbI_3$.

Substrate Composition	α-$FAPbI_3$ (001) Peak (degree)	Strain (%)
$MAPbCl_{1.50}Br_{1.50}$	13.82	-2.4
$MAPbCl_{1.05}Br_{1.95}$	13.84	-1.9
$MAPbCl_{0.70}Br_{2.30}$	13.86	-1.4
$MAPbCl_{0.60}Br_{2.40}$	13.87	-1.2
$MAPbCl_{0.00}Br_{3.00}$	13.89	-0.8

Supplementary Table 3. Thermodynamic terms relevant to epitaxial nucleation of α-$FAPbI_3$ and δ-$FAPbI_3$ on cubic $MAPbBr_3$ substrates.

	α-$FAPbI_3$			δ-$FAPbI_3$
	A	**B**	**C**	**--**
ΔE_f	-22.79×10^{-2}			-23.10×10^{-2}
ΔE_s	1.20×10^{-2}			0
σ	0.0286×10^{-2}	0.0429×10^{-2}	0.0286×10^{-2}	6.242×10^{-2}*
ΔE	-21.5614×10^{-2}	-21.5471×10^{-2}	-21.5614×10^{-2}	-16.858×10^{-2}
ΔE (α-δ)	-4.7034×10^{-2}	-4.6891×10^{-2}	-4.7034×10^{-2}	--

The bulk formation energy (ΔE_f), strain energy (ΔE_s), interfacial energy (σ), total energy change (ΔE), and the difference between of the two phases (ΔE (α-δ)) are in eV $Å^{-2}$. The value marked with * indicates that the interface between the substrate and the δ-$FAPbI_3$ is considered incoherent, and the interfacial energy term is set at 1 J m^{-2} = 6.242×10^{-2} eV $Å^{-2}$.

Supplementary Table 4. Summary of representative halide perovskite photodetectors with high responsivities in the literature.

Device structure	Structure	Highest R	Light power	Bias	References
Au/$MAPbBr_3$/Au	Planar	~10 A W^{-1}	0.01 mW cm^{-2}	-2 V	[138]
Cr/$MAPbI_3$/Cr	Planar	~20 A W^{-1}	0.1 mW cm^{-2}	-1 V	[139]
Au/$MAPbI_3$/Au	Planar	~20.4 A W^{-1}	2 μW cm^{-2}	-1.5 V	[140]
Au/$MAPbBr_3$/Au	Planar	40 A W^{-1}	54 μW	-5 V	[141]
Au/ $(BA)_2(MA)_{n-1}Pb_nI_{3n+1}$ NWs/Au	Planar	2×10^4 A W^{-1}	10^{-6} mW cm^{-2}	-2 V	[106]
Au/$FAPbI_3$/ITO	Vertical	1.3×10^6 A W^{-1}	1.1×10^{-7} W cm^{-2}	-1 V	This Work

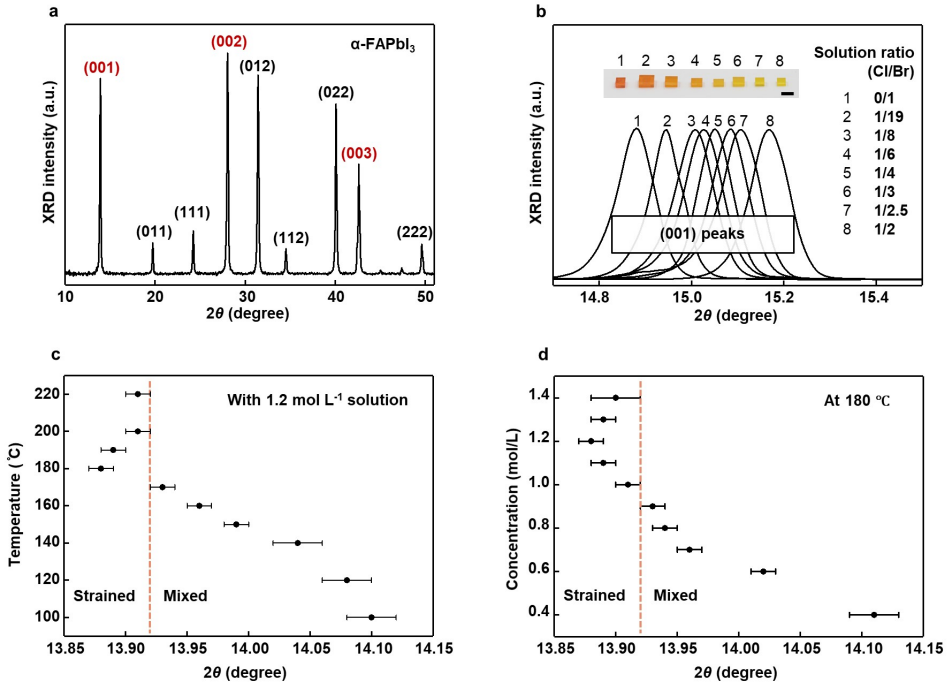

Supplementary Fig. 1 | Characterization of the lattice parameters and the study of growth condition. a, Powder XRD pattern of α-$FAPbI_3$, which is used as a reference of strain-free α-$FAPbI_3$. The lattice parameter of cubic α-$FAPbI_3$ is calculated to be 6.35 Å using the (001) diffraction peak at 13.92°. Peaks from {001} directions are labeled in red. **b**, Powder XRD patterns of substrates with different ratios of the composition. By tuning the Cl/Br molar ratio in the growth solution, we can change the Cl/Br ratio as well as the lattice parameter of the substrate crystal. We note that $MAPbCl_{3.00}Br_{0.00}$, $MAPbCl_{0.00}Br_{3.00}$, and their alloys all have cubic structures. Lattice parameters can be directly calculated by the 2θ peak positions. The inset is an optical image of the corresponding substrates with different Cl/Br ratios. All powders are made by grinding the bulk single crystals. Scale bar: 5 mm. **c**, XRD (100) peak positions of α-$FAPbI_3$ at different growth temperatures. The temperature to grow α-$FAPbI_3$ with the highest strain is found to be ~180℃. Further increasing the growth temperature results in a high growth rate and a thick epitaxial layer of α-$FAPbI_3$ and therefore low crystal quality that relaxes the strain. Decreasing the growth temperature below 180℃ can lead to slow crystallization and thus a mixed epitaxial alloy layer at the interface, which shifts the XRD peak position to higher angles. **d**, XRD (100) peak positions of α-$FAPbI_3$ at different growth solution concentrations. Concentrations above 1.2 mol L^{-1} result in high defect concentration and therefore strain relaxation, due to the fast crystallization rate and the thick epitaxial layer. Concentrations below 1.0 mol L^{-1} will slow down the crystallization process and lead to a mixed epitaxial alloy layer at the interface. The vertical dash lines in **c** and **d** show the peak position of a strain-free powder sample. (a.u., arbitrary units).

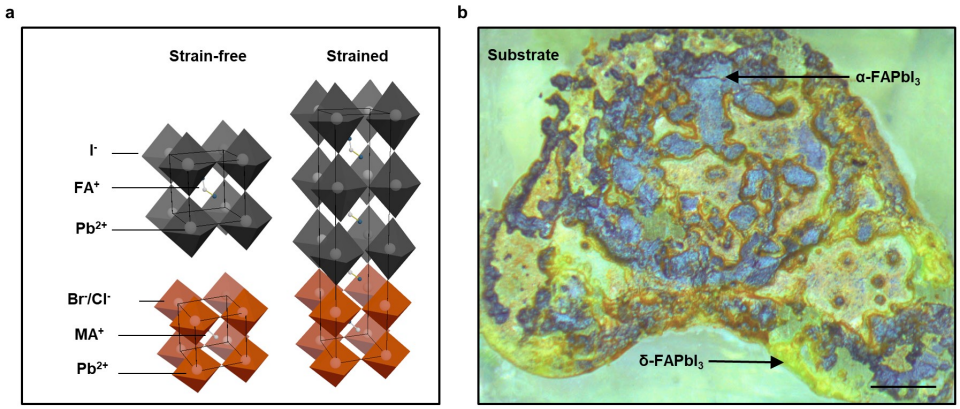

Supplementary Fig. 2 | Schematic crystal structures of epitaxial α-$FAPbI_3$ on $MAPbCl_xBr_{3-x}$ and the optical image of α-$FAPbI_3$ on a Cl-rich substrate. a, Schematic crystal structures of α-$FAPbI_3$, $MAPbCl_xBr_{3-x}$, and the epitaxial heterostructure showing the crystallographic orientation of the epitaxial α-$FAPbI_3$ and the $MAPbCl_xBr_{3-x}$ substrate, with distorted PbI_6 octahedron inorganic framework in the epitaxial layer under compressive interfacial strain. **b**, An optical image of $FAPbI_3$ grown on $MAPbCl_{2.00}Br_{1.00}$ substrate using the same growth method as the other substrates. Due to the large lattice mismatch between the substrate and α-$FAPbI_3$, the α-$FAPbI_3$ crystallizes randomly rather than epitaxially on the substrate surface. The lack of epitaxial stabilization leads to quick phase transformation from metastable α-$FAPbI_3$ to δ-$FAPbI_3$ at room temperature. Scale bar: 200 μm.

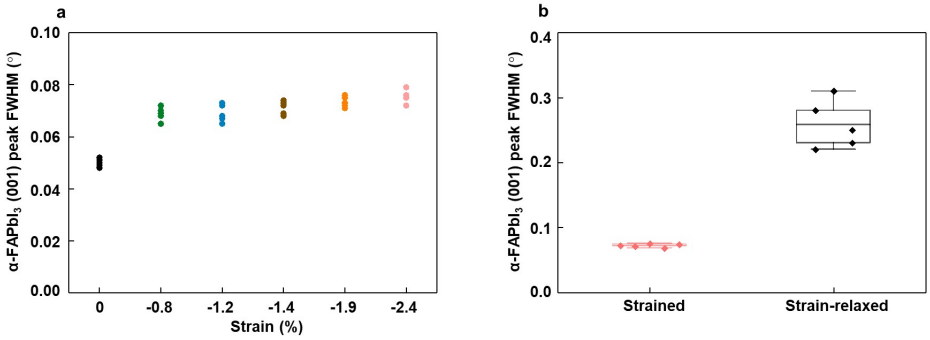

Supplementary Fig. 3 | XRD diffraction peak FWHM. a, Diffraction peak FWHM study of the epitaxial α-$FAPbI_3$ thin films under different strain magnitudes. Results show that the epitaxially strained α-$FAPbI_3$ thin films have a relatively higher diffraction peak FWHM than that of the strain-free α-$FAPbI_3$ crystal due to the lattice strain and the reduced dimension. **b**, statistical study of the α-$FAPbI_3$ (001) peak FWHM of the strained and the strain-relaxed samples. Results show that the diffraction peak FWHM of the strained epitaxial α-$FAPbI_3$ thin films (~0.07°) is ~3 times smaller than that of the strain-relaxed one (~0.25°). Note the strain-relaxed epitaxial α-$FAPbI_3$ thin films come from Extended Data Fig. 1g. Number of experiments $n = 5$ for each strain value.

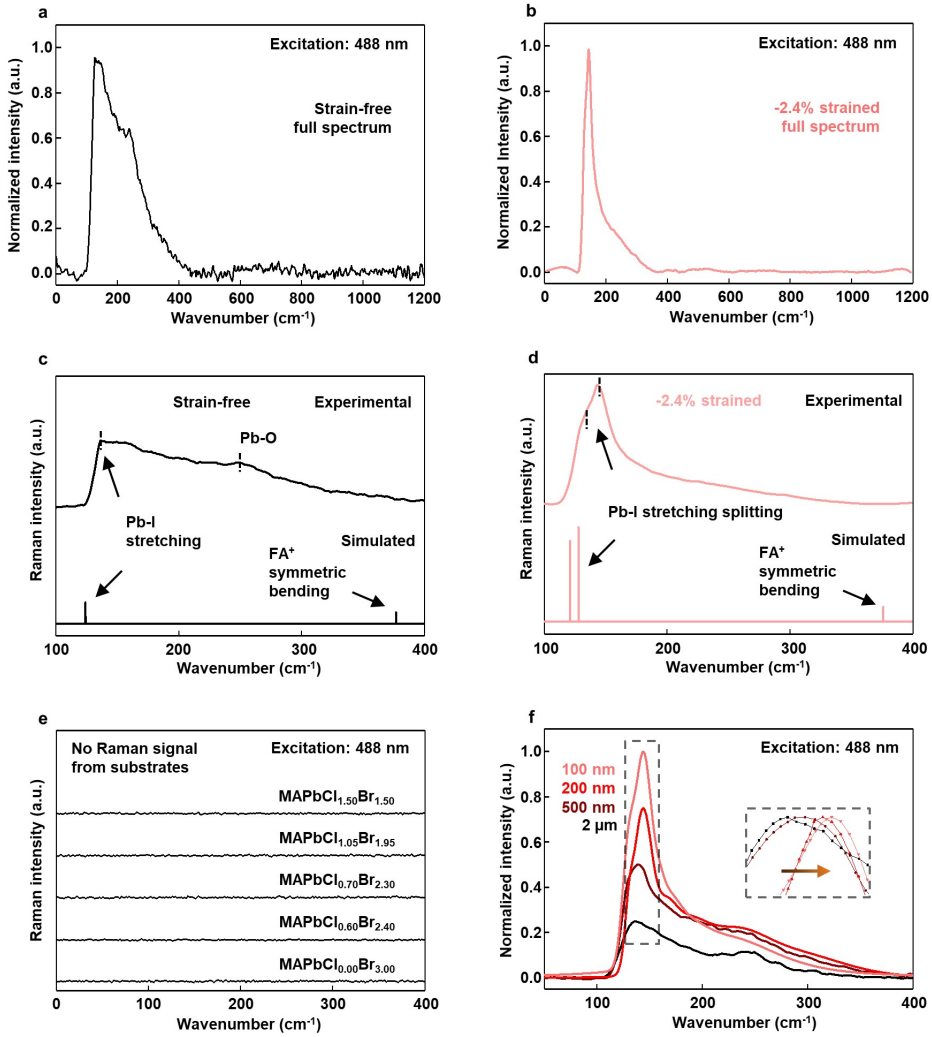

Supplementary Fig. 4 | Raman spectra of α-$FAPbI_3$ and the substrates. Raman full spectra of **a**, strain-free α-$FAPbI_3$ bulk crystal and **b**, -2.4% strained α-$FAPbI_3$ thin film showing the absence of other peaks outside the range of 100 to 400 cm^{-1}. The strain-free α-$FAPbI_3$ crystal is less Raman-active than the strained α-$FAPbI_3$ thin film, so the relative peak intensity of the strain-free crystal is much weaker. The comparison of the experimental and simulated Raman spectra of the **c**, strain-free, and **d**, -2.4% strained α-$FAPbI_3$ lattices. The discrepancy between experimental and simulated Pb-I stretching wavenumbers may be due to the anharmonicity of the bonds and the van der Waals interactions between the inorganic cages and organic cations. For the strained lattice, an obvious peak splitting takes place in both the experimental and the simulated spectra. The splitting of the Pb-I symmetric stretching peak originates from the in-plane compression and out-of-plane stretching, while the intensity enhancement comes from the breakage of the cubic symmetry. The weak FA^+ cation bending peak at 377 cm^{-1} fails to be detected, which is due to the dynamic FA^+ cation rotation at room temperature. **e**, Raman spectra of $MAPbCl_{0.00}Br_{3.00}$, $MAPbCl_{0.60}Br_{2.40}$, $MAPbCl_{0.70}Cl_{2.30}$, $MAPbCl_{1.05}Br_{1.95}$, and $MAPbCl_{1.50}Br_{1.50}$ substrates with a 488-nm laser as the excitation source. No Raman signals can be detected in the wavenumber range of interest. Therefore, possible interference from the substrates can be excluded. **f**, Thickness-dependent Raman spectra of -2.4% strained α-$FAPbI_3$ samples. Strained α-$FAPbI_3$ thin film has a sharp

and strong signal, which can be attributed to the increased tetragonality of the crystal structure. As the film thickness increases, the strain gets gradually relaxed and the lattice transforms back to less Raman-active cubic structure. The Raman peak position also shifts to lower wavenumbers because of the softer and longer Pb-I bonds (inset image).

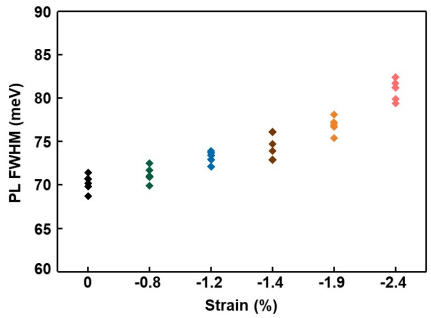

Supplementary Fig. 5 | FWHM of the PL peaks of epitaxial layers under different strains. The results show that the FWHM of the PL peak increases with the strain, due to the strain-induced dislocations that broaden the PL peak. A bulk α-$FAPbI_3$ single crystal is used as the strain-free reference. Note the number of experiments $n = 5$ for each strain value.

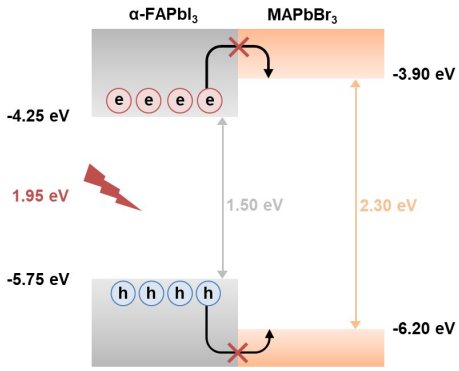

Supplementary Fig. 6 | Band diagram of the heterostructure and the interfacial charge transfer. Excited carriers in the α-$FAPbI_3$ will not transfer to the $MAPbBr_3$ due to the energy barrier. The analysis shows that the charged carrier transfer in the heterojunction can be excluded due to the straddling band alignment with a prohibited carrier transfer direction and a large energy barrier.

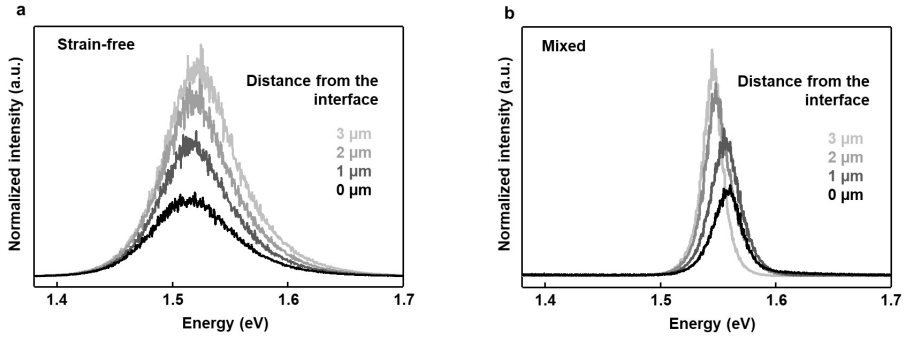

Supplementary Fig. 7 | Focal point dependent PL measurements of strain-free and mixed α-$FAPbI_3$. a, Focal-point-dependent confocal PL spectra of a strain-free α-$FAPbI_3$ bulk crystal. The redshift of the PL peak from ~1.523 eV to ~1.516 eV, less pronounced than the PL peak redshift of the strained sample in Fig. 2b, is due to reabsorption. **b**, Focal-point-dependent confocal PL spectra of a mixed epitaxial α-$FAPbI_3$ grown at a low temperature. Note the mixed sample came from the mixed epitaxial growth with low temperature and low concentration in Supplementary Fig. 1. The increase of focus depth causes the PL peak to blueshift, due to the increase of Br and Cl incorporation in the epitaxial layer.

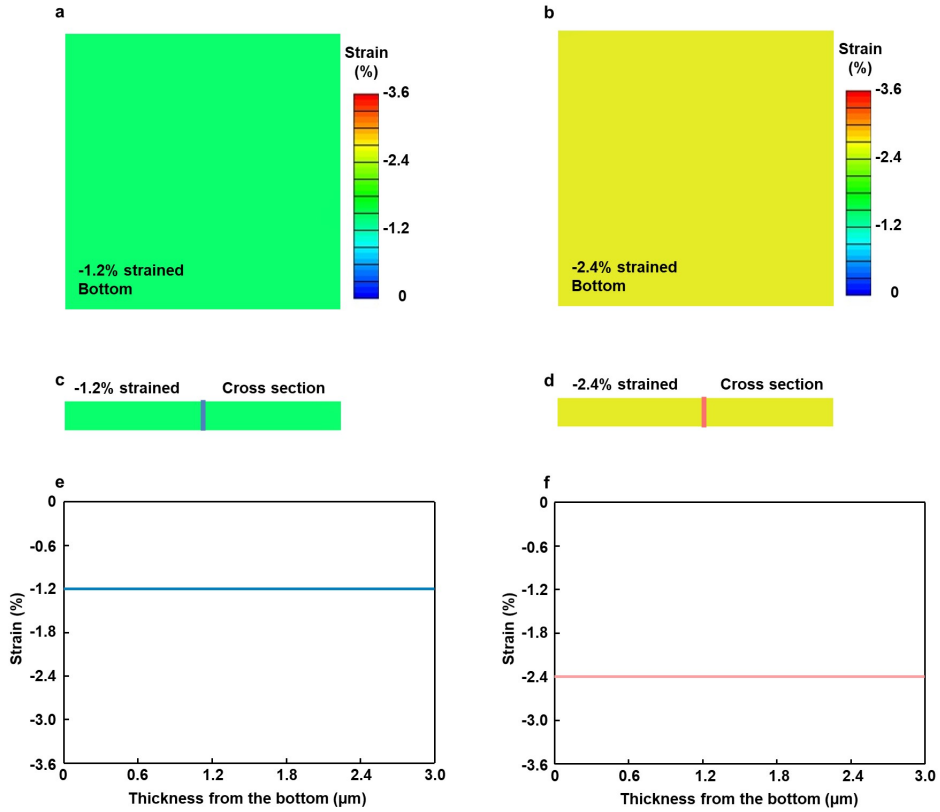

Supplementary Fig. 8 | Elastic strain relaxation study of the epitaxial α-$FAPbI_3$ thin films. Planar strain distribution of the α-$FAPbI_3$ with **a,** -1.2% and **b,** -2,4% strain. Vertical strain distribution of the α-$FAPbI_3$ with **c,** -1.2% and **d,** -2,4% strain. Results show uniform strain distribution in both α-$FAPbI_3$ thin films. Thickness-dependent strain distribution of the α-$FAPbI_3$ with **e,** -1.2% and **f,** -2,4% strain. Colors are correlated with the lines in **c** and **d**. Results indicate that the elastic strain relaxations in both α-$FAPbI_3$ thin film are 0.096% and 0.093%, respectively.

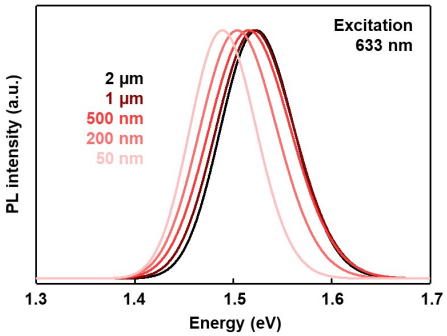

Supplementary Fig. 9 | Film-thickness-dependent PL measurements of epitaxial α-$FAPbI_3$ on $MAPbCl_{1.50}Br_{1.50}$. The PL properties of strained α-$FAPbI_3$ films show a strong thickness dependence. As the film thickness increases, the PL position gradually shifts back to the position of the free-standing bulk crystals. This can be attributed to the plastic strain relaxation as the film gets thicker.

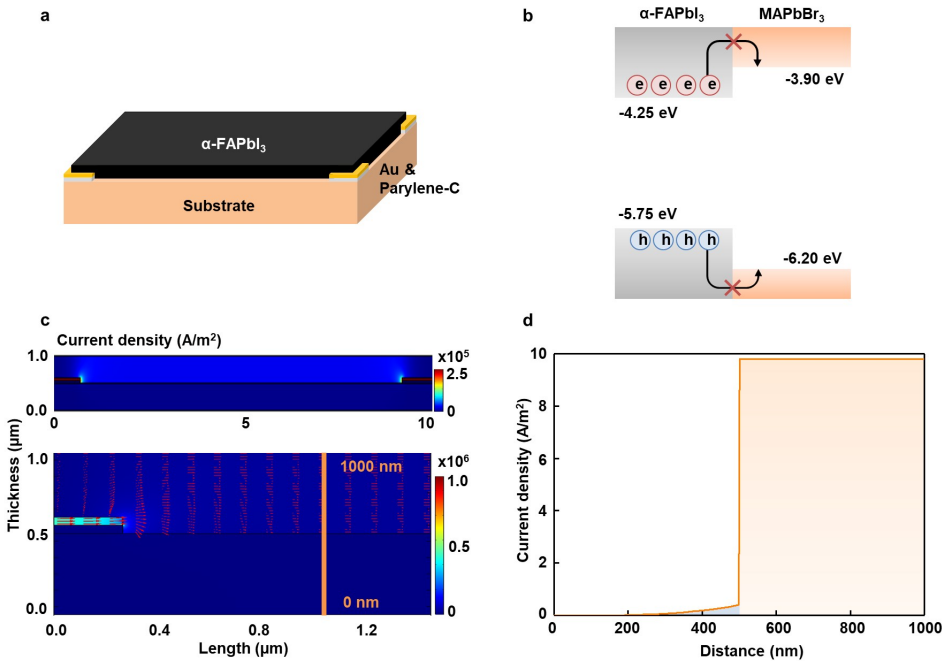

Supplementary Fig. 10 | Possible carrier collection by the interfacial carrier transfer during Hall effect measurements. a, The schematic structure of the device. Parylene-C (grey) is used as an insulating layer to prevent the injection of carriers from the Au electrode (yellow) to the substrate. **b**, The bandgap diagram of the heterostructure shows that the large energy barrier between the α-$FAPbI_3$ and the $MAPbBr_3$ blocks the carrier injection to the $MAPbBr_3$. **c**, Current density distribution by FEA simulation. The upper panel shows the current mapping where the current density in the epitaxial layer is much higher than that of the substrate. The lower panel shows the zoomed-in current distribution image around the electrode. Red arrows show the direction of current flow, which suggests a minimal carrier injection into the substrate due to the energy. **d**, Current density distribution along the vertical orange line in **c**, where the current in the substrate takes 0.8% of the total current.

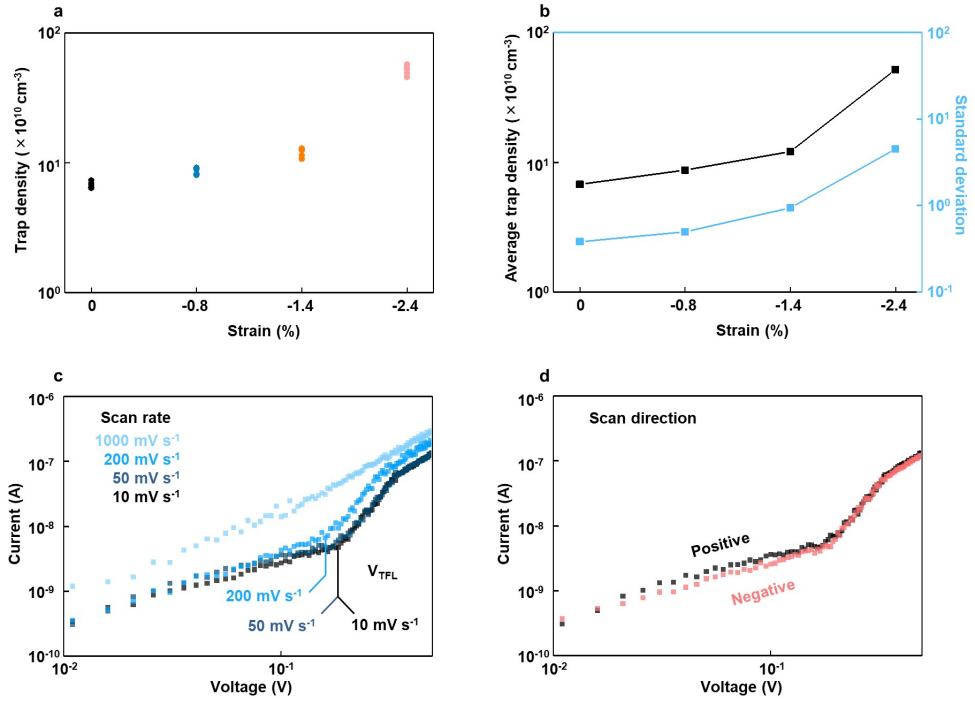

Supplementary Fig. 11 | SCLC measurements of the epitaxial α-$FAPbI_3$ with different strains. a, Strain-dependent trap density of the epitaxial α-$FAPbI_3$. Note the number of experiments n = 5 for each strain value. **b,** Statistics of the strain-dependent trap density. Results show that the average trap density will increase with increasing the strain, which can be attributed to the strain-induced defects. Meanwhile, the standard deviation of the trap density values also increases with the strain, indicating the increased disorder due to the higher defect density with the strain. **c**, Scan-rate-dependent *I–V* curves. *I–V* curves with 10 mV s^{-1} and 50 mV s^{-1} scan rates are similar, indicating that these scan rates are sufficiently slow to avoid artificial results. The *I–V* curve with 200 mV s^{-1} results in a smaller V_{TFL} because of the limited response of free carriers from the fast scan. Further increasing the scan rate to 1000 mV s^{-1} leads to the vanish of the trap-filling process. **d**, *I–V* curves with different scan directions of the same device. The high similarity of the two curves concludes that the scan direction will not affect the SCLC measurements due to the symmetric Au/Perovskite/Au device structure.

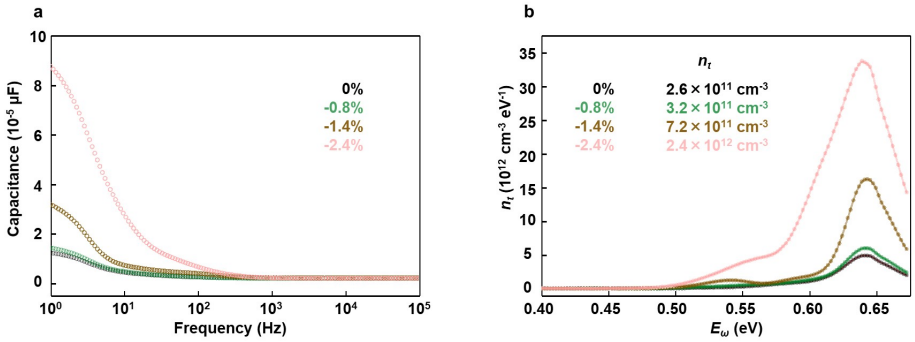

Supplementary Fig. 12 | *C-ω* measurements of the epitaxial α-$FAPbI_3$ to evaluate the trap density. a, *C-ω* spectra of the epitaxial α-$FAPbI_3$ thin films with different strain magnitudes. The low-frequency capacitance originates from the carrier trapping/detrapping processes. The larger capacitance at a higher strain magnitude suggests a higher density of traps. The high-frequency capacitance is attributed to the geometrical capacitance and the depletion capacitance. **b**, Trap density distribution extracted from the *C-ω* spectra. An obvious trap density increment is evident with increasing the strain magnitude. The fitted trap densities (n_t) by the Gaussian distribution equation indicate a higher trap density at a higher strain magnitude.

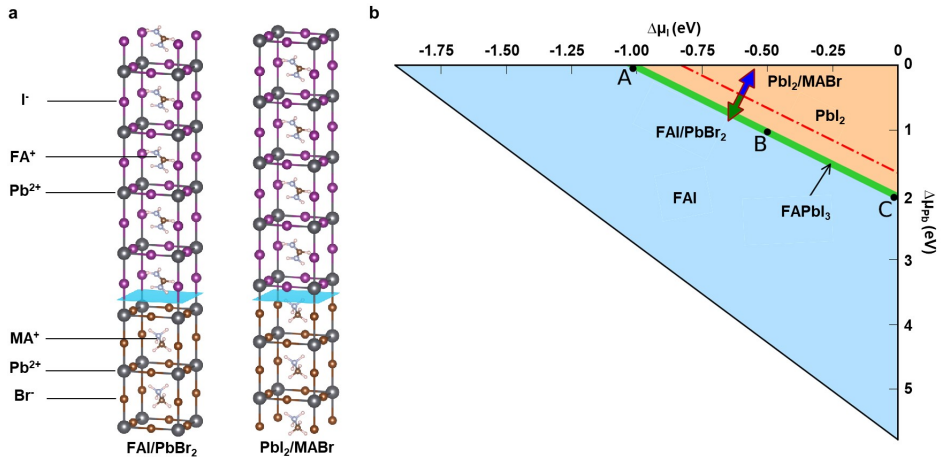

Supplementary Fig. 13 | First-principles calculations of epitaxial stabilization. a, Schematic heterostructural models used to calculate the epitaxial α-$FAPbI_3$ (001)/$MAPbBr_3$ (001) interface. The two interface terminations studied are FAI/$PbBr_2$ and PbI_2/MABr. In each model, the blue plane indicates the interface, the upper section indicates the $FAPbI_3$ film, and the lower section indicates the $MAPbBr_3$ substrate. **b**, Calculated phase diagram for α-$FAPbI_3$ and epitaxial α-$FAPbI_3$ (001)/$MAPbBr_3$ interface. The long, narrow region marked in green depicts the thermodynamically stable range for equilibrium growth of α-$FAPbI_3$ under different I and Pb chemical potentials. Outside this region, the compound decomposes into FAI or PbI_2. Three representative points A ($\Delta\mu_I$ = −1.02 eV, $\Delta\mu_{Pb}$ = 0 eV), B ($\Delta\mu_I$ = −0.50 eV, $\Delta\mu_{Pb}$ = −1.03 eV), and C ($\Delta\mu_I$ = 0 eV, $\Delta\mu_{Pb}$ = −2.04 eV) are selected for calculating the interfacial energy. The red dashed line separates the phase diagram into stability regions of the two different interfacial terminations in **a**. μ represents the chemical potentials of the corresponding atoms.

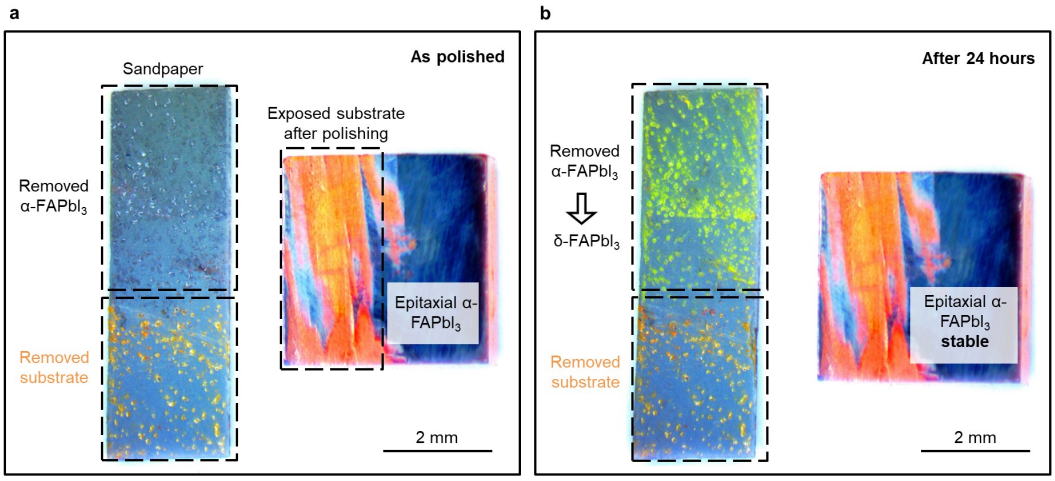

Supplementary Fig. 14 | Stability investigation of the epitaxial and the removed α-$FAPbI_3$. Images of the **a**, as-polished and the **b**, 24-hour aged epitaxial α-$FAPbI_3$ thin film. The left half of the epitaxial α-$FAPbI_3$ thin film is removed by a sandpaper while the right half of the epitaxial α-$FAPbI_3$ thin film remains on the substrate. Removed α-$FAPbI_3$ that is attached to the upper half of the sandpaper suffers from phase transition from black α phase to yellow δ phase after 24 hours. The epitaxial α-$FAPbI_3$ thin film remains on the substrate is stable without phase transition. Results show the epitaxial stabilization of the epitaxial α-$FAPbI_3$ thin film relies on the constraint from the substrate lattices.

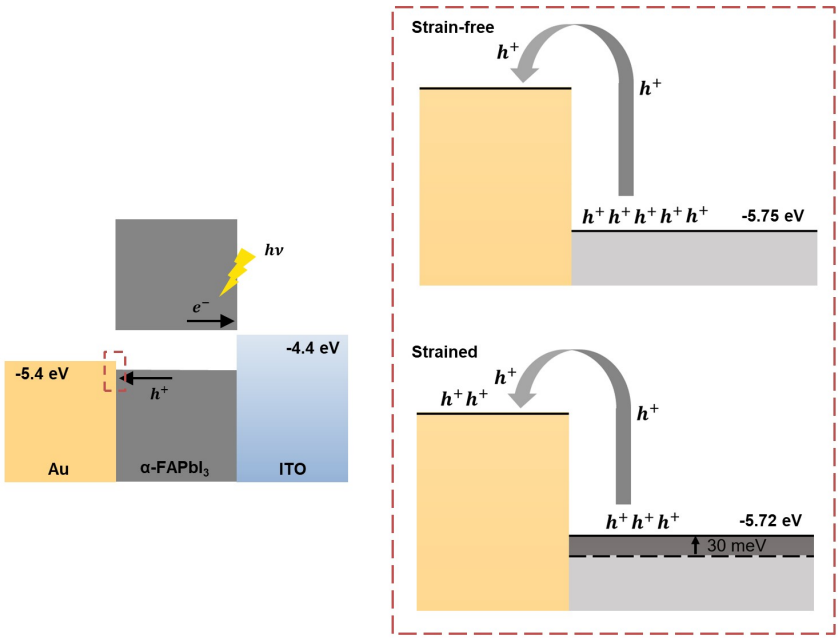

Supplementary Fig. 15 | Schematic band diagrams of photodetectors. Left panel is the flat band diagram of the photodetector. Due to the compressive strain, the VBM of α-$FAPbI_3$ at the interface will be pushed up and align better with the Au Fermi level (-5.4 eV), which allows better hole transfer from α-$FAPbI_3$ to Au and therefore enhances the device performance.

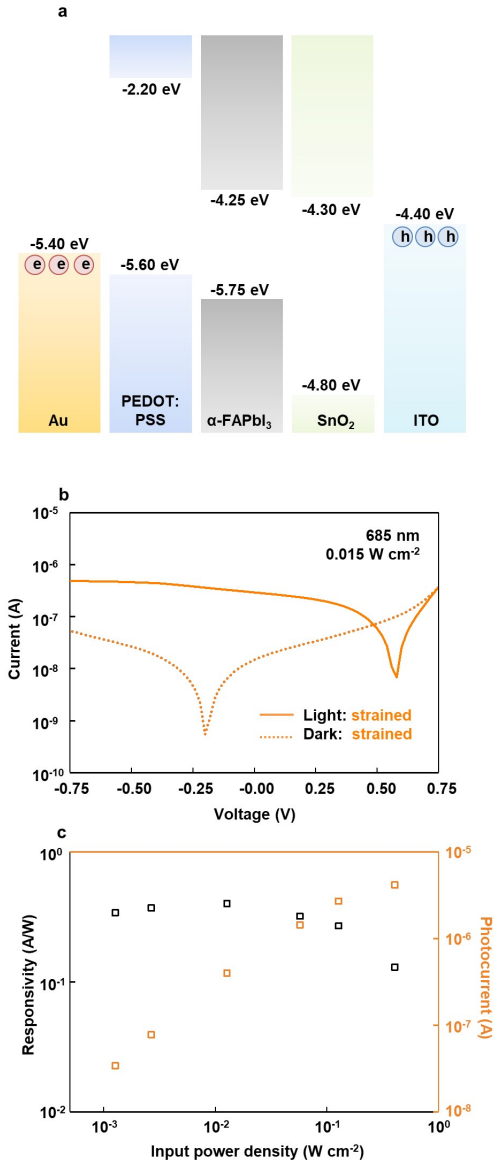

Supplementary Fig. 16 | Photodiode-type photodetector characterizations. a, The band diagram of the photodetector. An Au/PEDOT:PSS/α-$FAPbI_3$/SnO_2/ITO structure is used to build a photodiode. In this structure, the injection of external carriers under reverse bias is efficiently blocked due to the large energy barrier. **b,** *I–V* curves the photodetector. The dark current is reduced to ~10^{-8} A due to the diode structure. **c,** Responsivity and photocurrent of the photodetector under different illumination power levels. Results show that the responsivity is lower than 1 with the diode structure.

References

1 Sun, M. *et al.* All-Inorganic Perovskite Nanowires-InGaZnO Heterojunction for High-Performance Ultraviolet-Visible Photodetectors. *ACS Appl Mater Interfaces* **10**, 7231-7238, (2018).

2 Chen, J. *et al.* Single-Crystal Thin Films of Cesium Lead Bromide Perovskite Epitaxially Grown on Metal Oxide Perovskite (SrTiO3). *Journal of the American Chemical Society* **139**, 13525-13532, (2017).

3 Oksenberg, E., Sanders, E., Popovitz-Biro, R., Houben, L. & Joselevich, E. Surface-Guided CsPbBr3 Perovskite Nanowires on Flat and Faceted Sapphire with Size-Dependent Photoluminescence and Fast Photoconductive Response. *Nano Lett* **18**, 424-433, (2018).

4 Wang, Y. *et al.* Nontrivial strength of van der Waals epitaxial interaction in soft perovskites. *Physical Review Materials* **2**, 076002, (2018).

5 Wang, Y. *et al.* High-Temperature Ionic Epitaxy of Halide Perovskite Thin Film and the Hidden Carrier Dynamics. *Advanced Materials* **29**, (2017).

6 Wang, L. *et al.* Unlocking the Single‐Domain Epitaxy of Halide Perovskites. *Advanced Materials Interfaces*, (2017).

7 Li, X., Luo, Y., Holt, M. V., Cai, Z. & Fenning, D. P. Residual Nanoscale Strain in Cesium Lead Bromide Perovskite Reduces Stability and Shifts Local Luminescence. *Chemistry of Materials*, (2019).

8 Wang, Y. *et al.* Defect-engineered epitaxial VO2±δ in strain engineering of heterogeneous soft crystals. *Science Advances* **4**, eaar3679, (2018).

9 Saidaminov, M. I. *et al.* Suppression of atomic vacancies via incorporation of isovalent small ions to increase the stability of halide perovskite solar cells in ambient air. *Nature Energy*, (2018).

10 Zheng, X. *et al.* Improved Phase Stability of Formamidinium Lead Triiodide Perovskite by Strain Relaxation. *ACS Energy Letters* **1**, 1014-1020, (2016).

11 Shai, X. *et al.* Achieving ordered and stable binary metal perovskite via strain engineering. *Nano Energy* **48**, 117-127, (2018).

12 Tsai, H. *et al.* Light-induced lattice expansion leads to high-efficiency perovskite solar cells. *Science* **360**, 67-70, (2018).

13 Jones, T. W. *et al.* Lattice strain causes non-radiative losses in halide perovskites. *Energy & Environmental Science* **12**, 596-606, (2019).

14 Zhao, J. *et al.* Strained hybrid perovskite thin films and their impact on the intrinsic stability of perovskite solar cells. *Science Advances* **3**, eaao5616, (2017).

15 Zhu, C. *et al.* Strain engineering in perovskite solar cells and its impacts on carrier dynamics. *Nature Communications* **10**, 815, (2019).

16 Steele, J. A. *et al.* Thermal unequilibrium of strained black CsPbI3 thin films. *Science*, eaax3878, (2019).

17 Lü, X. *et al.* Enhanced Structural Stability and Photo Responsiveness of CH3NH3SnI3 Perovskite via Pressure-Induced Amorphization and Recrystallization. *Advanced Materials* **28**, 8663-8668, (2016).

18 Liu, G. *et al.* Pressure‐Induced Bandgap Optimization in Lead‐Based Perovskites with Prolonged Carrier Lifetime and Ambient Retainability. *Advanced Functional Materials* **27**,

(2017).
19 Liu, S. *et al.* Manipulating efficient light emission in two-dimensional perovskite crystals by pressure-induced anisotropic deformation. *Science Advances* **5**, eaav9445, (2019).
20 Ma, Z. *et al.* Pressure-induced emission of cesium lead halide perovskite nanocrystals. *Nature Communications* **9**, 4506, (2018).
21 Jaffe, A., Lin, Y., Mao, W. L. & Karunadasa, H. I. Pressure-induced metallization of the halide perovskite (CH3NH3) PbI3. *Journal of the American Chemical Society* **139**, 4330-4333, (2017).
22 Han, Q. *et al.* Single Crystal Formamidinium Lead Iodide (FAPbI3): Insight into the Structural, Optical, and Electrical Properties. *Advanced Materials* **28**, 2253-2258, (2016).
23 Wang, W. F. *et al.* Growth of mixed-halide perovskite single crystals. *Crystengcomm* **20**, 1635-1643, (2018).
24 Fang, Y., Dong, Q., Shao, Y., Yuan, Y. & Huang, J. Highly narrowband perovskite single-crystal photodetectors enabled by surface-charge recombination. *Nature Photonics* **9**, 679, (2015).
25 Saidaminov, M. I. *et al.* High-quality bulk hybrid perovskite single crystals within minutes by inverse temperature crystallization. *Nature Communications* **6**, 7586, (2015).
26 Lei, Y. *et al.* Controlled Homoepitaxial Growth of Hybrid Perovskites. *Advanced Materials* **30**, 1705992, (2018).
27 Suryanarayana, C. & Norton, M. G. *X-ray diffraction: a practical approach*. (Springer Science & Business Media, 2013).
28 Birkholz, M. *Thin film analysis by X-ray scattering*. (John Wiley & Sons, 2006).
29 Gubicza, J. *X-ray line profile analysis in materials science*. (IGI Global, 2014).
30 Hartmann, J. M., Abbadie, A. & Favier, S. Critical thickness for plastic relaxation of SiGe on Si(001) revisited. *Journal of Applied Physics* **110**, 083529, (2011).
31 Steele, J. A. *et al.* Direct Laser Writing of δ- to α-Phase Transformation in Formamidinium Lead Iodide. *ACS Nano* **11**, 8072-8083, (2017).
32 Frank, O. *et al.* Raman 2D-Band Splitting in Graphene: Theory and Experiment. *ACS Nano* **5**, 2231-2239, (2011).
33 Chen, J. *et al.* Probing Strain in Bent Semiconductor Nanowires with Raman Spectroscopy. *Nano Letters* **10**, 1280-1286, (2010).
34 Mohiuddin, T. M. G. *et al.* Uniaxial strain in graphene by Raman spectroscopy:Gpeak splitting, Grüneisen parameters, and sample orientation. *Physical Review B* **79**, 205433, (2009).
35 Quarti, C. *et al.* The Raman spectrum of the CH3NH3PbI3 hybrid perovskite: interplay of theory and experiment. *The journal of physical chemistry letters* **5**, 279-284, (2013).
36 Pérez-Osorio, M. A. *et al.* Raman Spectrum of the Organic–Inorganic Halide Perovskite CH3NH3PbI3 from First Principles and High-Resolution Low-Temperature Raman Measurements. *The Journal of Physical Chemistry C*, (2018).
37 Pering, S. R. *et al.* Azetidinium lead iodide for perovskite solar cells. *Journal of Materials Chemistry A* **5**, 20658-20665, (2017).
38 Steele, J. A. *et al.* Direct Laser Writing of δ-to α-Phase Transformation in Formamidinium Lead Iodide. *ACS nano*, (2017).
39 Niemann, R. G. *et al.* Halogen Effects on Ordering and Bonding of CH3NH3+ in CH3NH3PbX3 (X = Cl, Br, I) Hybrid Perovskites: A Vibrational Spectroscopic Study. *The Journal of Physical*

Chemistry C **120**, 2509-2519, (2016).

40 Chen, T. *et al.* Entropy-driven structural transition and kinetic trapping in formamidinium lead iodide perovskite. *Science advances* **2**, e1601650, (2016).

41 Taylor, V. C. A. *et al.* Investigating the Role of the Organic Cation in Formamidinium Lead Iodide Perovskite Using Ultrafast Spectroscopy. *The Journal of Physical Chemistry Letters* **9**, 895-901, (2018).

42 Govinda, S. *et al.* Critical Comparison of FAPbX3 and MAPbX3 (X = Br and Cl): How Do They Differ? *The Journal of Physical Chemistry C* **122**, 13758-13766, (2018).

43 Nakada, K., Matsumoto, Y., Shimoi, Y., Yamada, K. & Furukawa, Y. Temperature-Dependent Evolution of Raman Spectra of Methylammonium Lead Halide Perovskites, CH3NH3PbX3 (X = I, Br). *Molecules* **24**, 626, (2019).

44 Ledinský, M. *et al.* Raman Spectroscopy of Organic–Inorganic Halide Perovskites. *The Journal of Physical Chemistry Letters* **6**, 401-406, (2015).

45 Li, D. *et al.* Size-dependent phase transition in methylammonium lead iodide perovskite microplate crystals. *Nature Communications* **7**, 11330, (2016).

46 Sarmah, S. P. *et al.* Double Charged Surface Layers in Lead Halide Perovskite Crystals. *Nano Letters* **17**, 2021-2027, (2017).

47 Kanemitsu, Y. Luminescence spectroscopy of lead-halide perovskites: materials properties and application as photovoltaic devices. *Journal of Materials Chemistry C* **5**, 3427-3437, (2017).

48 Xie, L.-Q. *et al.* Understanding the Cubic Phase Stabilization and Crystallization Kinetics in Mixed Cations and Halides Perovskite Single Crystals. *Journal of the American Chemical Society* **139**, 3320-3323, (2017).

49 Wenger, B. *et al.* Consolidation of the optoelectronic properties of CH3NH3PbBr3 perovskite single crystals. *Nature communications* **8**, 590, (2017).

50 Gershon, T. *et al.* Relationship between Cu2ZnSnS4 quasi donor-acceptor pair density and solar cell efficiency. *Applied Physics Letters* **103**, 193903, (2013).

51 Nayak, P. *et al.* The impact of Bi3+ heterovalent doping in organic-inorganic metal halide perovskite crystals. *Journal of the American Chemical Society*, (2017).

52 Mićić, O. I. *et al.* Size-Dependent Spectroscopy of InP Quantum Dots. *The Journal of Physical Chemistry B* **101**, 4904-4912, (1997).

53 Wehrenfennig, C., Liu, M., Snaith, H. J., Johnston, M. B. & Herz, L. M. Homogeneous Emission Line Broadening in the Organo Lead Halide Perovskite CH3NH3PbI3–xClx. *The Journal of Physical Chemistry Letters* **5**, 1300-1306, (2014).

54 Yan, Z.-Z., Jiang, Z.-H., Lu, J.-P. & Ni, Z.-H. Interfacial charge transfer in WS2 monolayer/CsPbBr3 microplate heterostructure. *Frontiers of Physics* **13**, 138115, (2018).

55 Zi-Yu, P., Jian-Long, X., Jing-Yue, Z., Xu, G. & Sui-Dong, W. Solution-Processed High-Performance Hybrid Photodetectors Enhanced by Perovskite/MoS2 Bulk Heterojunction. *Advanced Materials Interfaces* **0**, 1800505, (2018).

56 Li, H., Zheng, X., Liu, Y., Zhang, Z. & Jiang, T. Ultrafast interfacial energy transfer and interlayer excitons in the monolayer WS2/CsPbBr3 quantum dot heterostructure. *Nanoscale* **10**, 1650-1659, (2018).

57 Zhu, H. *et al.* Interfacial Charge Transfer Circumventing Momentum Mismatch at Two-Dimensional van der Waals Heterojunctions. *Nano Letters* **17**, 3591-3598, (2017).

58 Rigosi, A. F., Hill, H. M., Li, Y., Chernikov, A. & Heinz, T. F. Probing Interlayer Interactions in Transition Metal Dichalcogenide Heterostructures by Optical Spectroscopy: MoS2/WS2 and MoSe2/WSe2. *Nano Letters* **15**, 5033-5038, (2015).
59 Comin, R. *et al.* Structural, optical, and electronic studies of wide-bandgap lead halide perovskites. *Journal of Materials Chemistry C* **3**, 8839-8843, (2015).
60 Rudin, S., Reinecke, T. L. & Segall, B. Temperature-dependent exciton linewidths in semiconductors. *Physical Review B* **42**, 11218-11231, (1990).
61 Wright, A. D. *et al.* Electron–phonon coupling in hybrid lead halide perovskites. *Nature Communications* **7**, 11755, (2016).
62 Lee, J., Koteles, E. S. & Vassell, M. O. Luminescence linewidths of excitons in GaAs quantum wells below 150 K. *Physical Review B* **33**, 5512-5516, (1986).
63 Dar, M. I. *et al.* Origin of unusual bandgap shift and dual emission in organic-inorganic lead halide perovskites. *Science Advances* **2**, (2016).
64 Ni, L. *et al.* Real-Time Observation of Exciton–Phonon Coupling Dynamics in Self-Assembled Hybrid Perovskite Quantum Wells. *ACS Nano* **11**, 10834-10843, (2017).
65 Thirumal, K. *et al.* Morphology-Independent Stable White-Light Emission from Self-Assembled Two-Dimensional Perovskites Driven by Strong Exciton–Phonon Coupling to the Organic Framework. *Chemistry of Materials* **29**, 3947-3953, (2017).
66 Ferreira, A. C. *et al.* Elastic Softness of Hybrid Lead Halide Perovskites. *Physical Review Letters* **121**, 085502, (2018).
67 Zienkiewicz, O. C., Taylor, R. L., Nithiarasu, P. & Zhu, J. *The finite element method*. Vol. 3 (McGraw-hill London, 1977).
68 Katan, C., Mohite, A. D. & Even, J. Entropy in halide perovskites. *Nature materials* **17**, 377, (2018).
69 Matthews, J. W. & Blakeslee, A. E. Defects in epitaxial multilayers: I. Misfit dislocations. *Journal of Crystal Growth* **27**, 118-125, (1974).
70 People, R. & Bean, J. C. Calculation of critical layer thickness versus lattice mismatch for GexSi1−x/Si strained-layer heterostructures. *Applied Physics Letters* **47**, 322-324, (1985).
71 Kosyachenko, L. A. *Solar Cells: New Aspects and Solutions*. (BoD–Books on Demand, 2011).
72 Jiang, S. *et al.* Phase Transitions of Formamidinium Lead Iodide Perovskite under Pressure. *Journal of the American Chemical Society*, (2018).
73 Chen, Z. *et al.* Remote Phononic Effects in Epitaxial Ruddlesden–Popper Halide Perovskites. *The Journal of Physical Chemistry Letters*, 6676-6682, (2018).
74 Ge, C. *et al.* Ultralow Thermal Conductivity and Ultrahigh Thermal Expansion of Single-Crystal Organic–Inorganic Hybrid Perovskite CH3NH3PbX3 (X = Cl, Br, I). *The Journal of Physical Chemistry C* **122**, 15973-15978, (2018).
75 Yin, W.-J., Yang, J.-H., Kang, J., Yan, Y. & Wei, S.-H. Halide perovskite materials for solar cells: a theoretical review. *Journal of Materials Chemistry A* **3**, 8926-8942, (2015).
76 Wang, C., Ecker, B. R., Wei, H., Huang, J. & Gao, Y. Environmental Surface Stability of the MAPbBr3 Single Crystal. *The Journal of Physical Chemistry C* **122**, 3513-3522, (2018).
77 Shi, D. *et al.* Low trap-state density and long carrier diffusion in organolead trihalide perovskite single crystals. *Science* **347**, 519-522, (2015).

78 Dong, Q. *et al.* Electron-hole diffusion lengths> 175 μm in solution-grown CH3NH3PbI3 single crystals. *Science* **347**, 967-970, (2015).
79 Wu, Z., Yao, W., London, A. E., Azoulay, J. D. & Ng, T. N. Elucidating the Detectivity Limits in Shortwave Infrared Organic Photodiodes. *Advanced Functional Materials* **28**, 1800391, (2018).
80 Stolterfoht, M., Armin, A., Philippa, B. & Neher, D. The Role of Space Charge Effects on the Competition between Recombination and Extraction in Solar Cells with Low-Mobility Photoactive Layers. *The Journal of Physical Chemistry Letters* **7**, 4716-4721, (2016).
81 Mihailetchi, V. D., Xie, H. X., de Boer, B., Koster, L. J. A. & Blom, P. W. M. Charge Transport and Photocurrent Generation in Poly(3-hexylthiophene): Methanofullerene Bulk-Heterojunction Solar Cells. *Advanced Functional Materials* **16**, 699-708, (2006).
82 Herz, L. M. Charge-Carrier Mobilities in Metal Halide Perovskites: Fundamental Mechanisms and Limits. *ACS Energy Letters* **2**, 1539-1548, (2017).
83 Chen, B., Yang, M., Priya, S. & Zhu, K. Origin of J–V Hysteresis in Perovskite Solar Cells. *The Journal of Physical Chemistry Letters* **7**, 905-917, (2016).
84 Wei, J. *et al.* Hysteresis Analysis Based on the Ferroelectric Effect in Hybrid Perovskite Solar Cells. *The Journal of Physical Chemistry Letters* **5**, 3937-3945, (2014).
85 Tress, W. *et al.* Understanding the rate-dependent J–V hysteresis, slow time component, and aging in CH3NH3PbI3 perovskite solar cells: the role of a compensated electric field. *Energy & Environmental Science* **8**, 995-1004, (2015).
86 Bain, A. K. & Chand, P. *Ferroelectrics: Principles and Applications*. (John Wiley & Sons, 2017).
87 Li, C., Guerrero, A., Huettner, S. & Bisquert, J. Unravelling the role of vacancies in lead halide perovskite through electrical switching of photoluminescence. *Nature Communications* **9**, 5113, (2018).
88 Li, C. *et al.* Real-Time Observation of Iodide Ion Migration in Methylammonium Lead Halide Perovskites. *Small* **13**, 1701711, (2017).
89 Shao, Y. *et al.* Grain boundary dominated ion migration in polycrystalline organic–inorganic halide perovskite films. *Energy & Environmental Science* **9**, 1752-1759, (2016).
90 Lee, J.-W., Kim, S.-G., Yang, J.-M., Yang, Y. & Park, N.-G. Verification and mitigation of ion migration in perovskite solar cells. *APL Materials* **7**, 041111, (2019).
91 Yun, J. S. *et al.* Critical Role of Grain Boundaries for Ion Migration in Formamidinium and Methylammonium Lead Halide Perovskite Solar Cells. *Advanced Energy Materials* **6**, 1600330, (2016).
92 Xing, J. *et al.* Ultrafast ion migration in hybrid perovskite polycrystalline thin films under light and suppression in single crystals. *Physical Chemistry Chemical Physics* **18**, 30484-30490, (2016).
93 Kang, K. *et al.* High-Performance Solution-Processed Organo-Metal Halide Perovskite Unipolar Resistive Memory Devices in a Cross-Bar Array Structure. *Advanced Materials* **31**, 1804841, (2019).
94 Hu, Y. *et al.* Ultrathin Cs3Bi2I9 Nanosheets as an Electronic Memory Material for Flexible Memristors. *Advanced Materials Interfaces* **4**, (2017).
95 Calado, P. *et al.* Evidence for ion migration in hybrid perovskite solar cells with minimal hysteresis. *Nature Communications* **7**, 13831, (2016).

96 Zimmermann, E. *et al.* Characterization of perovskite solar cells: Towards a reliable measurement protocol. *APL Materials* **4**, 091901, (2016).
97 Ayers, J. E., Kujofsa, T., Rago, P. & Raphael, J. *Heteroepitaxy of semiconductors: theory, growth, and characterization*. (CRC press, 2016).
98 Pohl, U. W. *Epitaxy of Semiconductors: Introduction to Physical Principles*. (Springer Science & Business Media, 2013).
99 Ball, J. M. & Petrozza, A. Defects in perovskite-halides and their effects in solar cells. *Nature Energy* **1**, 16149, (2016).
100 Liu, Z. *et al.* Gas-solid reaction based over one-micrometer thick stable perovskite films for efficient solar cells and modules. *Nature Communications* **9**, 3880, (2018).
101 Wang, K.-L. *et al.* Tailored Phase Transformation of CsPbI2Br Films by Copper(II) Bromide for High-Performance All-Inorganic Perovskite Solar Cells. *Nano Letters* **19**, 5176-5184, (2019).
102 Wang, L. *et al.* A Eu(3+)-Eu(2+) ion redox shuttle imparts operational durability to Pb-I perovskite solar cells. *Science* **363**, 265-270, (2019).
103 Zhao, Y. *et al.* Perovskite seeding growth of formamidinium-lead-iodide-based perovskites for efficient and stable solar cells. *Nature Communications* **9**, 1607, (2018).
104 Yang, D. *et al.* High efficiency planar-type perovskite solar cells with negligible hysteresis using EDTA-complexed SnO2. *Nature Communications* **9**, 3239, (2018).
105 Wu, W.-Q. *et al.* Bilateral alkylamine for suppressing charge recombination and improving stability in blade-coated perovskite solar cells. *Science Advances* **5**, eaav8925, (2019).
106 Feng, J. *et al.* Single-crystalline layered metal-halide perovskite nanowires for ultrasensitive photodetectors. *Nature Electronics* **1**, 404-410, (2018).
107 Kong, W. *et al.* Organic Monomolecular Layers Enable Energy-Level Matching for Efficient Hole Transporting Layer Free Inverted Perovskite Solar Cells. *ACS Nano* **13**, 1625-1634, (2019).
108 Liu, X. *et al.* 20.7% highly reproducible inverted planar perovskite solar cells with enhanced fill factor and eliminated hysteresis. *Energy & Environmental Science* **12**, 1622-1633, (2019).
109 Saidaminov, M. I. *et al.* High-quality bulk hybrid perovskite single crystals within minutes by inverse temperature crystallization. *Nature communications* **6**, (2015).
110 Leijtens, T. *et al.* Carrier trapping and recombination: the role of defect physics in enhancing the open circuit voltage of metal halide perovskite solar cells. *Energy & Environmental Science* **9**, 3472-3481, (2016).
111 Brenes, R. *et al.* Metal Halide Perovskite Polycrystalline Films Exhibiting Properties of Single Crystals. *Joule* **1**, 155-167, (2017).
112 Yao, W. *et al.* Organic Bulk Heterojunction Infrared Photodiodes for Imaging Out to 1300 nm. *ACS Applied Electronic Materials*, (2019).
113 Street, R. A., Yang, Y., Thompson, B. C. & McCulloch, I. Capacitance Spectroscopy of Light Induced Trap States in Organic Solar Cells. *The Journal of Physical Chemistry C* **120**, 22169-22178, (2016).
114 Hwang, T. *et al.* Electronic Traps and Their Correlations to Perovskite Solar Cell Performance via Compositional and Thermal Annealing Controls. *ACS Applied Materials & Interfaces* **11**, 6907-6917, (2019).
115 Kovalenko, A., Pospisil, J., Zmeskal, O., Krajcovic, J. & Weiter, M. Ionic origin of a negative capacitance in lead halide perovskites. *physica status solidi (RRL) – Rapid Research Letters*

11, 1600418, (2017).
116 Khan, M. T., Salado, M., Almohammedi, A., Kazim, S. & Ahmad, S. Elucidating the Impact of Charge Selective Contact in Halide Perovskite through Impedance Spectroscopy. *Advanced Materials Interfaces* **0**, 1901193, (2019).
117 Han, C. *et al.* Unraveling surface and bulk trap states in lead halide perovskite solar cells using impedance spectroscopy. *Journal of Physics D: Applied Physics* **51**, 095501, (2018).
118 Samiee, M. *et al.* Defect density and dielectric constant in perovskite solar cells. *Applied Physics Letters* **105**, 153502, (2014).
119 Yi, C. *et al.* Entropic stabilization of mixed A-cation ABX 3 metal halide perovskites for high performance perovskite solar cells. *Energy & Environmental Science* **9**, 656-662, (2016).
120 Yang, W. S. *et al.* High-performance photovoltaic perovskite layers fabricated through intramolecular exchange. *Science* **348**, 1234-1237, (2015).
121 Jeon, N. J. *et al.* Compositional engineering of perovskite materials for high-performance solar cells. *Nature* **517**, 476-480, (2015).
122 Lee, J.-W. *et al.* 2D perovskite stabilized phase-pure formamidinium perovskite solar cells. *Nature Communications* **9**, 3021, (2018).
123 Yuan, S. *et al.* NbF5: A Novel α-Phase Stabilizer for FA-Based Perovskite Solar Cells with High Efficiency. *Advanced Functional Materials* **0**, 1807850, (2019).
124 Fu, Y. *et al.* Stabilization of the metastable lead iodide perovskite phase via surface functionalization. *Nano letters* **17**, 4405-4414, (2017).
125 Gu, L. *et al.* Significantly improved black phase stability of FAPbI3 nanowires via spatially confined vapor phase growth in nanoporous templates. *Nanoscale* **10**, 15164-15172, (2018).
126 Zhou, Y., Kwun, J., Garces, H. F., Pang, S. & Padture, N. P. Observation of phase-retention behavior of the HC (NH 2) 2 PbI 3 black perovskite polymorph upon mesoporous TiO 2 scaffolds. *Chemical Communications* **52**, 7273-7275, (2016).
127 Li, B. *et al.* Surface passivation engineering strategy to fully-inorganic cubic CsPbI3 perovskites for high-performance solar cells. *Nat Commun* **9**, 1076, (2018).
128 Ma, S. *et al.* Strain-Mediated Phase Stabilization: A New Strategy for Ultrastable α-CsPbI3 Perovskite by Nanoconfined Growth. *Small* **0**, 1900219, (2019).
129 Liu, M. *et al.* Lattice anchoring stabilizes solution-processed semiconductors. *Nature*, (2019).
130 Lee, J. H. *et al.* Epitaxial Stabilization of a New Multiferroic Hexagonal Phase of TbMnO3 Thin Films. *Advanced Materials* **18**, 3125-3129, (2006).
131 Vailionis, A., Siemons, W. & Koster, G. Room temperature epitaxial stabilization of a tetragonal phase in ARuO3 (A=Ca and Sr) thin films. *Applied Physics Letters* **93**, 051909, (2008).
132 Xu, Z., Salvador, P. & Kitchin, J. R. First-Principles Investigation of the Epitaxial Stabilization of Oxide Polymorphs: TiO2 on (Sr,Ba)TiO3. *ACS Applied Materials & Interfaces* **9**, 4106-4118, (2017).
133 Liu, B., Long, M., Cai, M.-Q., Hao, X. & Yang, J. Ferroelectric Polarization in CsPbI3/CsSnI3 Perovskite Heterostructure. *The Journal of Physical Chemistry C*, (2018).
134 Ahmadi, M., Wu, T. & Hu, B. A Review on Organic–Inorganic Halide Perovskite Photodetectors: Device Engineering and Fundamental Physics. *Advanced Materials*, (2017).
135 Yang, Z. *et al.* High-Performance Single-Crystalline Perovskite Thin-Film Photodetector. *Advanced Materials*, (2018).

136 Zhao, Y., Li, C. & Shen, L. Recent advances on organic-inorganic hybrid perovskite photodetectors with fast response. *InfoMat* **0**, (2019).
137 Li, Y. & Yang, K. High-throughput computational design of organic–inorganic hybrid halide semiconductors beyond perovskites for optoelectronics. *Energy & Environmental Science* **12**, 2233-2243, (2019).
138 Haihua, Z. *et al.* A Two-Dimensional Ruddlesden–Popper Perovskite Nanowire Laser Array based on Ultrafast Light-Harvesting Quantum Wells. *Angewandte Chemie International Edition* **0**, 7748-7752, (2018).
139 Ye, F. *et al.* High-Quality Cuboid CH3NH3PbI3 Single Crystals for High Performance X-Ray and Photon Detectors. *Advanced Functional Materials* **0**, 1806984, (2018).
140 Ji, L., Hsu, H.-Y., Lee, J., Bard, A. J. & Yu, E. T. High performance photodetectors based on solution-processed epitaxial grown hybrid halide perovskites. *Nano letters*, (2018).
141 Zhang, Y. *et al.* Trash into Treasure: δ-FAPbI3 Polymorph Stabilized MAPbI3 Perovskite with Power Conversion Efficiency beyond 21%. *Advanced Materials* **0**, 1707143, (2018).